

2004

Femtosecond pulsed laser ablation and patterning of 3C-SiC films on Si substrates for MEMS fabrication

Yuanyuan Dong
Iowa State University

Follow this and additional works at: <https://lib.dr.iastate.edu/rtd>

 Part of the [Mechanical Engineering Commons](#)

Recommended Citation

Dong, Yuanyuan, "Femtosecond pulsed laser ablation and patterning of 3C-SiC films on Si substrates for MEMS fabrication " (2004).
Retrospective Theses and Dissertations. 1154.
<https://lib.dr.iastate.edu/rtd/1154>

This Dissertation is brought to you for free and open access by the Iowa State University Capstones, Theses and Dissertations at Iowa State University Digital Repository. It has been accepted for inclusion in Retrospective Theses and Dissertations by an authorized administrator of Iowa State University Digital Repository. For more information, please contact digirep@iastate.edu.

**Femtosecond pulsed laser ablation and patterning of 3C-SiC films
on Si substrates for MEMS fabrication**

by

Yuanyuan Dong

A dissertation submitted to the graduate faculty
in partial fulfillment of the requirements for the degree of

DOCTOR OF PHILOSOPHY

Major: Mechanical Engineering

Program of Study Committee:
Palaniappa A. Molian (Major Professor)
Michael Olsen
Abhijit Chandra
Li Cao
Gary Tuttle

Iowa State University

Ames, Iowa

2004

Copyright © Yuanyuan Dong, 2004. All rights reserved.

UMI Number: 3158327

INFORMATION TO USERS

The quality of this reproduction is dependent upon the quality of the copy submitted. Broken or indistinct print, colored or poor quality illustrations and photographs, print bleed-through, substandard margins, and improper alignment can adversely affect reproduction.

In the unlikely event that the author did not send a complete manuscript and there are missing pages, these will be noted. Also, if unauthorized copyright material had to be removed, a note will indicate the deletion.

UMI[®]

UMI Microform 3158327

Copyright 2005 by ProQuest Information and Learning Company.

All rights reserved. This microform edition is protected against unauthorized copying under Title 17, United States Code.

ProQuest Information and Learning Company
300 North Zeeb Road
P.O. Box 1346
Ann Arbor, MI 48106-1346

Graduate College
Iowa State University

This is to certify that the doctoral dissertation of
Yuanyuan Dong
has met the dissertation requirements of Iowa State University

Signature was redacted for privacy.

Major Professor

Signature was redacted for privacy.

For the Major Program

TABLE OF CONTENTS

LIST OF FIGURES	vi
LIST OF TABLES	xi
ACKNOWLEDGEMENTS	xii
ABSTRACT	xiii
CHAPTER 1. INTRODUCTION	1
CHAPTER 2. LITERATURE REVIEW	5
CHAPTER 3. HIGH-ENERGY FEMTOSECOND PULSED LASER MICROMACHINING OF SILICON CARBIDE COATED SILICON IN SELF-FOCUSED AIR MEDIUM	38
CHAPTER 4. FEMTOSECOND PULSED LASER ABLATION OF 3C-SiC THIN FILM ON SILICON	63
CHAPTER 5. FEMTOSECOND PULSED LASER MICROMACHINING OF SINGLE CRYSTALLINE 3C-SiC and Si STRUCTURES	84
CHAPTER 6. FORMATION AND CHARACTERIZATION OF FEMTOSECOND PULSED LASER SYNTHESIZED NANOPARTICLES ON THIN FILMS OF 3C-SiC	97
CHAPTER 7. FEMTOSECOND PULSED LASER ABLATION OF DIAMOND-LIKE CARBON FILMS ON SILICON	118
CHAPTER 8. GENERAL CONCLUSIONS AND FUTURE WORK	128
APPENDIX A. EVALUATION OF B-INTEGRAL	131
APPENDIX B. CRITICAL REVIEW: PHYSICAL MECHANISMS AND MODELING OF ULTRASHORT LASER ABLATION	133

LIST OF FIGURES

Figure 2.1	Nd laser drilling and scribing	9
Figure 2.2	Excimer laser drilling in polyimide	13
Figure 2.3	The intensity profile of the laser focus spot	23
Figure 2.4	Holes drilled through a 100 mm steel foil	24
Figure 2.5	Medical implants (stents) made of tantalum by femtosecond laser	27
Figure 2.6	(a) Photoinduced holographic gratings in bulk polymer by femtosecond laser. (b) Femtosecond laser photopolymerized bull sculpture by two-photon absorption (TPA)	29
Figure 3.1	Traditional technique for producing sub-micron structures	41
Figure 3.2	Ablation threshold versus the number of laser pulses for SiC film on Si	49
Figure 3.3	SEM images of laser microdrilled silicon at 1 mJ in air in single-shot mode	51
Figure 3.4	SEM image of laser irradiated surface at 1mJ, 1 kHz, N=50 in continuous-shot mode	52
Figure 3.5	SEM images of laser microdrilled holes at 0.6 mJ in continuous-shot mode	53
Figure 3.6	SEM images of holes at 0.25 mJ using a 20× objective lens in continuous-shot mode	54
Figure 3.7	Profilometer traces of holes	54
Figure 3.8	(a) Hole depth versus the number of pulses as a function of pulse energy at 1 kHz (b) Diameters of holes and thermal damages for various pulses at a constant pulse energy of 0.9 mJ and 1 kHz (c) A schematic diagram showing the definitions of hole and damage regions	55

Figure 3.9	The effect of translation speed on (a) cutting width (b) cutting depth	58
Figure 3.10	SEM images of laser-cut grooves at 0.8 mJ using (a) Femtosecond laser 120fs (b) Nanosecond laser 200ns	59
Figure 4.1	A schematic representation of a laser micromachining set-up	66
Figure 4.2	SEM images of laser-induced 3C/SiC surface morphology for a single pulse in air	68
Figure 4.3	SEM images of laser-induced 3C/SiC surface morphology at 7 μ J in air	70
Figure 4.4	SEM images of laser-induced 3C-SiC surface morphology at 0.2 μ J in air	72
Figure 4.5	SEM image of the fracture section of the single-crystalline SiC film	73
Figure 4.6	Depth of the laser-generated cavities versus the number of laser pulses N applied to 3C-SiC in air	74
Figure 4.7	Squared diameters, D ₂ , of the modification and the ripple areas as a function of the applied laser fluences for single-pulse processing of 3C-SiC in air, respectively	76
Figure 4.8	The surface-damage threshold as a function of the number of laser pulses N at low processing fluence for the ablation of 3C-SiC in air	77
Figure 4.9	SEM image of the ripple zone: an amorphous phase and nanoparticles with a size of about 100 nm, resulting from re-crystallization	79
Figure 5.1	SEM images of rotors of micromotors processed at different energies in helium	89
Figure 5.2	SEM images of microturbine rotors processed at 0.5 μ J	90
Figure 5.3	SEM images of lateral resonator processed at 1 μ J	92
Figure 5.4	The stylus profilometer scans for the holes that did not go all the way through the wafer.	95
Figure 6.1	Scanning electron micrographs of 800-nm, 120-fs laser-irradiated 3C-SiC areas, Plan view for the sample treated at four different laser fluences	102

Figure 6.2	Effect of Gaussian profile energy on the size of nanoparticles	105
Figure 6.3	The typical atomic force micrographs of nanoparticles in SiC film irradiated below $0.6F_{th}$.	106
Figure 6.4	X-ray diffraction spectra of 3C-SiC films unexposed and exposed to the ultrafast laser	109
Figure 6.5	The AES spectra of before- and after- irradiated films at 0.45 J/cm^2 .	110
Figure 6.6	The Raman spectra taken from before- and after-laser-irradiated 3C-SiC films at different fluences	112
Figure 7.1	Squared diameters D^2 of the damaged areas in dependence on the applied laser pulse energies for single pulse processing ($\tau = 120 \text{ fs}$, $\lambda = 800 \text{ nm}$) of DLC in air	121
Figure 7.2	Ablation threshold $E_{th}(N)$ at $0.24 \mu\text{J}$ as a function of the number of pulses N for the ablation ($\tau = 120 \text{ fs}$, $\lambda = 800 \text{ nm}$) of DLC in air	122
Figure 7.3	SEM images of laser-induced DLC surface morphology	124
Figure 7.4	SEM images of laser-induced DLC surface morphology at $0.24 \mu\text{J}$ and 1000 pulses	125
Figure B.1	Absolute electron-hole density as function of excitation fluence	144

LIST OF TABLES

Table 3.1	Ablation threshold, F_{th} , from thermal and optical properties.	50
-----------	---	----

ACKNOWLEDGEMENTS

I would like to express my thanks to my major professor, Dr. Molian, for his direction and support during my Ph.D. study. I would also like to thank Dr. Tuttle, Dr. Olsen, Dr. Cao, Chandra, and Dr. Bullen, for accepting to serve on my committee, and providing advices for the successful completion of my dissertation.

My special thoughts of gratitude go to my husband and my parents and my sisters. Their hopes and aspirations helped me fulfill my goals. I would also like to thank the various technicians and researchers who helped me with my research at various points. Special thanks go to Jim Dautremont for his assistance in troubleshooting problems with the various equipment in the research laboratory, and to Dr. Straszheim for his assistance in helping me with a great amount of SEM work.

ABSTRACT

Femtosecond pulsed laser (FPL) micromachining is a direct-writing technique in which an ultrashort pulse laser beam is focused to dimensions of a few microns inside or on the surface of the substrate and then moved around using a X-Y positioning table, thereby creating either features or patterns as required. It outperforms conventional micromachining technologies due to advantages such as precise resolution, minimal thermal or shock damage, and absence of discrimination among materials. 3C-SiC is a very important semiconductor in electronics and opto-electronics and more recently regarded as an optimal candidate for structural or coating applications in microelectromechanical systems (MEMS) used under harsh and high-temperature environments. However, it is a very difficult material to be machined or etched by mechanical or chemical methods.

In this work, fundamental studies on the interaction of femtosecond pulsed beam with 3C-SiC films were performed. The influence of laser parameters such as pulsed energy on the ablation and calculations of damage thresholds and ablation rates were determined. Based on these results, MEMS structures including micromotors, microturbine rotors, and lateral resonators were patterned with good quality and repeatability. Research demonstrates that FPL micromachining is capable of offering a unique solution to overcome the traditional barriers in SiC machining method, opening up opportunities for SiC materials to be used in industrial environment.

As a spinoff of femtosecond pulse micromachining, nanostructuring of 3C-SiC films on Si was observed. Nanoparticle surfaces were further studied in terms of formation conditions and characterizations of crystal structure and related properties. "Incubation"

effects were identified and Coulomb explosion mechanism was proposed to be responsible for the generation of nanoparticles.

Results of research enhance our current understanding of ultrashort pulse-matter interactions and offer potential applications for SiC-MEMS.

CHAPTER 1. INTRODUCTION

Broad applications of femtosecond pulsed lasers (FPL) have been witnessed in numerous areas of science and engineering since its invention over the past decades. Micromachining by FPL is a potential ramification of micromachining technologies when manufacturers incessantly shrink their product size down to meet their needs. The reason is simple. FPL's precise localized-energy deposition, minimal collateral damage and wavelength-independence make it a standout for ultra-precise machining.

The purpose of research is to systematically investigate femtosecond laser micro-or nanomachining and nanostructuring of 3C-SiC films on Si substrates. 3C-SiC is chosen as the material because of its potential for numerous applications and lack of good micro-fabrication techniques due to its chemical inertness and hardness. The difficulty in machining SiC is the principal bottleneck of exploiting its potential applications, particularly its use for MEMS devices. Other difficult-to-machine materials such as diamond-like-carbon thin films were also investigated.

This body of investigation with the central theme of femtosecond laser micro- or nanomachining includes following sections: 1) design of optical delivery systems for micromachining and nanostructuring; 2) experimental investigations of the effects of laser parameters on generating micro- or nanostructures and characterizations and evaluations of micro- or nanostructures by various diagnostic techniques, for example, SEM, AFM, XRD, AES, and micro-Raman spectroscopy; 3) computation of key parameters like damage threshold and ablation rate using basic laser physics so as to obtaining high-quality patterning of MEMS structures and unveiling the physical picture of laser-matter interactions; 4) pattern

of MEMS structures through positioning-table motions; 5) understanding of physical mechanisms and formulation of an analytical model of the interaction of ultrashort laser with 3C-SiC. The research results not only offer a proof of the capability of femtosecond pulses laser in this rapidly expanding area of micromachining, but also find its perspectives in nanostructuring of material surfaces.

Dissertation organization

The dissertation is organized into nine chapters and two appendices. Chapter 1 (this chapter) states the objectives of the research and provides a brief summary of the studies that are presented in latter chapters. Chapter 2 provides literature review of recent developments in laser micromachining. Chapter 3, a paper published in *Journal of Laser Applications*, reports on the investigation of using the self-focusing capability of air induced by high-energy femtosecond pulses to produce nanostructures. In this paper, the effects of pulse energy, the number of pulses, pulse repetition rate and x-y translation speed on the size, shape and thermal damage of holes and grooves were evaluated. Despite the capability of air medium to produce tiny holes of few μm diameters, the shape of the hole is highly asymmetrical due to the beam profile distortion. A comparison of femtosecond pulsed laser ablation with nanosecond pulsed laser ablation demonstrated the advantages of small size, minimal thermal damage and cleanliness for ultra-short pulses. Chapter 4, a paper published in the *Applied Physics A: Materials Science & Processing*, presents the threshold fluence and ablation rate, useful for the micromachining of the 3C-SiC films. It discusses the role played by energy fluence on the material removal mechanisms. The effect of “incubation” due to accumulation of defects was experimentally verified. Helium assisted in improving the

processing quality and ablation rate of SiC thin films due to its inertness and high ionization potential. Chapter 5, a paper published in the *Journal of Micromechanics and Microengineering*, reports on laser-assisted surface micromachining of 3C-SiC thin films on Si substrate for the patterning of MEMS structures such as micromotor, gas turbine rotor and lateral resonators. Besides, it demonstrates that the high-quality membranes of pressure sensor with controllable diameter and thickness can be produced using laser-assisted bulk micromachining of 6H-SiC. Femtosecond laser direct-writing is a promising technology for structuring of MEMS devices. Chapter 6, two combined papers, one published in *Applied Physics Letters* and the other submitted to *Physica Status Solidi A*, reports on the formation of highly-oriented, uniform, and spherical nanoparticles of 3C-SiC as a result of Coulomb explosion caused by the interaction of near infrared ultrafast laser pulses with 3C-SiC thin films grown on Si substrate. The formation mechanism, size, shape, composition and structure of nanoparticles were analyzed by means of SEM, AFM, XRD, AES and Raman spectroscopy. Chapter 7, a paper submitted to *Applied Surface Science*, presents that femtosecond laser micromachining of thin diamond-like carbon (DLC) films on silicon in two aspects: one is to estimate ablation threshold and investigate the influence of ablation parameter on the morphological features of ablated regions; two is to compare the results with picosecond pulsed laser ablation. Chapter 8 summarizes the generic conclusions drawn from this body of research, and suggests future work for clarifying the physical mechanism in more details in order to best understand and direct experiments.

Appendix A provides a detailed derivation for the B-integral, which characterizes the extent of nonlinear effects of self-focusing and/or filamentation. Appendix B comprehensively analyzes the physical mechanisms of ultrashort laser-matter interaction

from the viewpoints of both microscopic electron-phonon dynamics and macroscopic heat transport. An analytical model of the interaction of femtosecond with 3C-SiC was developed.

CHAPTER 2. LITERATURE REVIEW

LASER MACHINING

Laser machining is a material removal process accomplished through laser and target material interactions [1]. The basic mechanisms include absorption of photon energy and conversion of light energy to thermal energy or photochemical energy. Material is removed by melting and blowing away, or by direct vaporization/ablation or by bond breaking. Laser machining is a non-contact process yet it has high spatial confinement. The forces in laser machining are small. The photon pressure is negligible. In contrast, the traditional machining processes rely on mechanical stresses induced by tools to break the bonds of materials.

Laser machining produces narrow heat affected zone and re-solidified layer in micron dimensions. It can machine hard materials or brittle materials such as ceramics by judicious selection of laser wavelength. High aspect ratio holes with small diameters impossible for other methods can be drilled using lasers. Laser machining offers unmatched flexibility. Laser light can be transmitted and reflected to the desired locations at high speeds so that precise 3D machining can be conveniently realized. The combination of fiber-transmitted laser energy and robotic technology can provide a system with great dimensional freedom. Fixtures can be greatly simplified due to the non-contact nature. Laser machining is extremely sensitive due to the focusing property of the laser beam. At focus, the laser intensity is highest and away from it, laser intensity drops rapidly. The depth of focus of the laser beam is relatively small (tens of microns to around a few millimeters), thus limiting the cutting depth. By comparison, traditional machining processes cause large areas of work damage. These involve various tools for materials with different hardness or abrasiveness.

Further treatment is necessary to remove dross adhesion and edge burr in order to obtain high precision.

Some traditional machining methods can achieve better surface qualities than laser machining process in the macro-scale applications. However, it is usually more economical and efficient to use laser machining process for micro-scale applications because of its low thermal damage to workpiece. The kerf in laser cutting can be made very narrow ($<100\ \mu\text{m}$), the depth of laser drilling can be controlled to less than one micron per laser pulse and shallow permanent marks can be made with great flexibility. Small blind holes, grooves, surface texturing and marking can be achieved with excellent quality. However, this also means low material removal rate in laser machining process compared with traditional machining. Laser machining is not efficient for bulk material removal through pure thermal effects. At present, there is growing interest in the precise fabrication of micro- and nanostructures such as motors, optics, sensors, fluid control devices, actuators, miniature valves, pacemakers, implants, and catheters. The traditional mechanical approaches of cutting, drilling, and shaping materials are no longer satisfactory for fabricating micron-scale structures. Instead, beam techniques based on photons, electrons, and ions are used to produce high-resolution structures. Lasers have been proven as effective tools in micromachining. Lasers have been used to solve fine machining problems in numerous fields, including medical devices, telecommunication, microelectronics, fiber optics, data storage, instrumentation, and micro-optics. Compared with other technologies for micromachining applications, lasers are suitable for those applications that demand more precision, speed, and "direct-write" capability. Lasers can also work on most materials and are environmentally friendly.

Ultraviolet (UV) lasers are widely used for micromachining applications. The most popular and commercial UV lasers include excimer, argon-ion, tripled and quadrupled Nd:YAG, fluorine, helium-cadmium, metal vapor, and nitrogen. Among these, excimer lasers (193 to 351 nm) are the best choices, but Nd:YAG lasers may be considered if they are Q-switched and frequency- quadrupled to produce 266 nm.

Nd:YAG LASER MACHINING [2,3,4]

Nd:YAG laser is one of the two common solid-state lasers (the other one is Nd:glass laser). YAG is a complex crystal of Yttrium-Aluminium-Garnet with a chemical composition of $Y_3Al_5O_{12}$, and it is transparent and colorless. About 1% Nd^{3+} (Neodinium) ions are doped into the YAG crystal, and the crystal color then changes to a light blue color. Nd^{3+} ions are suspended in crystalline matrix to generate laser light. The ions emit electrons when excited, the crystalline matrix spreads the energy among the ions. Nd:YAG laser uses krypton or xenon flash lamps for optical pumping. Its power can be up to several hundred watts in continuous mode, and high pulse rates (50 kHz) can be reached. The fundamental wavelength of Nd:YAG laser is 1.06 μm . Nd:YAG lasers are designed to operate in continuous mode or pulsed mode. The pulse width varies from 1 ms to 10 ns. Q-switched Nd:YAG lasers may have second-harmonic ($\lambda = 532$ nm), third-harmonic ($\lambda = 355$ m), and fourth-harmonic beams ($\lambda = 266$ nm) by double-, triple-, and quadruple-frequency technology. In this way, the green and ultraviolet beams can be obtained with capability to focus smaller spots than the infrared beams because of the short wavelength. In addition, a

wider range of materials can be processed because of the absorption of the different materials at different wavelengths.

Both infrared and ultraviolet Nd:YAG laser processing are well established and have reached routine production status for a variety of applications in the electronics industry.

These applications include:

- Resistor trimming;
- *Via* drilling (Figure 2.1a); Frequency-tripled and frequency-quadrupled Nd:YAG lasers offer the attractive characteristic of very high absorption in many materials of interest, such as polyimide materials, resulting in fine machining of flex circuits and multichip modules.
- Removal of small amounts of unwanted metallization on master patterns used for making photographic masks for integrated circuit chips; Frequency-doubled Nd:YAG lasers operating at 532 nm are often used since the absorptivity of the metal is relatively high at this wavelength.
- Metallization of copper for the interconnecting links;
- Laser tape-automated bonding of leads to integrated circuit input-output pads; Laser bonding has less chance of damaging the chip because of its localized nature, which is an advantage over conventional techniques like thermocompression bonding. Materials that have been used include gold, copper, and tin. The rate of formation of the bonds can be high, greater than 60 per second. This is a growing yet relatively small interconnection application for millisecond pulse Nd:YAG lasers.

- Hermetic sealing of electronic packages by laser welding, a final packaging application for which infrared Nd:YAG laser with pulses in the millisecond regime is served. Laser welding has the advantages of no damage or distortion of the delicate components in the package and smaller heat-affected zone than the competing techniques such as tungsten-inert gas (TIG) welding and resistance welding. Laser welding provides production package sealing with excellent hermeticity and good shock and vibration resistance.
- Laser annealing of ion - implanted layers, for which Q-switched Nd:YAG lasers with pulse duration around 100 nsec has been most often used. The duration of laser annealing is short enough to retain the intrinsic advantages in comparison with conventional methods, though it is not economically viable for production application.

Scribing (Figure 2.1b) and marking of silicon may be done with Nd:YAG laser because silicon absorbs well at wavelengths near 1 micron. Laser marking, instead of conventional printing and stamping, provides an attractive alternative for durable permanent marks with no possibility of contamination. It also compares favorably with other marking systems, when the comparison is based on throughput, performance and flexibility. Nd:YAG laser scribing and marking have many applications in electronics, cosmetics, food and beverage, and optical industries including grooving of micro-channels for cooling systems and creation of slots for assembly.

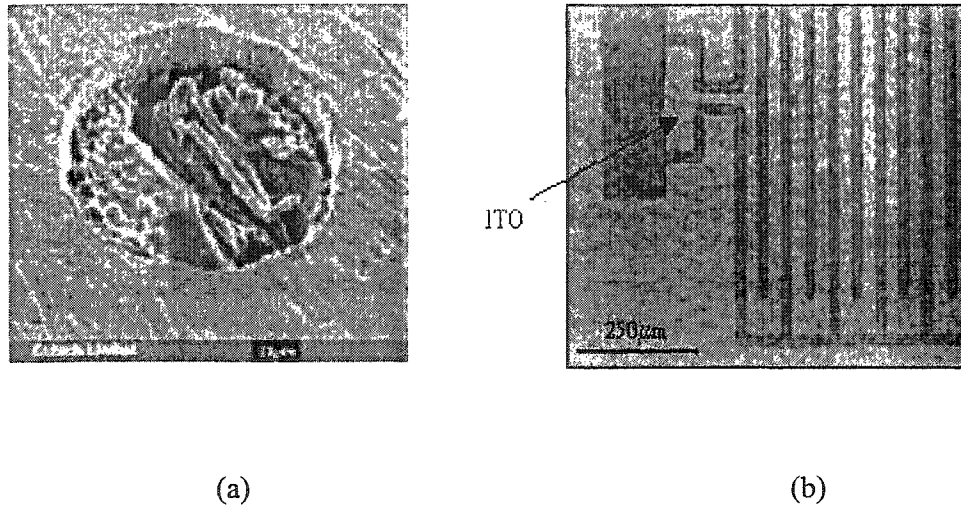


Figure 2.1. (a) 100µm diameter blind microvia drilled in a PCB. Nd laser trepanned hole in top copper conductive layer. (b) a thin film of ITO on glass scribed with 25µm wide tracks by the Q-switched 3rd-harmonic Nd laser machine. (Source: Exitech Ltd)

Nd:YAG lasers also play an important role in medical applications. In coagulation and tissue evaporation, cw Nd:YAG lasers with powers as high as 50 W are used; the beam is delivered, through an optical fiber inserted into a conventional endoscope, to the internal organs (lungs, stomach, bladder) of the human body. Repetitively Q-switched Nd:YAG lasers are used for photo-disruption of transparent membranes of pathological origin, which can appear in the anterior chamber of the eye (e.g., secondary cataract) or for iridectomy.

Nd:YAG laser's scientific applications are in the areas of micromachining or microstructuring where Q-switched lasers with their frequency-tripled harmonic and frequency-quadrupled harmonic as well as mode-locked lasers were often considered. The reason is that the absorption is higher in UV region and many materials are best machined using UV laser sources. Drilling and cutting of various materials including ceramics (ZrO_2 ,

Al_2O_3 , Si_3N_4 , Diamond and WC), polymers (PETG, PMMA), metal and semiconductor were investigated. Effects of absorption, energy density, repetition rate and time for drilling on the maximum diameter, maximum depth, removal depth per pulse and quality of processing were determined. 3D-microstructure, fabrication of optical fiber, and rapid prototyping of micromechanical devices are explored using Nd:YAG lasers. Though the feasibility was proven, the small feature size and high quality of processing are not best achievable due to the limitation of the pulse duration (nanosecond).

EXCIMER LASER MICROMACHINING [3,5,6]

Excimer lasers represent an interesting and important class of molecular lasers involving transitions between different electronic states of special molecules referred to as excimers. Typical excimer complexes include argon fluoride (ArF), krypton fluoride (KrF), xenon fluoride (XeF), and xenon chloride (XeCl). The output wavelengths of the excimer lasers vary from 193 to 351 nm in the ultraviolet to near-ultraviolet. Fluorine (F_2) excimer laser has the shortest wavelength of 157 nm. Excimer lasers have high repetition rates up to 500 Hz and high average powers up to 100 W. Excimer laser can be operated only in the pulsed regime. The pulse duration is in the range of several tens of nanoseconds and the pulse energy is on the order of hundreds of millijoules. The efficiency of these lasers is relatively high (2-4%) as a result of the high quantum efficiency and high efficiency of the pumping processes.

The physics of the material removal process for excimer lasers is different from that of CO_2 or Nd:YAG lasers, which operate in a visible or infrared wavelength regime and remove materials with low to medium resolution through melting or vaporization. The UV

excimer lasers remove material with high resolution through ablation, direct decomposition of chemical bonds due to absorption of single or multiple photons (photolytic process) and heat-affected decomposition of chemical bonds (pyrolytic process). In ablation, structures in the sub-micrometer to micrometer range can be formed transiently with minimum thermal effects. Processing with excimer lasers results in higher precision and reduced heat damage zones compared with CO₂ and Nd:YAG lasers. Such benefits derive from their short wavelengths (193 to 351 nm), high energy per pulse, and nanosecond (ns) pulse widths.

In general, the small wavelengths allow strong interactions of the beam with a variety of materials, however, the UV excimer-material interaction mechanisms may still be differentiated based on the type of material bonds. The photolytic interaction is dominant for covalent bonds, which is very common in polymer and organic materials, and partially for ionic bonds [7]. Pyrolytic-dominated mechanism is accountable for excimer laser interaction of other materials, e.g. ceramics, glasses, and metals.

Due to the above-mentioned characteristics, excimer laser ablation is extremely desirable for polymer processing applications. The high photon energy of UV excimer laser radiation leads to a direct interaction of photons with electrons without excitation on the rotational and vibrational level [7]. As a result, excimer lasers for machining polymer have greater precision with sub-micron spatial and depth resolution. Pioneered by IBM and Siemens in the 1980's [8,9], excimer lasers have been used for drilling vertical interconnection arrays (vias) in polyimide layer for the production of multichip modules (Figure 2.2 a) and also investigated for drilling multilevel polymer printed wiring boards. This technique has proved to be faster and less expensive than the competing techniques of

wet etching or reactive ion etching. It is now commonplace to create via holes as small as 10 micron in polyimide dielectrics for electronic packaging. Via drilling in microelectronic packaging continues to be a major application of excimer laser micromachining.

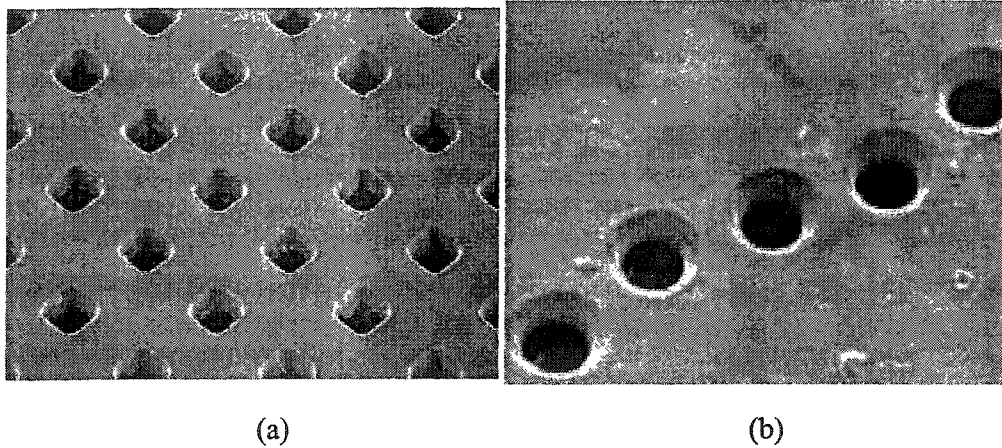


Figure 2.2. Excimer laser drilling (a) 100µm x 100µm square via array in polyimide (Source: Resonetic, Inc.) (b) Array of 30µm diameter ink jet printer nozzles drilled in polyimide (Source: Exitech Ltd.)

Applications of excimer lasers ablation are pervasive to semiconductors, data storage devices, medical devices, photonics and computer peripherals as well. Lithography exposure tools utilizing excimer lasers is truly one of the significant supplements. The 193 and 248 nm UV lights provide a good illumination source for achieving sub-micron-size features in semiconductor microchips. KrF-, ArF-laser-based photolithography offer desirable features for fabrication of DRAM devices with feature size of 0.25 µm, with adequate control of critical dimensions, overlay, and depth of focus, which may be regarded as a benchmark of microcircuit fabrication. Their high power output leads to short wafer exposure times. The

linewidth may be as narrow as a 1-2 picometers (pm) for frequency stabilized KrF lasers. This meets the linewidth requirements for the source, so that it is possible to design high-performance all-quartz optical systems without the need for color correction. For photonics applications, its capability of writing sub-micron period relief gratings on polymer surfaces and fabricating fiber optic grating on inorganics are well demonstrated. Medical applications of excimer lasers, for example, include corneal sculpting, to change the refractive power of the eye and hence correct myopia and microchannel fabricating in polymers for “lab-on-chip” components for biological analysis [10]. A popular use in computer peripherals is drilling very precise holes (ink-jet nozzles) in thin plastic films (polymeric substrates) (as used, e.g., in the ink jet printer head). Excimer lasers are also used to strip polymer insulation from fine wires to connect the head to the drive circuitry for data storage devices fabrication, remove metal films from polymer substrates, micromachine ceramics and semiconductors, and mark thermally sensitive materials, among other things.

Another significant difference in machining between excimer and CO₂ or YAG lasers is that the latter takes advantage of the beam interaction of the workpiece to machine and form the desirable 2-D or 3-D features through the programmed movement of workpiece while excimer lasers produce large area beams that are masked through a template to achieve the desired cutting area. The pattern of the mask may be transferred onto the workpiece with a proportional reduction in size through projection lenses of various magnifications. The workpiece is mounted onto precision XY stages. Laser processing can be achieved stationary or moving workpiece. With the help of synchronized scanning of the mask and workpiece with sub-micron precision, the transfer of large areas of the mask pattern onto the sample can

be realized. The features produced in the workpiece are a function of the mask shape, the relative motions of the mask and the workpiece and the firing of the laser.

Excimer laser ablation in conjunction with mask projection techniques allows incredible flexibility in the types of processing and the geometries of the structures such as micro-channels, ramps, contoured surfaces with channels, micro-lens etc. Many areas are advancing rapidly from the use of the unique structures that can be produced by excimer laser micromachining techniques. In particular, micro-fluidic systems, where one or more fluids are mixed, separated or transported, are utilizing laser-produced features, and features such as ramps, reservoirs, channels and contoured shapes are being incorporated into production devices.

FEMTOSECOND LASER MICROMACHINING

Frequency-tripled, quadrupled Nd:YAG lasers and excimer lasers have achieved much progress in laser micromachining for feature sizes less than 100 μm in part due to their short ultraviolet (UV) wavelength. But this wavelength has its limitation for processing a large class of transparent materials, including some glasses and plastics. The corrosive gases in the excimer lasers make handling difficult. The use of ultrafast (less than 1 ps) laser pulses opened up new opportunities for precision machining, which keeps pace with the application demands in the microelectronics and microfabrication industries and biomedical fields as structure sizes move to even smaller dimensions while the processing is free from collateral damage.

Femtosecond pulsed laser system

Femtosecond pulsed lasers are also known as ultrashort or ultrafast pulsed lasers (pulse width $<1\text{ps}$). A typical femtosecond laser system consists of an oscillator and an amplifier. The generation of femtosecond laser pulses should be credited to both Ti:sapphire material and chirped pulse amplification (CPA) technology.

Ti:sapphire is one solid-state material that has favorable characteristics such as high saturation fluence, high thermal conductivity, high damage threshold and broad bandwidth extending from 700 to 1100 nm for developing fs-pulses [11]. It not only can produce the very short seed pulses through Kerr-lens modelocking but also is nearly ideal for amplification. Ultrashort light pulses are firstly generated at a high repetition rates ($\sim 100\text{MHz}$) with pulse energies in the range of nanojoules, and with pulsewidths in the range of 10^{-12}s to 10^{-14}s [12] by mode-locking means. CPA technique [13] is widely used to amplify the nanojoule pulse energy to microjoule and millijoule level for broader applications without damaging the optical components inside the amplifier. CPA is a process of stretching out, amplifying and recompressing the pulses. Before amplification, the pulsewidth is made longer by a factor of 1000 to 10,000 times in a pulse stretcher to reduce the damaging effect of peak intensity. The stretcher is a telescope of unity magnification, connecting two anti-parallel diffraction gratings. The longer the wavelength of light, the shorter the path they travel and thus the sooner they arrive at the next stage. [14]. The stretched pulse, with perhaps less than 1 W of peak power, is then amplified by passing through a high-energy-density medium, such as Ti:sapphire crystal in a regenerative amplifier. The crystal is excited either by a continuous-wave (CW) or Q-switched pump laser. After the stretched seed pulse has made multiple passes through the gain crystal, the

amplified pulse with up to the several-gigawatt limit imposed by nonlinearities exits the amplifier. The amplified long pulse is recompressed back to its short pulse state by a pair of parallel gratings with the path length shortest for short wavelengths. When the pulse recompressed back to a few femtoseconds, peak powers of up to petawatts (10^{15} W) can be achieved. The average output power of a typical regenerative amplifier is about 1 W, depending on the choice of pump laser. The repetition rate of a regenerative amplifier is many orders of magnitude lower than the original seed laser, however, so the pulse energy and peak power are many times higher--how much higher depends on the repetition rate [15]. The ability of CPA type lasers to amplify pulses to extreme levels opens new avenues in science and technology. In science, scientists use it to explore applications in thermonuclear ignition or in the generation of high-energy photons (x-ray) or particles. In technology, femtosecond lasers can compare against electrodischarge machining (EDM) and focused ion beam (FIB) for micromachining at dimensions of less than 100 μm , which are equipment-intensive and have limitations. The prospects for ultrafast-pulse laser as an alternative look promising [16].

Mechanisms of femtosecond laser micromachining

The physical mechanisms of femtosecond laser-induced ablation are not fully understood, which are strongly dependent on specific optical and thermodynamic properties of the solid, laser wavelength, and pulse duration. The mechanisms are essentially due to the transient behaviors and interactions among photons, electrons, and phonons. However, a wealth of valuable information on ultrashort laser-matter interaction has been obtained through investigations of materials processing by femtosecond laser. It is recognized that

ultrashort pulse duration exhibits advantages in terms of feature size and minimal collateral damage compared to long pulse duration (ns) in high-precision laser machining of materials.

In the early 1990s, researchers at the University of Michigan (Ann Arbor, MI) shed light on fundamental differences of laser-matter interaction for femtosecond pulses from longer pulses. The mechanisms of laser-matter interaction are to a large extent determined by the time period to deposit energy into a material, thermal diffusion time and electron-phonon coupling time. For ultrashort pulses, laser energy is deposited at a time scale much shorter than both the heat transport and the electron-phonon coupling, the light-matter interaction process is essentially frozen in time. Subsequent electron-ion energy relaxation takes place on a much longer time scale than the laser-matter interaction time. With energy transfer from the electrons to the atomic lattice, material removal, ablation, and plasma formation occur. The irradiated zone changes from solid to vapor phase and to plasma formation almost instantaneously. Most of the locally heated materials directly vaporize because of extreme electron temperatures with many thousands of degrees Kelvin after absorption of the laser energy, though the resulting melt layer due to heat conduction also forms but the thickness of which is small [17]. For long pulses, the time of laser-matter interaction is much longer than the time of energy transfer from electrons to ions. Heat diffusion causes much larger melted volume than the focus spot. Upon absorption, the materials get molten and subsequently vaporize. Recoil pressure from the vapor flux and thermo-capillary force from the huge temperature gradient on the liquid-vapor interface provide the driving forces for melt ejection.

For ultrashort pulses with visible or near-infrared wavelength, metals and semiconductors are strongly absorbing materials. There are two characteristic lengths - the thermal diffusion length ($l_d = (k\tau)^{1/2}$, τ is the laser pulsewidth and k is the thermal diffusivity of the material) and the absorption or penetration skin depth ($l_s = 1/\alpha$, α is the absorption coefficient). When the laser pulse width τ is greater than a certain value τ_c , $l_d > l_s$ for long pulses, and the volume of laser-heated materials is determined by the heat diffusion length. Ablation occurs from both the melt and vapor phases; as a result, the zone where melting and resolidification can occur is quite extensive, and the spatial resolution of processed structures is compromised [18]. When $l_d < l_s$ for ultrashort pulses, the absorption skin depth determines material removal which occurs before the onset of energy loss due to diffusion. The ablation wave actually precedes the thermal relaxation wave so that ablation occurs from the vapor phase. Because the melt phase is minimal, ablation and material removal become highly precise. For long pulses, the fluence breakdown threshold varies with laser pulse width as $F_{th} \propto \tau^{1/2}$. For ultrashort pulses, this phenomenon is independent of pulsewidth.

In general, the ultrashort laser ablation of metals and semiconductors is a linear absorption process which means that photon energy is greater than the ionization potential due to a large density of free electrons and valence electrons in metals and semiconductors. For ablation of metals, firstly, free electron-induced impact ionization due to absorption of the laser energy results in a geometric increase in the free electron density, this is the Joule heating (inverse Bremsstrahlung) process, and then the absorbed laser energy is deposited into the thermal energy of electrons. Subsequently electron-ion energy transfer occurs after the laser pulse is over, eventually forming vapor and plasma phases followed by rapid

expansion. The ablation process can be considered as a direct solid-vapor or solid-plasma transition without the presence of the liquid phase [19]. For the covalently bonded semiconductors with small bandgaps such as Si, GaAs and InSb, the interaction mechanism is both thermal and non-thermal melting processes originating from a destabilization of the lattice in the presence of the very dense electron-hole (e-h) plasma [20]. A number of studies by time-resolved pump-probe interferometry and time of flight mass spectroscopy have been performed to clarify this laser-matter interaction process. A set of two-temperature models for titanium, gold and silicon were developed to deal with the absorption of the laser energy, specific heats of electrons and ions of materials, thermal conduction, and electron-ion energy coupling [21-23].

For transparent dielectric materials, ultrashort pulse-induced optical breakdown occurs by the nonlinear absorption or multiphoton absorption of the optical energy and ablation takes place after optical breakdown by the absorption of a plasma with “a critical density” at the surface [17]. The multiphoton absorption is a simultaneous absorption of m photons in the laser pulse such as $m h \nu \geq U_i$, where $h \nu$ is the energy of the photon, and U_i is ionization potential or bandgap. Only at very high laser field strength or in the case of ultrashort-pulse laser-matter interaction, multiphoton ionization process becomes significant and the bound electrons of the transparent material can be directly ionized (from its bound energy level or valence band to the free energy level or conduction band). This multiphoton ionization process leads avalanche ionization during which the free-electron density grows exponentially and further leads to the optical breakdown of transparent material and ablation occurs. For long pulses, it is also an avalanche ionization process but launched by impact ionization due to collision between free electron and bound electron. These free electrons

from metallic impurities, thermal or linear optical ionization of shallow energy levels of inclusions, as seed electrons for avalanche ionization, tend to fluctuate in volume. Hence, the breakdown threshold shows large statistical fluctuation. In addition, for long pulsewidth, the breakdown threshold changes as the square root of pulsewidth. In contrast to long pulsewidth, multiphoton ionization can directly provide high density seed electrons without large statistical fluctuation. Thus, the breakdown threshold becomes more deterministic. And the pulsewidth square root scaling law becomes invalid and the breakdown threshold remains constant. Once the plasma critical density for absorption of laser wavelength is reached, the material ablation begins by transferring of electron energy into lattice but this is a vaporization-dominated process due to short time of laser-matter interaction for ultrashort pulses.

Advantages of femtosecond laser micromachining

The mechanisms of ultrashort-pulse laser ablation of materials are drastically different from those of long-pulsed laser ablation. Ultrashort laser pulses have much higher laser intensity and precise laser-induced breakdown threshold. The ablation of materials with ultrashort pulses reduces heat-affected zone owing to limited thermal diffusion. These preferable characteristics offer ultrashort lasers as a competitive alternative to other cw or long-pulse lasers (Nd:YAG, Excimer, Diode pumped solid state lasers) for the laser-based micromachining industry.

Precision machining of fine features

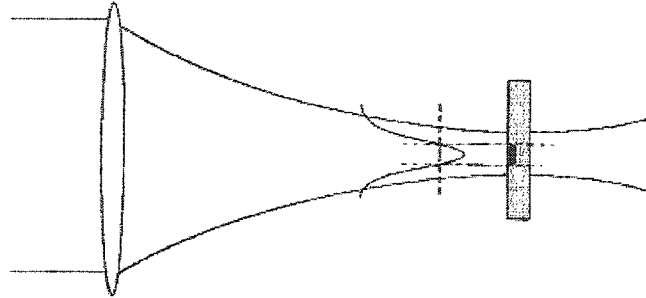


Figure 2.3. The intensity profile of the laser focus spot can be controlled so that only a small portion near the center is above the breakdown threshold. Using this geometry, sub-focus-spot-size breakdown spots can be obtained [24].

Precision of laser machining is usually determined by the smallest diffraction-limited focus spot (given as the $1/e^2$ intensity diameter of the laser focus spot) which is proportional to the laser wavelength. Ultrashort pulse lasers mostly operate in the near-IR wavelength in the 0.75-1- μm range and produce a spot size much larger than one by excimer laser in UV or DUV wavelength range. However, ultrashort lasers may provide an alternative to long-pulse (nanoseconds) excimer lasers for some precision micromachining applications. The reason is that the ablated spot size is no longer limited to laser focus spot size given by wavelength but controlled in such a way that only a small portion of the focused laser spot is above the ablation threshold due to precisely determined breakdown threshold [24]. Researchers (Pronko et al) at the University of Michigan (Ann Arbor, MI) have demonstrated that 0.3- μm holes (that is, ten times smaller than the laser spot size of 3- μm diameter) can be drilled in

silver films by working in a pulse width regime (200 fs) dominated by ablative removal and by taking advantage of the sharp fluence threshold for material removal [25].

Minimal thermal and mechanical damage

Machining with ultrashort laser pulses produce small heat-affected zone. Material goes directly into the vapor phase instead of melt phase because extremely short pulse duration does not allow propagation of heat into the surrounding material. Ultrashort light

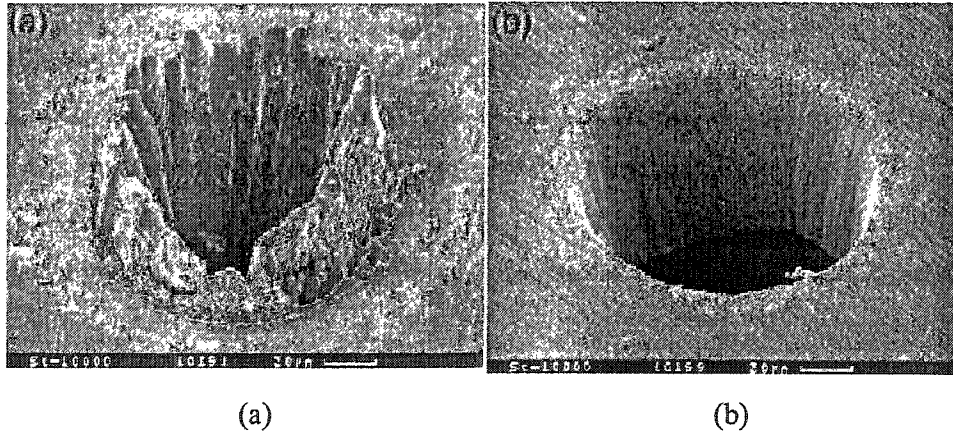


Figure 2.4. Holes drilled through a 100 mm steel foil with a pulse width of (a) 3.3 ns (b) 200 fs (Source: Applied Surface Science 109-110 (1997) 15–19)

pulse creates a solid plasma (a mixture of loosely bound ions and electrons on the surface). The plasma plume leaves the surface very rapidly – taking energy with it and consequently leaving very little energy behind to create a heat-affected zone. In addition, such adverse effects as the thermal stress fractures can be minimized due to the lack of heat conduction into the surrounding material.

Machining nearly all kinds of materials

Long pulse laser machining is essentially a single photon process, a linear process which depends upon the wavelength of light being well-matched to where the material absorbs. For ultrashort pulse machining, wavelength-dependent linear absorption is relatively marginal because a “multiphoton” or “nonlinear” process due to high laser field strength enables the laser-matter interaction to occur [26]. With this process, very hard and high melting temperature metals like Molybdenum, Rhenium, high band-gap dielectrics such as diamond, transparent and organic materials, and biodegradable materials can be machined. The other materials machined by ultrashort pulses include semiconductors, ceramics, and polymers [26-28]. Virtually, any dielectric, metal, and mechanically hard material can be machined by the same laser beam.

High accuracy and repeatability

Ultrashort pulse machining can achieve high accuracy because not only this process generates minimal heat diffusion but also the pulse does not interact at all with the plume of vaporized material, which would distort and bend the incoming beam and produce a rough-edged cut. Based on a “multiphoton process”, ultrashort laser machining has a deterministic threshold so that “shot-after-shot repeatability” can be obtained [26].

High efficiency

Generally, for most materials, using pulsewidths shorter than 10 ps, process efficiency typically increases as the pulsewidth gets shorter. For equivalent pulse energy, the peak intensity for femtosecond pulses is more than 10^4 higher than that for the nanosecond pulses, thanks to ultrashort pulsewidth, which produces a more efficient ablation process.

Also, energy loss into the bulk material is minimized, which means that the efficiency of the process is improved and the ablation energy threshold is reduced by up to two orders of magnitude depending on the material. Laser Zentrum (Hannover, Germany) has demonstrated that, for steel, the critical pulsewidth above which efficiency falls off is about 1 ps [29].

Friendly environment

Femtosecond pulsed laser in the visible and near infrared wavelength provides a competitive alternative to excimer lasers for some applications in that it does not need to handle the corrosive gases and ultraviolet radiation damage of optics like excimer lasers, though excimer lasers can achieve very fine features through their short ultraviolet wavelength and photochemical interactions [24].

Applications of femtosecond laser micromachining

The advantages of femtosecond laser-material interaction leads to precise machining of almost any material from steel to tooth enamel to very soft materials like heart tissue. The capabilities of micromachining a wide range of materials, for example, metal, glass, diamond, fluoropolymers, PMMA, silica, optical materials, masks, ceramics, biodegradable polymers and even explosives, undoubtedly show that femtosecond laser micromachining is an attractive option for numerous applications, including microelectronics and semiconductor industry, biomedicine, telecommunications and photonics, automotive and others [28]. Some emerging industrial applications include:

Biomedical applications

Researchers at Laser Zentrum Hannover (LZH) e.V.(Germany) set a good example of medical devices structured by femtosecond laser, cardiovascular medical implant (so called stent). The coronary stents are precisely slotted tubes 1-2 mm in diameter which are inserted into the vessel in order to stop the collapse or closure of arteries and ensure sufficient blood

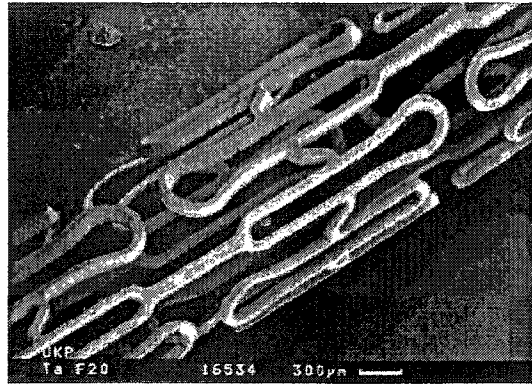


Figure 2.5. Medical implants (stents) made of tantalum by femtosecond laser. Stents are used in cardiovascular surgery. (Source: Laser Zentrum Hannover)

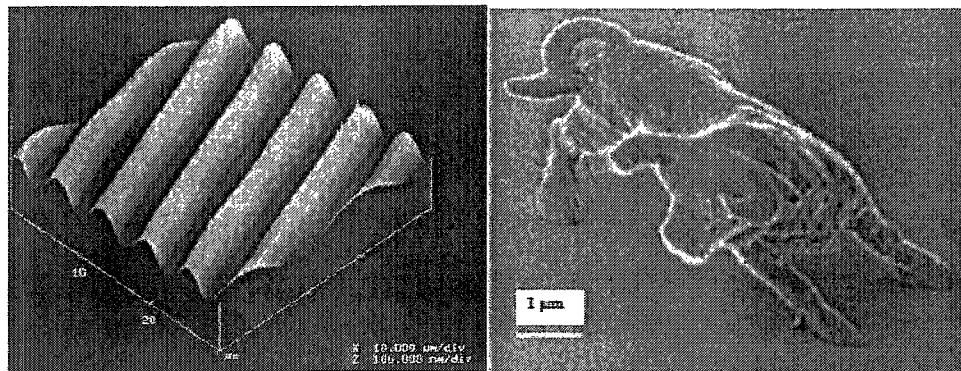
flow. Currently, stents are made of stainless steel mostly machined by nanosecond YAG lasers and post-machining is necessary to remove burr and deposited material. Femtosecond-pulse laser-machined stents are no longer limited to stainless steels but extended to a multitude of materials from the metallic to the organic, especially biodegradable polymers which can save surgical procedures for removing the stents after a certain time. And minimally invasive and damage-free stents may be obtained just one step without electropolish. Titanium-, tantalum-, biologic resorbable poly-(L-Lactide)-made stents were successfully machined by LZH/Cortronik [18,30].

Bright prospects of femtosecond laser micromachining in medicine are also encouraged by some far-reaching scientific experiments such as hole drilling on tooth [31] and pig myocardium, small hole drilling through the heart muscle (myocardium) into the inner chambers termed transmyocardial revascularization for relief from anginal pain [32], spinal and ophthalmic surgery, for example, glaucoma treatment, cataract removal [33,34]. For instance, researchers at Lawrence Livermore National Laboratory (LLNL; Livermore, CA) have produced a clean hole with no thermal damage on tooth by ultrashort pulse ablation, in contrast to a random-shaped hole with collateral damage with long pulse ablation. It goes without saying that ultrashort-pulse short energy deposition time and the high efficiency of the ablation process abate collateral mechanical and thermal damage to minimum, even for hard tissue (tooth) easily subject to shear and compressive stresses, which cause fractures and fissures when using conventional long pulse lasers.

Photonics, Micro-optics and Optical communication

Quartz is particularly challenging to micromachine using long pulse lasers. When ultrashort pulses are used to machine dielectrics including transparent materials such as quartz, precise and reproducible ablation take places with the exact ablation threshold because of multiphoton ionization process during laser-matter interaction. Consequently, ultrashort lasers expand its micromachining field to optoelectronics, micro-optics, and fiber technology. The fundamental ideas for these applications are ascribed to near infrared (IR) photosensitivity of glasses for local refractive-index change with high-intensity femtosecond pulses irradiation, absence of linear absorption for 3-dimensional processing inside bulk materials, and multiphoton ionization process for high quality of processing with low internal scattering losses due to the deterministic threshold [35]. And this technology allows for the

fabrication of optical waveguides (the change in the index of refraction when irradiated at an energy fluence below a certain threshold) and micrograting (ablation process at an energy fluence above a certain threshold) on not only glasses but non-glass materials such as polymer [36]. Direct-write 2-D or 3-D optical waveguides exhibit good stability at room temperature and offer promise for realizing compact, all-solid-state lasers and amplifiers. Taking advantage of ultrashort pulses traits of near-perfect temporal coherency and the deterministic multiphoton nature of the interaction, Kawamura and Zhai *et al* reported a two-beam holographic method to encode surface relief gratings, multi-layer micrograting and multi-dimensional nanostructures either on or beneath surface of materials [37-42]. Bragg gratings encoded in the glass fibers and glass planar waveguides are the key elements for



(a)

(b)

Figure 2.6. (a) Photoinduced holographic gratings in bulk polymer by femtosecond laser [41]. (b) Femtosecond laser photopolymerized bull sculpture by two-photon absorption (TPA) [51].

diffractive optics commonly applied to wavelength division multiplexity (WDM) communications. Kawamura *et al* also reported the formation of periodic nanostructures in crossed holographic gratings encoded on the surface of a silica glass by double-exposure techniques [43]. These periodic structures are arrays of holes with diameters of 20-300 nm, rectangular islands with a dimension of $\sim 600 \times 600$ nm or periodic grooves with the smallest width of ~ 15 nm, which are well suited for emerging applications such as photonic crystals and quantum line or dot arrays. Intense femtosecond pulses have also potential capability for the application of optical storage devices because laser-induced structural modifications can be confined to submicron size regions smaller than the focused spot. Sun *et al* demonstrated three-dimensional photonic crystal structures fabricated by near-IR femtosecond laser pulses with two-photon-absorption photopolymerization of resin [44].

Microelectronics

As the semiconductor industry drives toward even smaller feature sizes, undoubtedly, femtosecond laser-based technique finds itself right niche in microelectronics due to its unprecedented capability for precision micromachining. Its applications include precision via microdrilling and electrical paths microcutting of submicron features in microchips, repairing lithographic masks by combining scanning near-field optical microscopy with femtosecond laser pulses [45], laser etching of integrated circuits (isolating features on integrated circuits) and *in situ* repair of optoelectronic devices, which is laser surgery on light-emitting diodes to eliminate the effect of defects [46].

Automotive

Femtosecond laser application in the automotive industry is mainly microdrilling of high-aspect-ratio, high quality micro-holes for fuel injector nozzles

Others

Microfluidic systems offer potential for performing many types of biological assays, such as nucleic-acid separation, enzymes essays, immunoassays, and drug-screening. Femtosecond laser micromachining is also useful for creation of high-quality fluidic microchannels or customization of microfluidic devices [35]. But photo- and soft lithography, a major fabrication technique, is limited to two-dimensional channel structures and to feature size of about 10 μm or larger. The advantages of femtosecond micromachining lie in fabricating not only microchannels itself but also complex assembling microfluidic system by integrating the detection system with the analytical section on a single glass substrate. The advantage is to avoid the complexity and fluid loss associated with multichip designs by placing all the key components on a single chip and flexibly modifying the prefabricated microfluidic devices by adding an integrated microcapillary to a microfluidic device. Such machining technology will play an important commercial role in the manufacture of microfluidic systems

More specific and valuable scientific and commercial applications of femtosecond laser pulses are being explored, identified and utilized. Researchers at LLNL demonstrated the feasible processing of energetic materials with ultrashort pulses, which are highly sensitive to shock or thermal stress and possibly cause unintentional initiation. For example, there is a dramatic improvement in cutting PETN explosives with 150-fs compared with 500-ps pulses [47]. Mazur *et al.* at Harvard university created arrays of sharp conical spikes by repeatedly irradiating silicon surfaces with femtosecond laser pulses in SF_6 and Cl_2 . More

recently they reported that silicon surfaces microstructured in the presence of SF₆ with high-intensity femtosecond laser pulses have near-unity absorption from the near-ultraviolet (250 nm) to the near-infrared (2.5 μm) [48,49]. This finding makes microstructured silicon applicable for near-infrared photodetectors for wavelengths longer than 1.1 μm used for both telecommunications and scientific instrumentation, however, silicon itself is not used to absorb or detect light at wavelengths longer than 1.1 μm. One challenge of ultrashort laser micromachining is to surmount the diffraction limit of the optical system dependent on the radiation wavelength and capable of fabricating two- and three-dimensional sub-micron or nanostructures. One approach is to choose the peak laser fluence slightly above the threshold value by taking advantage of the deterministic ablation threshold so that the material is only modified by the central part of the beam with sub-wavelength size [24]. Another approach is to use femtosecond pulses in junction with a scanning near-field optical microscope (SNOM). For example, nanomachining line structures, complex grid patterns, and curved contours with ~10 nm spatial resolution on thin gold films was demonstrated by coupling 800-nm femtosecond laser radiation with an AFM silicon tip operated in the contact mode [50]. Another breakthrough of femtosecond laser-based nanofabrication technology was reported on sub-diffraction-limit (SDL) micro/nanofabrication via two-photon-absorption (TPA) photopolymerization. Using this technique, a lateral spatial resolution down to 120 nm by aid of high numerical-aperture optics was obtained. Various 3D microstructures (a revolvable micro-gearwheel, a micro-chain, and a micro-bull) were fabricated. TPA is promising for low-cost nanostructure fabrication for applications in optics, medicine, and biology [51].

FEMTOSECOND LASER MICRO/NANOFABRICATION OF 3C-SiC THIN FILMS ON SI SUBSTRATES

This study was proposed to develop a femtosecond laser-aided micromachining method for MEMS devices fabrication. At present, the primary technologies used for MEMS devices are the microelectronic fabrication techniques and their spin-offs which are generally limited to produce microstructures in chemically inert wide band-gap semiconductor materials and in a wide range of metallic and plastic materials. A case is SiC devices where the chemical inertness and high hardness of SiC hamper developments of SiC-based MEMS devices, realizing that such devices have potential for widespread applications under harsh environments. Femtosecond laser micromachining would be an ideal candidate to overcome the limitations associated with conventional MEMS fabrication methods. It can create three-dimensional patterns with assorted geometries in one-step (direct-write in contrast to unidirectional extensions of two-dimensional patterns with conventional lithographic techniques).

The dynamics of ultrashort laser-matter interaction has been studied by experimental and theoretical methods for various materials categorized into metals, semiconductors, and dielectrics. The accumulation of these valuable results clearly presents that femtosecond laser pulses are preferred to longer pulses in micromachining. However, in regards to the detailed dynamics of femtosecond laser ablation, the type of material raises many issues, which to some degree restricts the progress in femtosecond micromachining. Hence, it is important to have a thorough understanding of laser-matter interaction of SiC for fulfilling our goal of fabricating high-quality SiC-based MEMS structures. SiC is a semiconductor material with a wider band-gap than those commonly used Si, GaAs, InP and InSb. Its physical mechanism

is different from both narrower-than-it band-gap semiconductors and much wider-than-it band-gap insulators. However, they indeed share some common characteristics with SiC which facilitated an improved understanding of SiC ablation mechanism.

REFERENCES

1. Introduction of Laser Machining Processes: Preview of Laser Machining Process (LMP) from the World Wide Web:
<http://www.columbia.edu/cu/mechanical/mrl/ntm/Chapter1.html>
2. Common Industrial Lasers: Solid State Lasers from the World Wide Web:
<http://www.columbia.edu/cu/mechanical/mrl/ntm/level1/ch02/html/11c02s06.html>
3. Laser Machining Processes: Conventional laser machining of materials from the World Wide Web:
<http://www.columbia.edu/cu/mechanical/mrl/ntm/level1/ch05/html/11c05s05.html>
4. D.Zankowsky, "Micromachining techniques aid in manufacturing", Laser Focus World, pp.155-159 October, 1998
5. R.Srinivasan, B.Braren and R.W. Drefus, J. Appl. Phys. 61 372 1987
6. E.Hunger, H.Pietsch, S.Petzoldt and E.Matthias, Appl. Surf. Sci. 54 227 1992
7. F.V.Alvensleben, M.Gonschior, H.Kappel, and P.Heekenjann, "Laser Micromachining", Optics and Photonics News, OSA, August, 1995
8. F.Bachmann, Chemtronics, 4 149 1989
9. J.R.Lankard and G.Wolbold, Appl. Phys. A, 54 355 1992
10. D.L.Pugmire, E.A.Wadell, R.Haasch, M.J.Tarlov, and E.Locascio, Anal. Chem. 74 871 2002

11. K. Yamakawa, C. Barty, IEEE Journal of Selected Topics in Quantum Electronics, 6 658 2000
12. G.Chériaux, J.P. Chambaret, Measurement Science and Technology, 12 1769 2001
13. T.Norris, T.Sizer, and I.N.Duling, J. Opt. Lett., 18 2044 1993
14. E.J.Lerner, "Ultrafast lasers deliver powerful, precise pulse", Laser Focus World, pp.77-84 December, 1998
15. J. Mackay, "Regenerative amplifiers raise Ti:sapphire laser output", Laser Focus World, pp.83-92 October, 1997
16. G.Mourou, Appl. Phys. B, 65 205 1997
17. X. Liu and G. Mourou, "Ultrashort laser pulses tackle precision machining", Laser Focus World, pp.101-118 August, 1997
18. B. Craig, "Ultrafast pulses promise better processing of fine structures", Laser Focus World, pp.79-88 September, 1998
19. B.N. Chichkov, C. Momma, S. Nolte, F.von. Alvensleben, A.Tünnermann, Appl. Phys. A, 63 109 1996
20. K. Sokolowski-Timten, J.Bialkowski, M.Boing Phys. Rev. B 58 R11805 1998
21. S.I. Anisimov and B.Rethfeld, "On the theory of ultrashort laser pulse interaction with a metal", Proceeding of the SPIE, 3093 pp.192-203 1997
22. M.Q.Ye and C.P. Grigoropoulos, J. Appl. Phys., 89 5183 2001
23. P.P.Pronko, P.A. VanPompay, R.K. Singh, F.Qian, D.Du, and X.Liu, Mat. Res. Soc. Symp. Proc., 397 45 1996
24. X.Liu, D.Du, G. Mourou, IEEE Journal of Quantum. Electronics, 33 1706 1997

25. P.P.Pronko, S.K.Dutta, J.Squier, J.V.Rudd, D.Du, G.Mourou, *Opt. Commun.* 114 106
1995
26. T.(Ed.).DeBolt, *Handbook of Micromachining*. Ann Arbor, MI: Clark-MXR, Inc.
Retrieved December 21, 2001, from the World Wide Web: [http://
www.cmxr.com/industrial/handbook/index.htm](http://www.cmxr.com/industrial/handbook/index.htm)
27. S. Nolte, G. Kamlage, F. Korte, T.Bauer, T.Wagner, A. Ostendorf, C. Fallnich, H.
Welling. *Adv. Engg. Mater.* 2 23 2000
28. N.Z. Rizvi RIKEN Review No.50 Focused on Laser Precision Microfabrication, 107
2002
29. S. Nolte et al., *CFD3, CLEO Abstracts*, pp.510 1998
30. F.Korte, S.Nolte, B.N.Chichkov, T.Bauer, G.Kamlage, T.Wagner, C.Fallnich,
H.Welling, *Appl. Phys. A* 69 [Suppl.], S7 1999
31. Joseph Neev et al., *IEEE J. of Select Topics in Quantum Elect.* 2, 790 1996
32. J. Marion, "Ultrashort pulse laser surgery," LLNL, UCRL-MI-12940 1997
33. M. Ito et al., *J. Refractive Surg.* 12 721 1996
34. R. M. Kurtz et al., *Proc. SPIE Vol.* 3255
35. P. Bado, "MICROMACHINING: Ultrafast pulses create waveguides and
microchannels", *Laser Focus World*, pp. 73-78 April, 2000
36. K. Miura et al., *Appl. Phys. Lett.* 71 3329 1997
37. K. Kawamura, T. Ogawa, N. Sarukura, M.Hirano and H. Hosono, *Appl. Phys. B*, 71
119 2000
38. K. Kawamura, N. Sarukura, M.Hirano and H. Hosono, *Jpn. Journal of Appl. Phys*, 39
L767 2000

39. K. Kawamura, N. Sarukura, M.Hirano and H. Hosono, *Appl. Phys. Lett.*, 78 1038 2001
40. H. Hosono, K. Kawamura, K.Matsuishi and M.Hirano, *Nuclear Instruments and Methods in Physics Research B*, 191(1-4) 89 2002
41. J. Zhai, Y. Shen, J. Si, J. Qiu and K. Hirao, *J. Phys. D*, 34 3466 2001
42. Y. Lia W. Watanabe, K. Yamada, T. Shinagawa, K. Itoh, J. Nishii and Y. Jiang, *App. Phys. Lett.* 80 1508 2002
43. K. Kawamura, N. Sarukura, M.Hirano, N. Ito and H. Hosono, *Appl. Phys. Lett.* 79 1228 2001
44. H.-B. Sun, Y. Xu, S. Juodkazis, K. Sun, M. Watanabe, S. Matsuo, H. Misawa, and J. Nishii, *Opt. Lett.* 26 325 2001
45. P. Noaker, "FEMTOSECOND LASERS: Nanostructuring repairs lithographic masks", *Laser Focus World* pp.20-26 January, 2000
46. E. Dupont, X. Zhu, S. Chiu, S. Moisa, M. Buchanan, M. Gao, H. C. Liu and P. B. Corkum, *Semicond. Sci. Technol.* 15 L15 2000
47. P. S. Banks et al., *CFD2, CLEO Abstracts*, pp. 510 1998
48. T.-H.Her, R.J.Finla, C.Wu, S.Deliwala, and E.Mazur, *Appl. Phys. Lett.* 73 1673 1998
49. C.Wu, C.H.Crouch, L.Zhao, J.E.Carey, R.Younkin, J.A.Levinson, E.Mazur, R.M.Farrell, P.Gothoskar, and A.Karger, *Appl. Phys. Lett.* 78 1850 2001
50. A.Chimmalgi, T.Y.Choi, C.P. Grigoropoulos, and K.Komvopoulos, *Appl. Phys. Lett.* 82 1146 2003
51. S.Kawata, H.-B.Sun, T.Tanaka, and K. Takada, *Nature*, 412 697 2001

**CHAPTER 3. HIGH-ENERGY FEMTOSECOND PULSED LASER
MICROMACHINING OF SILICON CARBIDE COATED SILICON IN SELF-
FOCUSED AIR MEDIUM**

A paper published in the *Journal of Laser Applications* (2002)

Yuanyuan Dong and Pal Molian

ABSTRACT

The ultra-short pulsed laser ablation of silicon wafers deposited with 1 μ m thin film of SiC was performed in air medium using a 1-mJ, 120-fs, 800-nm Ti:Sapphire laser, the objective being to determine the self-focusing capability of air to produce nanostructures. The effects of pulse energy, the number of pulses, pulse repetition rate and x-y translation speed on the size, shape and thermal damage of holes and grooves were evaluated. In addition, a 200-ns pulsed, 1064-nm Nd:YAG laser was used to process grooves and the results were compared against those processed by the femtosecond pulses. Results show that holes as small as 1 μ m were produced with femtosecond pulses using the self-action property of air. Despite the capability of air medium to produce tiny holes of few μ m diameters, the shape of the hole is highly asymmetrical due to the beam profile distortion. The critical laser power for nonlinear effects of air to become effective was calculated as 40 MW. However, both the beneficial and deleterious effects of air were not found when the peak power of laser beam was under 2 GW. A comparison of femtosecond pulsed laser ablation with nanosecond pulsed laser ablation demonstrated the advantages of small size, minimal thermal damage and cleanliness for ultra-short pulses.

INTRODUCTION

Ultra-short pulsed (USP) lasers such as Ti:Sapphire offer extremely high intensity (up to 10^{21} W/cm², the equivalent of focusing the power of all sunlight falling on earth to a spot of 0.1 mm) for efficient materials processing. USP lasers are preferred over long-pulsed lasers for minimal thermal damage, small feature size, controlled removal of material, and processing materials that are otherwise difficult-to-ablate [1]. Rapid deposition of laser energy, multiphoton absorption, absence of interaction of the beam with plasma during the pulse, and lack of time for transfer of energy from electrons to lattices are responsible for reduced liquid-phase formation, collateral thermal damage, ablation threshold, and improved precision compared to the long-pulsed lasers. In micromachining with USP lasers, the area of material removed can be made smaller than the laser spot itself by restricting the ablation threshold to be only at the center of the spot. Studies on femtosecond pulsed laser micromachining performed on various materials such as Si, InP, fused silica, Al, Pyrex, α -SiO₂, and TiN [2-10] have validated these conclusions. However, one problem that confronts USP laser micromachining is the air medium through which the beam propagates. When the high intensity, ultra-short pulsed beam travels through air, there is a change in the refractive index caused by the nonlinear "Kerr" effects [11]. Consequently, several physical phenomena such as self-focusing, self-phase modulation, beam filamentation, ionization, and optical breakdown occur leading to beam distortion and poor beam quality, that in turn affect the feature profile and repeatability. It is generally recommended to use a vacuum environment for beam propagation to prevent such effects. However, vacuum processing is tedious and time-consuming with a concomitant loss in productivity, which is significant in

the industrial environment. An alternative to the vacuum uses the diffractive optical elements [12] and helium as the beam delivery medium [13].

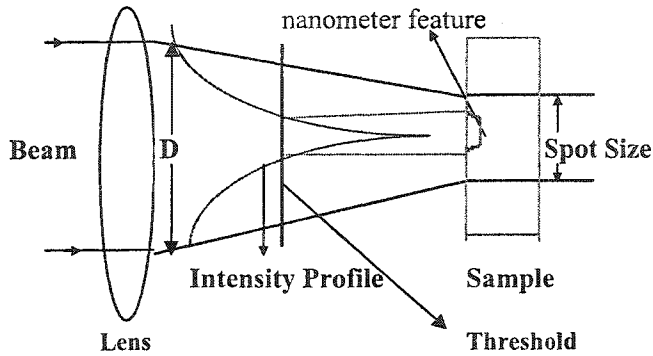


Figure 3.1. Traditional technique for producing sub-micron structures

In this work, the adverse effects of air medium on the micromachining of SiC coated Si are investigated as well as intended to generate possibly nanostructures by the self-action ability of air. The current practice to obtain sub-micron/nanoscale feature is to achieve a small spot by controlling the intensity profile of USP lasers in such a way that only a fraction of the spot size is above threshold energy fluence (Figure 1). In this way, researchers have demonstrated that the machined feature size can be smaller than the spot size. For example, a 60-fs laser with a 5- μm focused spot could produce an 800-nm hole in SiO_2 [9]. Similarly, 300-nm diameter holes were drilled in silver films using a 200-fs laser focused to a spot size of 3- μm [4]. Another example is the creation of 500-nm diameter holes in copper and silicon using a 500-fs laser [10]. The chief limitation of this technique is very low material removal rates due to low energy availability. Therefore, if nanostructures by femtosecond laser pulses in self-focused air medium become possible, not only ablation rate for micromachining will

be greatly increased, but also low energy, a harsh condition for producing nanostructures by femtosecond laser pulses, won't be necessary.

Micromachining with femtosecond laser pulses is of growing interest for the fabrication of semiconductor and MEMS devices. Laser micromachining challenges traditional and mature chemistry fabrication techniques from the perspectives of high flexibility and high repeatability of patterning to high ablation efficiency and high resolution [2-4]. Silicon (Si) is a technologically important material for semiconductor and microelectromechanical systems (MEMS) applications. Silicon carbide (SiC), an emerging semiconductor material, outperforms Si for high frequency, high-power, high-temperature and high-radiation microelectronic devices because SiC has a wider bandgap, higher breakdown field, higher thermal conductivity and higher saturation velocity than Si. In addition, SiC has a higher Young's modulus and mechanical hardness, which when combined with its electrical properties, makes SiC an attractive alternative to Si for MEMS devices, such as pressure sensors and accelerometers to be used in harsh temperature, wear, chemical, and radiation environments [14]. However, both bulk and surface micromachining of SiC structures were severely hampered by the chemical inertness of the material. While many researchers have investigated USP laser ablation of Si, no work is reported on the same for SiC thin films deposited on silicon. SiC has an absorption coefficient of 63cm^{-1} at 532 nm [15], about 16 times smaller than Si (1000 cm^{-1} at 800-nm) [16] and make the laser beam difficult to ablate. However, the USP laser by virtue of its high-intensity is capable of correcting this deficiency through multiphoton absorption. In addition, it can be an excellent alternative to reactive ion etching (RIE) which suffers from low etch rate, dimensional control, and poor selectivity in micromachining SiC. In this paper, the results of a study using

a 120-fs pulsed Ti:Sapphire laser for micromachining Si substrate/3C-SiC thin film are presented.

SELF-FOCUSING OF AIR MEDIUM

The self-focusing of laser beams in nonlinear media such as air was introduced by Chiao et al., in U.S. [17] and by Talanov in Russia [18] and continued by other researchers [19-29] with a large body of theoretical and experimental work using a variety of lasers such as Ruby, Q-switched Nd: YAG, mode-locked Nd: Glass, and Ti:Sapphire. When an intense laser beam propagates through a nonlinear medium whose refractive index increases with field intensity, it creates its own optical waveguide and transmits without diffraction spreading. The refractive index of the nonlinear medium (n) is the sum of the linear refractive index of the medium (n_0) and the refractive index change (δn) which the laser field induces:

$$n = n_0 + \delta n = n_0 + n_2 I \quad (3-1)$$

where n_2 is the nonlinear refractive index and I is the intensity of the laser beam. Since the laser beam has an inherently non-uniform intensity distribution, the intensity-dependent index of refraction (δn) causes different parts of the beam to propagate with different phase velocities. A lens effect is thus produced whereby the rays move toward the region of higher intensity, reducing the spot size. Thus, self-focusing is an inductive lens effect and is attributed to the clustering of molecules, anisotropy, electron distortion, orientation of asymmetric molecules in the presence of strong optical fields, and size of molecules.

Self-focusing of the laser beam is responsible for the formation of filaments which eventually destroy the beam through scattering and absorption. The transverse spatial inhomogeneities caused by a variety of factors such as optical surfaces and edges of apertures grow exponentially with laser power and generate filaments [26]. These filaments can be further divided into hyperfine filaments before the beam is completely destroyed [26]. However, the filament formation can be tailored to produce nanostructures, an objective of this work.

The extent of nonlinear effects of self-focusing and/or filamentation is characterized by the B-integral, defined by [30]:

$$B = \frac{2\pi}{\lambda} \int_0^l n_2 I(z) dz \quad (3-2)$$

where “ l ” is the distance of the focal point from the beam entry point of the lens and “ z ” is the position of beam along the beam path. The critical value for B that causes nonlinear effects is reported to be greater than 3-5 [30]. This value is easily exceeded for the USP laser beam in air with typical laser parameters. For example, consider the laser and process parameters used in this work: $L = 57$ mm (thickness of lens = 7 mm, distance between lens and focal point = 50 mm), $E = 0.9$ mJ, $\tau = 120$ fs. Under these conditions and taking n_2 as 12×10^{-19} cm²/W [31] and for a Gaussian beam, $I_0 = 2P/\pi w_0^2$, $I(z) = 2P/\pi[w(z)]^2$, $w(z) = w_0 [1 + (\lambda z/\pi w_0^2)^2]^{1/2}$, $B = 27.8$ (see the Appendix for calculations). This value is much higher than the value of 8.3 reported by Momma et al. [12], but it might be due to the fact that Momma et al. used a smaller value (3×10^{-19} cm²/W) for n_2 . In any event, the large value of B suggests the high probability for nonlinear effects to occur.

The critical or threshold power required for self-focusing a laser beam in a nonlinear medium is given by [26]:

$$P_c = \epsilon_0 n_0 C \lambda^2 / 4\pi n_2 \quad (3-3)$$

where ϵ_0 = vacuum permittivity, $8.85 (10^{-12})$ Farad/meter or ampere.sec/volt.meter, n_0 = linear refractive index, C = velocity of light (3×10^8 meter/sec), λ = wavelength of light (800 nm), and n_2 = nonlinear refractive index, meter²/Volt².

For air medium using a 1064-nm light, the nonlinear refractive index is $4.56 (10^{-24})$ m²/V² [26]. An interpolation of this data for 800-nm gives rise to an approximate value of $3.5 (10^{-24})$ m²/V² for n_2 . The critical power for self-focusing of 800-nm light by air is calculated as 40 MW. The ultra-short pulsed beam used in this work has a rated peak power of about 8 GW (1-mJ, 120-fs) and is more than adequate for self-focusing the 800-nm beam in air.

The self-focusing length Z_f is given by:

$$Z_f = Z_R / (P/P_c - 1)^{1/2} \quad (3-4)$$

where Z_R is the Rayleigh range given by:

$$Z_R = \pi w_0^2 / \lambda \quad (3-5)$$

where w_0 is the beam waist radius.

For the laser parameters of 1 mJ pulse energy, 120 fs pulse width, 800 nm wavelength, 40 μm spot size used in this work, Z_R and Z_f are 1.6 mm and 0.1mm respectively.

In an ideal case, a self-focusing beam will continue to focus until its radius reaches zero at the self-focus point. However, in a real medium, such as air, self-focusing continues until the medium breaks down thus creating a plasma and stopping the beam [26]. In addition, attenuation phenomenon limits the self-focusing range and keeps the beam intensity below the breakdown threshold. Furthermore, scattering and turbulence reduce the self-focusing distance.

The nonlinear self-focusing effects induced by the air can break the beam into intense filaments of light, only a few microns in diameter especially at increased intensity. The dimension of the filaments is given by [26]:

$$a_f = (a_0 / 2) (n_0 P_c / P)^{1/2} \quad (3-6)$$

where a_0 is given by $w_0 / \sqrt{2}$. For the parameters used in this work, the filament diameter calculated using equation (3-6) is 0.5 μm . The duration of filaments is shown to be about few nanoseconds [22]. Therefore, the filaments are capable of machining the material. Multiple holes can also be generated with a single beam especially at higher intensities because of the small-scale focusing [29] that breaks the beam into numerous filaments and due to the presence of group velocity dispersion in the medium [28,32] that splits the original pulse.

EXPERIMENTAL DETAILS

One μm thick 3C-SiC films were heteroepitaxially grown on 0.54-mm thick Si (100) wafer in an atmospheric pressure chemical vapor deposition (APCVD) reactor using a two-step growth process described in detail elsewhere [33]. An 800-nm wavelength, 1-mJ Ti:Sapphire oscillator-amplifier system (Spectra-Physics, Model Hurricane X) based on a chirped-pulse-amplification (CPA) technique was used to ablate the wafer under atmospheric pressure. Details of the CPA technique may be found elsewhere [2]. The laser emitted 120-fs pulses of linearly polarized light with near Gaussian beam ($M^2=1.5$) at a central wavelength of 800-nm (photon energy = 1.55 eV). The beam diameter was 6 mm. The laser was operated in single-shot mode, as well as in continuous-shot mode at pulse frequencies of 100 Hz to 1 kHz. The prepulse contrast ratio was 1000. The beam, steered through a 45° reflecting mirror and focused using a 50-mm focal length fused silica lens, was incident perpendicular to the sample surface. A circular spot was formed, the size of which was calculated as $40 \mu\text{m}$ based on the experimental data described in the next section. A 20x refractive objective lens was also used in few experiments. For comparison purposes, a Q-Switched Nd:YAG laser micromachining system (Florod, Model MEL-40) with a wavelength of $1.06 \mu\text{m}$ and a pulse width of 200 nanoseconds was used to process grooves. The MEL-40 laser micromachining system includes Labview™ and robotic work handlers, which are controlled by a personal computer and built-in CCTV. The repetition rate and energy of the Nd:YAG laser used were 1 kHz and 0.8 mJ respectively.

Prior to laser processing, each sample was cleaned with methanol and mounted on a motorized x-y stage (Coherent LabMotion Series) which has a repeatability of $1 \mu\text{m}$ and a resolution of $1 \mu\text{m}$. Two sets of experiments were conducted in air ambient. First, a series of

holes was drilled by varying the number of pulses and pulse repetition rates. Second, a set of grooves was ablated by varying the pulse energy and x-y translation speed. The number of laser pulses was controlled by an electronic shutter (UNIBLITZ VMM-T1) which incorporates two precise timers to control shutter exposure and delay intervals.

A number of analytical instruments were used to measure and characterize the kerf, hole size, hole taper, aspect ratio, recast layer, crack formation, surface roughness, and chemical contamination. An optical microscope (500×) was used to measure the dimensions of holes and grooves as well as examine surface damage. A surface profilometer (Veeco Instruments Inc. Solan technology Division, Dektak IIA, vertical resolution: 0.5 nm) served to measure the depths of holes and grooves. A scanning electron microscope (SEM) (JEOL JSM 840, 10 kV accelerating voltage) operated with secondary electrons and the associated energy dispersive X-ray spectrometer was used to examine the laser machined features and analyze the composition of debris and recast layer.

RESULTS AND DISCUSSION

Calculation of Spot Size and Ablation Threshold

The spot size of the beam at the focal region was calculated from the measurements of the dimensions of laser-irradiated regions and using the spatial fluence profile of a Gaussian beam given by:

$$F(r) = F_0 \exp(-2r^2/w_0^2) \quad (3-7)$$

where r = distance from the beam center, $w_0 = 1/e^2$ radius and

$$F_o = \text{maximum fluence} = 2 E/\pi w_o^2 \quad (3-8)$$

where E = pulse energy.

The diameter D of an ablated region can be directly related to the maximum fluence as [34]:

$$D^2 = 2w_o^2 \ln (F_o/F_{th}) \quad (3-9)$$

where F_{th} = material-dependent threshold fluence.

A plot of the square of damage diameter, D^2 , against the logarithm of energy fluence was made to obtain both the spot size (slope of line) and ablation threshold (the extrapolation of D^2 to zero value). The spot size, $2w_o$, was determined as $40 \mu\text{m}$.

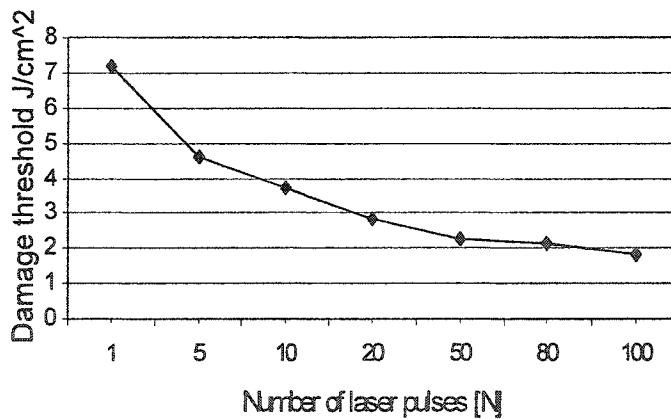


Figure 3.2. Ablation threshold versus the number of laser pulses for SiC film on Si

Sub-micron structures are usually obtained at the laser fluence just above the damage threshold of ablation and, hence, it is important to estimate this data. Figure 3.2 shows the effect of the number of pulses on the damage threshold calculated from the experimental

data. The damage threshold dramatically drops after the first laser pulse and reaches saturation after 100 laser pulses. Similar behavior was observed in other materials such as metals, ceramics, and polymers [7,34]. The reduction in damage threshold results from the laser-induced defect sites that accumulate during the first few laser shots and the incubation effects after very high number of laser shots [35].

Ablation threshold can also be obtained from the fundamental physics equation. Evaporation occurs when [3]:

$$C_i T_i = \rho \Omega T \quad (3-10)$$

where C_i = volumetric specific heat of lattice (J/m^3K), T_i = lattice temperature due to laser heating (K), ρ is the density ($kg\ m^{-3}$), Ω is the specific heat of evaporation ($J/kg\ K$) and T is evaporation temperature (K). F_{th} is then given by:

$$F_{th} = \rho \Omega T / \alpha \quad (3-11)$$

where α is the absorption coefficient (cm^{-1}). Table 1 shows the thermal properties of Si and SiC from which F_{th} can be obtained. There is a good agreement on ablation threshold for a single pulse between theoretically calculated value of SiC and experimentally calculated data shown in Figure 2.

Ablation threshold for multiple pulses, $F_{th}(N, \tau)$, can be related to the single-pulse threshold by a power law equation [7]:

$$F_{th}(N,\tau) = F_{th}(1,\tau) \cdot N^{S-1} \quad (3-12)$$

S characterizes the degree of incubation causing the surface fatigue. Experimental data were used to fit equation (12) to obtain the value of S as 0.72. Bonse et al. [36] obtained an S value of 0.78 for InP in air using a 130-fs, 800-nm Ti:Sapphire laser.

Table 3.1. Ablation threshold, F_{th} , from thermal and optical properties.

Property	Si	3C-SiC
Density, kg/m ³	2320	3,210
Specific heat, J/kg K	710	72
Evaporation Temperature, K	3540	2073
Absorption coefficient, cm ⁻¹	1000 [16]	63 [15]
Ablation threshold, J/cm ²	5.17	6.55

Laser Processing of Holes

Figures 3.3a and 3.3b are the scanning electron micrographs showing the effect of the number of pulses (N) on the size of hole and damage morphology using a constant pulse energy of 1 mJ in *single-shot mode*. The formation of 1- μ m diameter holes is attributed to the effect of self-focusing characteristic of air. There is evidence of thermal damage in the form of cracking, melting and solidification around the holes. Columnar cell structures and periodic ripples at the periphery of the melted layer were observed. The periodicity of ripples was the same as the wavelength of light. There was significant collateral thermal damage surrounding the hole when the number of pulses was increased from 20 and 50. This is

somewhat expected since it has been shown that brittle materials undergo fracturing and cracking at high-energy fluence [6].

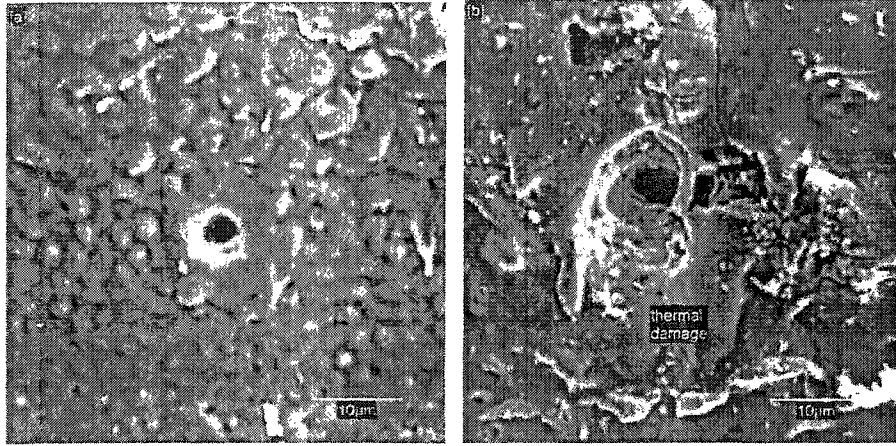


Figure 3.3. SEM images of laser microdrilled silicon at 1 mJ in air in single-shot mode (a) N=20 (b) N=50 (N= the number of pulses)

Figure 3.4 shows the damage morphology of the sample surface obtained when the laser beam was impinged on the surface at 1 mJ for 50 pulses in *continuous-shot mode* at 1kHz. The laser power was about 200 times higher than the critical power for self-focusing. The presence of several tiny holes with diameters less than few μm is believed to be a result of uncontrolled, self-focusing filamentation phenomenon. The irregular shape of the damage is again due to the air medium creating the spatial inhomogeneities in the energy distribution of the Gaussian beam profile through ionization and attenuation.

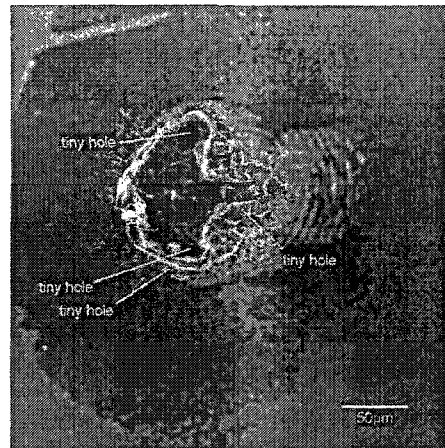


Figure 3.4. SEM image of laser irradiated surface at 1mJ, 1 kHz, N=50 in continuous-shot mode. Note the presence of several tiny holes.

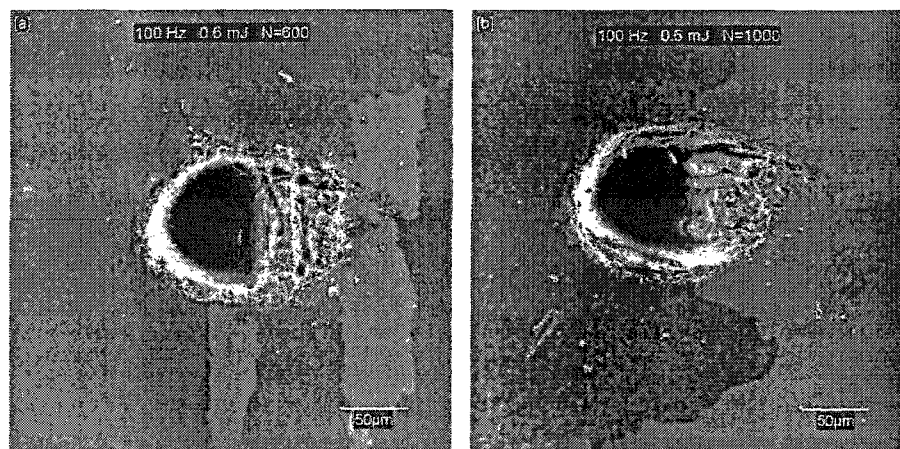


Figure 3.5. SEM images of laser microdrilled holes at 0.6 mJ in continuous-shot mode
(a) N=600, (b) N=1000, (c) N=3000

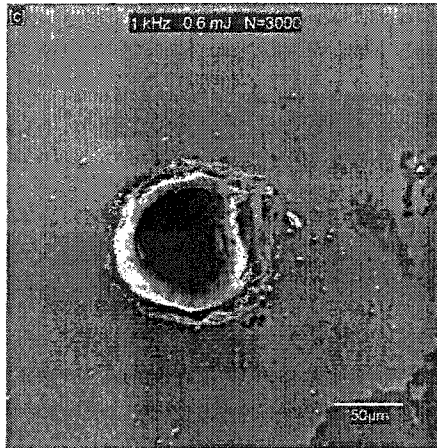


Figure 3.5 continued

Figures 3.5a to 3.5c show the holes drilled as a function of number of pulses at a reduced energy of 0.6 mJ (continuous-shot mode) but still the laser power is 125 times that of the critical power for self-focusing. These holes are irregular in shape, and the left sides are much closer to being circular than the right sides. Some tiny holes can be seen on the right side. Such effects are induced by the air medium by distorting the beam profile and producing filaments. These effects, however, are reduced with increasing N, as seen in Figure 3.5.

Figure 3.6 shows the holes drilled using a low pulse energy of 0.25 mJ (peak power 2 GW) and a 20× refractive objective lens instead of conventional fused silica lens. The application of the objective lens can further reduce the spot size on the sample surface. The holes were smaller and uniform than the holes shown in Figure 3.5, suggesting that the air medium did not have a deleterious effect on the beam profile. The absence of tiny holes also reflects that self-focusing did not become effective for laser power 50 times more than the critical power for self-focusing. There is a significant amount of residue surrounding the hole

possibly due to the material condensation and “extrusion” mechanism of material removal.

The chemical composition of the debris was identified as silicon oxide.

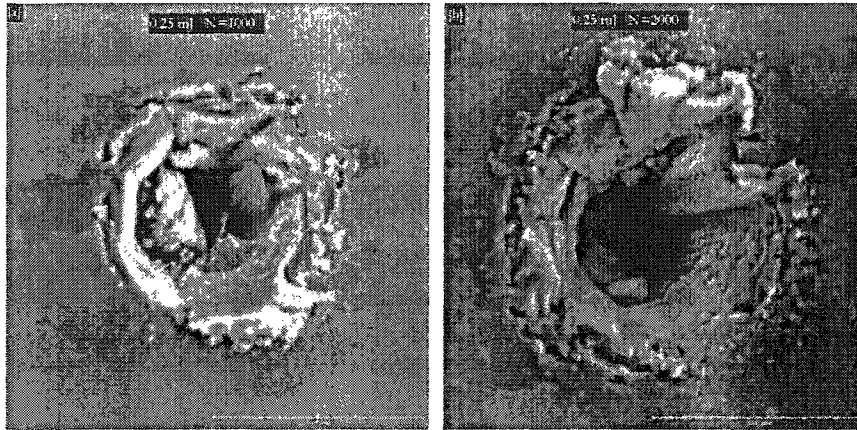
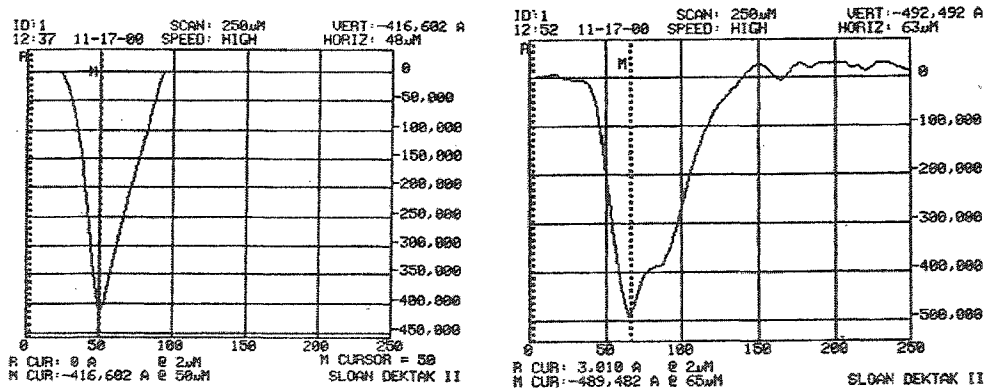


Figure 3.6. SEM images of holes at 0.25 mJ using a 20× objective lens in continuous-shot mode (a) N=1000 (b) N=2000 (c) N=5000



(a)

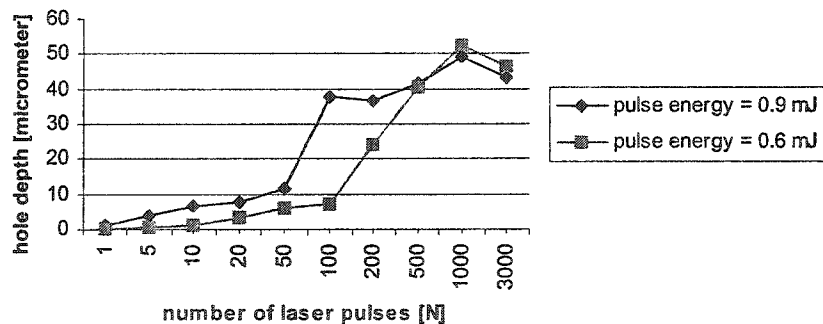
(b)

Figure 3.7. Profilometer traces of holes. Laser parameters: 1 kHz and 0.9 mJ.

(a) N= 500 (b) N=1000

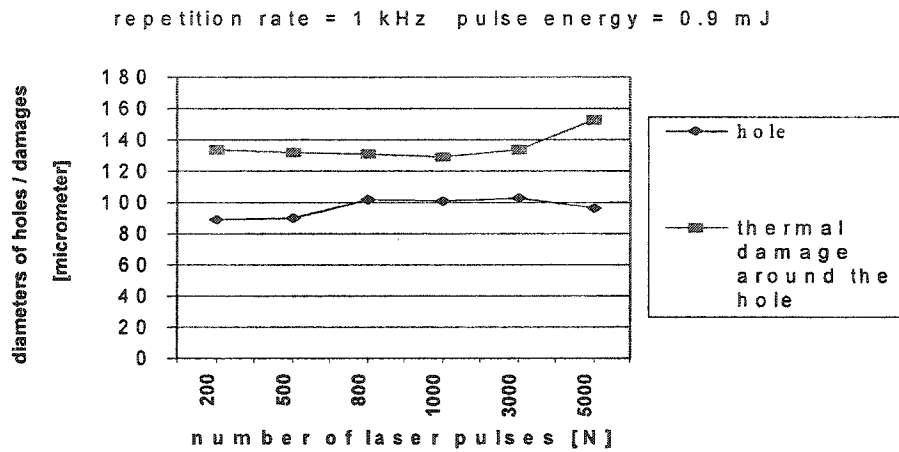
Figures 3.7a and 3.7b are the profilometer traces of holes exposed to 500 laser pulses and 1000 laser pulses respectively (1 kHz, 0.9 mJ). There is a large taper with a material

removal rate of about 0.8- μm per pulse. It is also seen that an increase in number of pulses had a greater effect on the diameter than on the depth. Figure 3.8 shows plots of hole depth, diameter, and damage size against the number of pulses. The ablation depth increases with increasing number of pulses, as expected. However, there is a slight decrease in ablation depth when pulse numbers exceeded 1000. This is mostly due to a combination of several effects such as evaporated species falling back into the hole, energy loss through the walls of the hole by reflection and material re-deposition. It may be seen in Figure 3.8a that the removal of the 1- μm 3C-SiC layer was achieved in 2 laser shots at the pulse energy of 0.9-mJ and 10 laser shots at the pulse energy of 0.6 mJ. The number of pulses had a marginal effect on the diameter of the hole and the associated thermal damage zone surrounding the hole implying that ultra-short pulsed laser ablation is a unidirectional process.

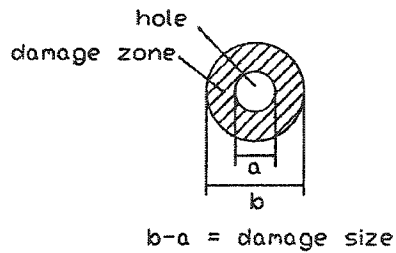


(a)

Figure 3.8. (a) Hole depth versus the number of pulses as a function of pulse energy at 1 kHz (b) Diameters of holes and thermal damages for various pulses at a constant pulse energy of 0.9 mJ and 1 kHz (c) A schematic diagram showing the definitions of hole and damage regions. Here “a” and “(b-a)” are defined as diameters of holes and damages, respectively.



(b)



(c)

Figure 3.8 continued

Laser Processing of Grooves

The relative motion between the focused laser beam and the sample generates grooves. Figures 3.9a and 3.9b show the effect of increasing translation speed for the pulse energy of 0.8 mJ (single scan) on cutting depth and width. It is seen that the cutting depth decreases more drastically than cutting width. Similar effects were observed when the pulse energy was increased. Figures 3.10a and 3.10b show the details of grooves as a function of the type of laser used. Femtosecond-pulsed laser produced well-defined cuts with narrow

width and little recast layer and less thermal damage compared to nanosecond-pulsed laser. There is sufficient evidence in literature [1,3,4,12,37] that the nanosecond-pulsed laser produces grooves with a high degree of damage at the edges than the femtosecond-pulsed laser. In USP lasers, the laser energy deposition into electrons occurs in less time than the

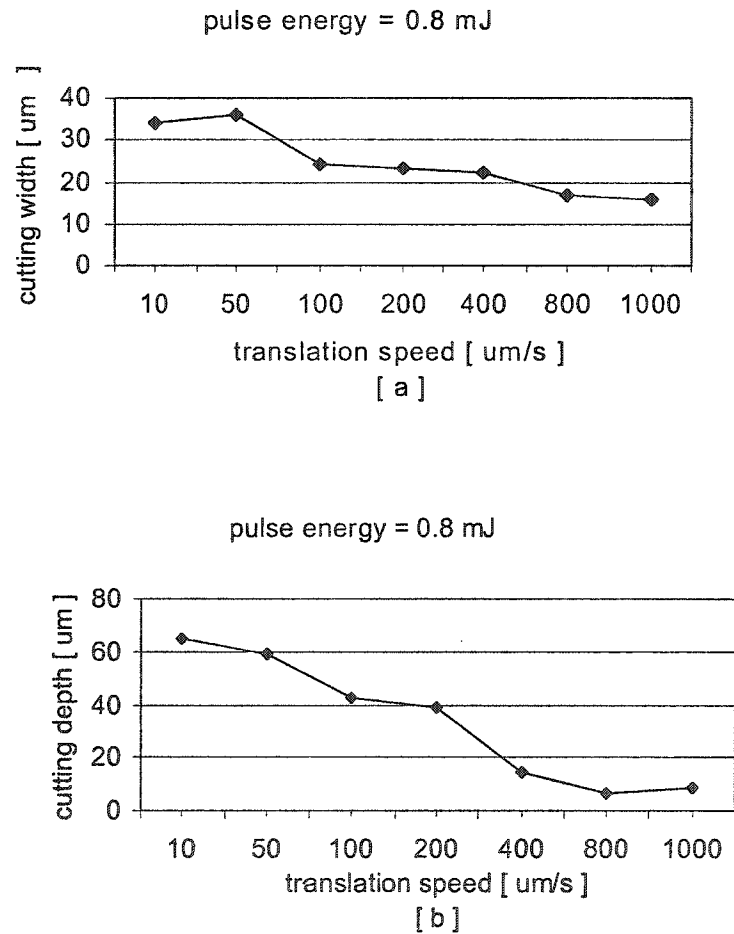


Figure 3.9. The effect of translation speed on (a) cutting width (b) cutting depth at a pulse energy of 0.8 mJ.

transfer time to lattice, and the heat diffusion involves much larger volume than the focus volume. The shorter pulse duration (than electron-phonon coupling time) of the USP lasers limits the heat conduction and results in a greater degree of precision, especially for metals and semiconductors because there is a large density of free electrons and valence electrons with an ionization potential less than the photon energy. When the absorption depth is smaller than the diffusion length ($\sqrt{D\tau}$ where D is the thermal diffusivity and τ is the pulse width) – generally valid for long pulses - the melt expulsion and associated fluid flow accompany the material removal, resulting in low precision. When the pulse length is reduced to ultra-short pulse range, the absorption depth becomes greater than the diffusion length leading to the localization of energy within the depth and, consequently, causing direct vaporization resulting in high precision.

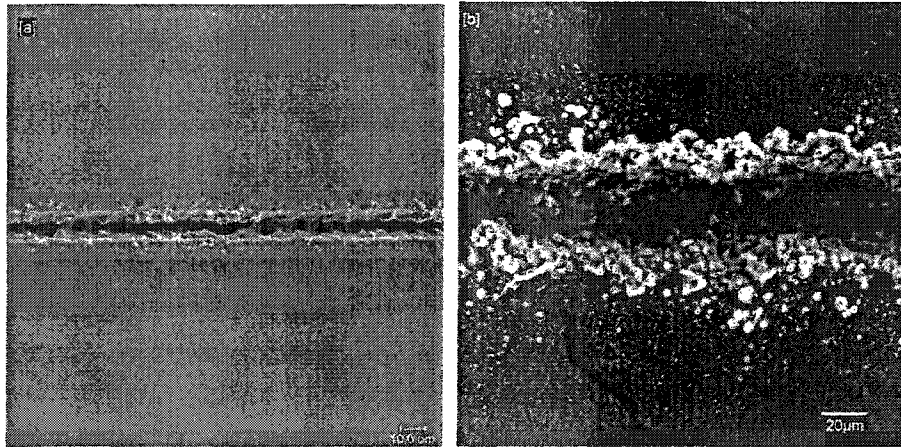


Figure 3.10. SEM images of laser-cut grooves at 0.8 mJ using (a) Femtosecond laser 120fs, 1KHz (b) Nanosecond laser 200ns, 1KHz.

CONCLUSIONS

In this work, we have demonstrated the nonlinear effects of air medium in ultra-short pulsed ablation for producing small features (beneficial effect) and uncontrollable geometry of ablated regions (deleterious effect) in micromachining. It is further shown that the effects of self-focusing were not effective until the peak power of the beam exceeded 50 times that of the critical power for self-focusing. The damage threshold of SiC was in good agreement with theoretical prediction. It is concluded that the femtosecond laser has potential as a micromachining tool for producing Si/SiC devices.

ACKNOWLEDGEMENTS

The authors would like to acknowledge the National Science Foundation (NSF) for supporting this research work under the grant DMI-9978633. Thanks are also due to Professor Marc Porter for providing the Surface Profilometer Facility.

REFERENCES

1. M.D. Shirk and P.A. Molian, *J. Laser Appl.*, 10- 1, (1998) 1-11
2. J X. Zhao, B. Huttner and A. Menschig, *SPIE* Vol. 3618, (1999) 114 –121
3. B.N.Chichkov, C.Momma, S. Nolte, F.von Alvensleben, and A. Thunermann *Appl. Phys. A63* (1996)109 –115
4. P.P. Pronko, S.K. Dutta, J. Squier, J.V.Rudd, D. Du,and G. Mourou, *Opt. Commun.* 114 (1995) 106-110
5. X.Zhu, D.M. Villeneuve, A. Yu. Nauma, S. Nikumb, and P. B. Corkum. *Appl. Surf. Sci.* 152 (1999) 138-148

6. D.Ashkenasi, M. Lorenz, R. Stoian, and A. Rosenfeld, *Appl. Surf. Sci.* 150 (1999) 101-106
7. J. Bonse, P.Rudolph, J. Krüger, S.Baudach and W. Kautek, *Appl. Surf. Sci.* 154-155 (2000) 659-663
8. S.Ameer-Beg, W.Perrie, S. Rathbone, J. Wright, W.Weaver and H.Champoux, *Appl.Surf. Sci.* 127-129 (1998) 875-880
9. X. Liu and G. Mourou, *Laser Focus World*, August, 1997, 101-118
10. P. Simon and J. Ihlemann, *Appl. Phys. A*, 63, (1996) 505-508
11. A.E. Siegman, Lasers, University Science Books, Sausalito, California, 1986
12. C. Momma, S. Nolte, G. Kamlage, F. Alvenslebn, and A. Thunnermann, *Appl. Phys. A*, 67, (1998) 517-20
13. J. Sun and P. Longtin, *Therm. Sci. and Eng.*, 7(6), (1999) 81-85
14. M. Mehregany, C.A. Zorman, N. Rajan, and C.H. Wu, *Proc. IEEE* 86, (1998) 1594 – 1610
15. G. L Harris Properties of Silicon Carbide, Published by: INSPEC, the Institution of Electrical Engineering, London, United Kingdom (1995)
16. I. W. Boyd, Laser Processing of Thin Films and Microstructures, Springer-Verlag, Berlin Heidelberg (1987) 36
17. R.Y. Chiao, E. Garmire, and C.H. Townes, *Phys. Rev. Lett.*, 13, (1964) 479
18. V.I. Talanov, *Radio Phys. (Translation)*, 7, (1964) 254
19. Akhmanov, S.A., A. P. Sukhorukov, and R. V. Khokhlov, *Soviet Physics JETP*, 23, 6, December, (1966)1025-1033
20. P.L. Kelley, *Phys. Rev. Lett.*, 15, 26, December, (1967) 1005-1008

21. R. Brewer and C.H. Lee, *Phys. Rev. Lett.*, 21, 5, (1968) 267-270
22. R. Brewer, J. R. Lifshitz, E. Garmire, R.Y. Chiao, and C.H. Townes, *Phys. Rev.*, 166, 2, (1968) 326-332
23. V. Zakharov, V.V. Sobolev, and V.C. Synakh, *Soviet Physics JETP*, 33, 1, 1971,77-81
24. C.A. Sacchi, Lasers and Their Applications, (Ed) A. Sona, Gordon and Breach, New York, 561-578, 1976
25. A. Ashkin, J.M. Dziedzic, and P. W. Smith, *Opt. Lett.*, 7, 6, (1982) 276-278
26. R.I. Miller and T.G. Roberts, *Appl. Opt.*, 26, 21, (1987) 4570-4575
27. D. Strickland and P.B. Corkum, *J. Opt. Soc. Am. B*, 11,3, (1994) 492-497
28. A. Brodeur, F.A. Ilkov, and S.L. Chin, *Opt. Commun.*, 129, (1996) 193-198
29. A. Brodeur and S.L. Chin, *Phys. Rev. Lett.*, 80, 20, (1998) 4406-4409
30. P. Maine, D. Strickland, P. Bado, M.Pessot, and G. Mouro, *IEEE J. Quant. Electron.*, QE-24, (1988) 398
31. M.J. Shaw, C.J. Hooker, and Wilson, D.C., *Opt. Commun.*, 103, (1993) 153-160
32. J.E. Rothenberg, *Opt. Lett.*, 17, 8, (1992), 583-585
33. C.A. Zorman, A.J. Fleischman, A.S. Dewa, M. Mehregany, C. Jacob, and P. Pirouz, *J. Appl. Phys.*, 78 (1995) 5136-5138.
34. J. Gudde, J.Hohlfeld, J.G. Muller, and E. Matthias, *Appl. Sur. Sci.*, 127-129, (1998) 378
35. D. Ashkenasi and A. Rosenfeld, *SPIE Vol. 3618* (1999) 102 -113
36. J. Bonse, J.M. Wrobel, J. Kruger, and W. Kautek, *Appl. Phys. A*, 72, (2001) 89-94

37. B.C. Stuart and M.D. Feit, *Phys. Rev. Lett.*, 74, 12, (1995) 2248–2251

CHAPTER 4. FEMTOSECOND PULSED LASER ABLATION OF 3C-SiC THIN FILM ON SILICON

A paper published in the *Applied Physics A: Materials Science & Processing* (2003)

Yuanyuan Dong and Pal Molian

ABSTRACT

A femtosecond pulsed Ti:sapphire laser (pulse width = 120 fs, wavelength = 800 nm, repetition rate = 1 kHz) was employed to perform laser ablation of 1- μm -thick silicon carbide (3C-SiC) films grown on silicon substrates. The threshold fluence and ablation rate, useful for the micromachining of the 3C-SiC films, were experimentally determined. The material removal mechanisms vary depending on the applied energy fluence. At high laser fluence, a thermally dominated process such as melting, boiling and vaporizing of single-crystal SiC occurs. At low laser fluence, the ablation is a defect-induced Coulomb explosion process via photo absorption of defects, excitation of electrons, formation of repulsive electrostatic field, and ejection of ions and neutral particles. The defect-activation process reduces the ablation threshold fluence and enhances lateral and vertical precision as compared to the thermally dominated mechanism. Helium, as an assistant gas, plays a major role in improving the processing quality and ablation rate of SiC thin films due to its inertness and high first ionization energy.

INTRODUCTION

Silicon carbide is an outstanding semiconductor material for high-frequency, high-power, high-temperature and high-radiation microelectronic devices because it has a wider band-gap, higher breakdown field, higher thermal conductivity and higher saturation velocity than Si. In addition, SiC has a higher Young's modulus and mechanical hardness, which when combined with its electrical properties, makes SiC an attractive alternative to Si for microelectromechanical systems (MEMS) device structures, such as pressure sensors and accelerometers to be used in harsh temperature, wear, chemical, and radiation environments [1]. Until recently, fabrication of micromachined SiC structures was severely hampered by the chemical inertness of the material. Unlike for Si, there are no known wet etchants that could be used to bulk micromachine device structures from SiC substrates. In fact, SiC is so resistant to wet chemical etching that many in the field refer to SiC as nature's best etch-stop material. Alternative methods to wet chemical bulk micromachining are being developed that include deep reactive ion etching (DRIE) and micromolding [2]. Presently, DRIE of SiC lacks the dimensional control and etch rates, and micromolding associated with Si DRIE requires several additional processing steps to create and eventually dissolve the Si molds, although it is successful in creating structures with complex 3D topographies.

Like SiC bulk micromachining, SiC surface micromachining is also a very difficult task. The most direct means to pattern SiC structural layers is reactive ion etching (RIE). RIE-based surface micromachining processes have been successfully used to fabricate single-structural-layer devices such as cantilever beams and lateral resonant structures; however, issues related to the micromasking of the etch field, low etch rates and poor selectivity to silicon and silicon dioxide sacrificial layers currently restrict the use of RIE in SiC surface

micromachining. Micromolding techniques have been developed to pattern SiC surface-micromachined structural layers [2], but as in the case of bulk micromachining, the use of micromolds increases the processing steps.

Micromachining with femtosecond laser pulses is of growing interest for the fabrication of semiconductor devices [3, 5, 6, 15]. Laser micromachining challenges traditional and mature chemistry fabrication techniques from the perspectives of high flexibility and high repeatability of patterning to high ablation efficiency and high resolution [3–5]. In micromachining with ultrafast laser pulses, the area machined can be made much smaller than the laser spot itself by restricting the light intensity threshold to be only at the center of the spot. Additionally, the multi-photon excitation of femtosecond laser pulses dramatically reduces heat conduction and thermal damage to the surrounding material [6, 7]. Studies on femtosecond laser micromachining performed on various materials such as Si, GaN, InP, TiN, fused silica, Pyrex, α -SiO₂, YLF and Al [3–6, 8–11] have validated these conclusions. In this paper, the results of a study using a 120-fs pulsed Ti:sapphire laser for the micromachining of 3C-SiC films are presented. The threshold fluence, ablation rate and mechanism of ablation were investigated. We will show that high-quality laser-surface processing can be best obtained at low fluence (defect-activated regime) irradiation for high laser shots.

EXPERIMENTAL DETAILS

About 1- μ m-thick 3C-SiC films were heteroepitaxially grown on 0.54-mm-thick Si(100) in an atmospheric pressure chemical vapor deposition (APCVD) reactor using a two-step growth process described in detail elsewhere [12]. A Ti:sapphire oscillator–amplifier

system (Spectra-Physics, Model Hurricane X), based on a chirped-pulse-amplification (CPA) technique was used to micromachine the 3C-SiC films. Details of the CPA technique may be found elsewhere [7]. The 120-fs laser was operated at a wavelength of 800 nm and a repetition rate of 1 kHz with a maximum single-pulse energy of 0.9 mJ. The linearly polarized light had a near-Gaussian beam quality with a pre-pulse contrast ratio of 1000. A set of neutral density (ND) filters was utilized to attenuate the beam intensity. The experimental set-up is shown in Fig. 4.1. Prior to laser processing, each sample was rinsed and cleaned in acetone and methanol and mounted on a motorized x - y stage (Coherent LabMotion Series), which had a repeatability of 1 μm and a resolution of 1 μm . Two sets of experiments were conducted in ambient air and helium. The first was a series of holes drilled by varying pulse energy using single pulses. The second was a series of holes ablated by varying the number of laser pulses at a given pulse energy. The number of laser pulses was controlled by an electronic shutter (UNIBLITZ VMM-T1), which incorporated two precise timers to control shutter exposure and delay intervals. A scanning electron microscope (SEM) (JEOL JSM 840, 10-kV accelerating voltage) in the secondary-electron mode was used to examine the laser-machined features and measure the depth of holes by a method of stereo depth measurement.

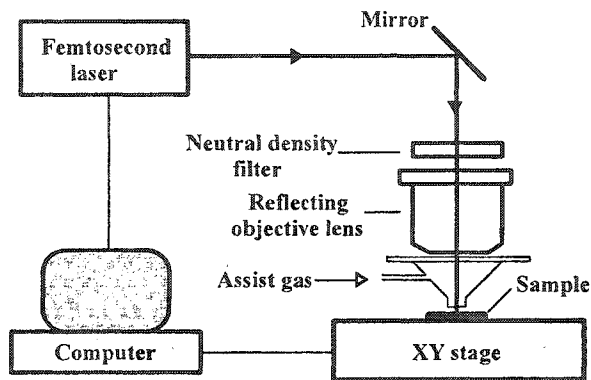


Figure 4.1. A schematic representation of a laser micromachining set-up

EXPERIMENTAL RESULTS AND DISCUSSION

Ablation morphology

The SiC film on Si was exposed to single laser pulse at a series of pulse energy levels ($7 \mu\text{J}$, $10 \mu\text{J}$, $13 \mu\text{J}$, $20 \mu\text{J}$, $27 \mu\text{J}$ and $33 \mu\text{J}$) in the ambient air. One laser shot was used to avoid processing the Si substrate. Figure 4.2 shows SEM images for these laser-induced surface morphological features with different pulse energies. The permanent damage is visible on the surface of SiC films. The elliptically damaged regions are sub-divided into three different zones that arise from the spatial distribution of Gaussian beam intensity: modification (the border of the spot), oriented ripples [13, 14] and ablation, corresponding to the peak intensity of the Gaussian laser beam. With increasing pulse energy, a crater is gradually formed and becomes larger at the center of the spot. Furthermore, the re-deposition of the material is also seen around the crater (Fig. 4.2c and d). In addition, the three zones are enlarged and the ripples are enhanced with an increase of pulse energy. The three-zone surface morphology is typical and is commonly observed in the laser-induced surfaces of such materials as InP and Si [15, 16].

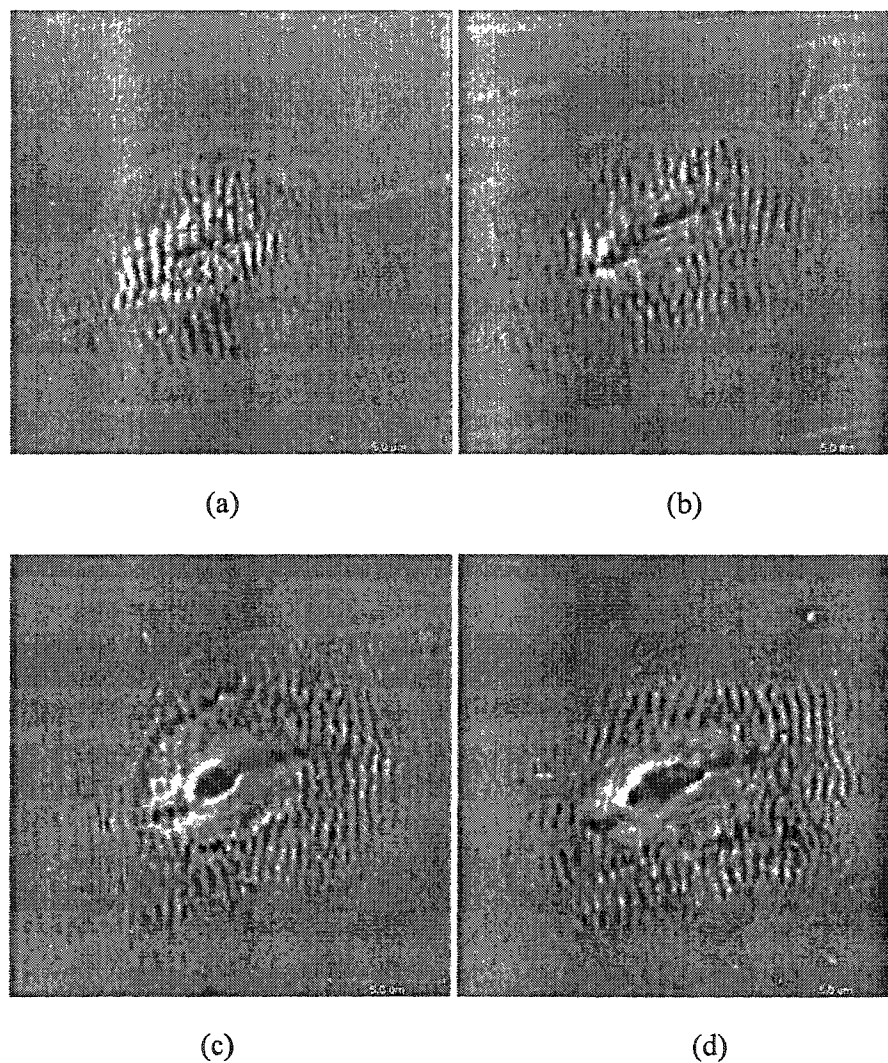


Figure 4.2. SEM images of laser-induced 3C/SiC surface morphology for a single pulse in air: a 7 μJ ; b 13 μJ ; c 20 μJ ; and d 27 μJ

The SiC film on Si was exposed to multiple pulses at a constant pulse energy of 7 μJ in the ambient air and helium. Figure 4.3 shows that the laser irradiation has penetrated into the Si substrate beginning at the center of the spot, based on the fact that a depth of 4 μm was obtained at the center of the crater with only five laser pulses (Fig. 4.3a). This depth is four-

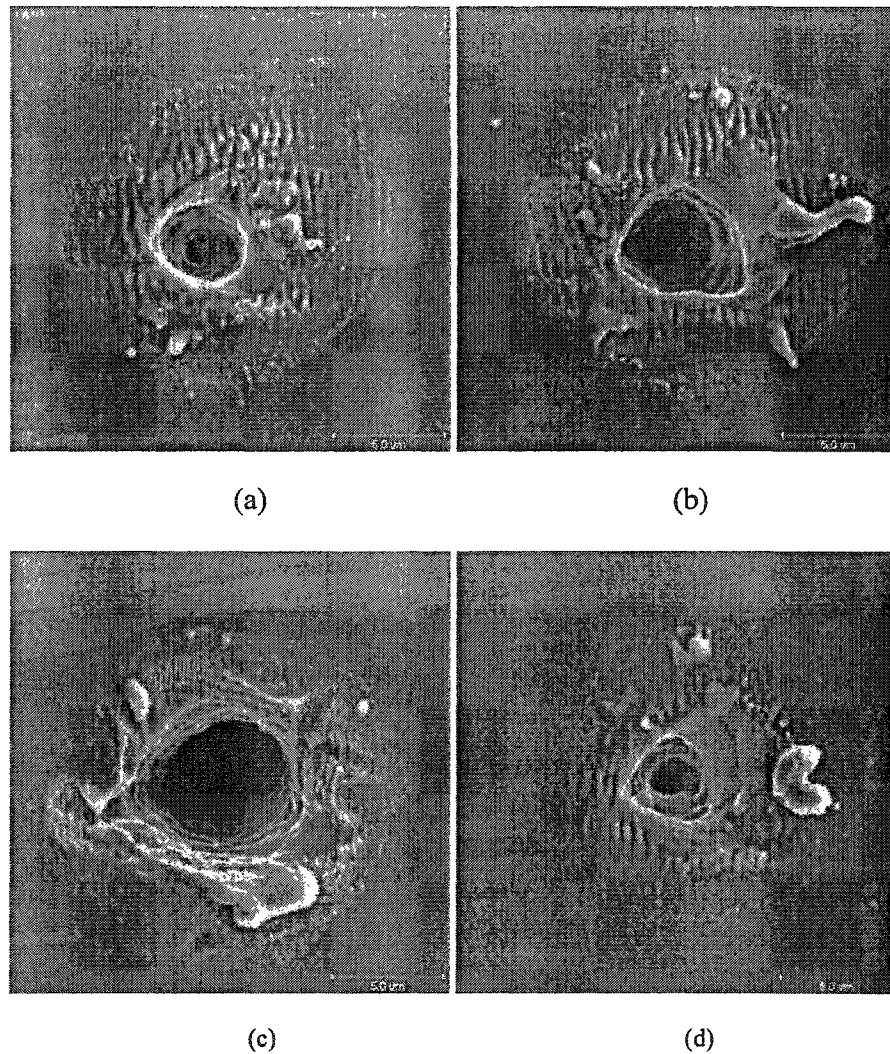


Figure 4.3. SEM images of laser-induced 3C/SiC surface morphology at $7 \mu\text{J}$ in air: a 5 pulses; b 10 pulses; and c 100 pulses, and in helium: d 5 pulses

times greater than the thickness of SiC film. Si substrate is not a laser etch stop for SiC film because Si has a higher absorption coefficient and a lower threshold fluence than SiC at 800 nm, 120-fs laser irradiation [16–18]. Apparently, compared with the processing of a single pulse, the damaged areas also increase with increasing number of pulses, but not as dramatically as with the increase of pulse energy. The depth of the crater at the center of the

spot becomes deeper with increasing number of pulses. The ripple pattern has disappeared with the increase of the cavity. At the top surface of the holes, outwardly extruded material is observed (Fig. 4.3b and c). For identical laser parameters, compared with the processing (Fig. 4.3a) in air, laser processing in helium (Fig. 4.3d) reduces the amount of thermal damage and decreases the modified area. Clearly, the processing quality is improved in the helium environment. Besides, depth measurement for the cavity at the center of the spot shows that the cavity is made deeper by using helium as an assistant gas than by using air. The chief reasons for the less modified area and the higher ablation rates in helium at the high fluence regime are attributed to helium's low nonlinear refractive index and high first ionization potential [19]. Its low non-linear refractive index reduces non-linear beam distortion and then decreases the processed feature size [19]. Its high first ionization potential decreases and/or suppresses the formation of plasma that otherwise damages the surface of materials and makes the laser beam interact mainly with the materials and not with the gas environment.

It is evident that thermal transport dominates the processing of SiC films in this high-energy regime because the ablation region is surrounded by significant thermal damage, termed a heat-affected zone (HAZ). Increase of the HAZ, phase change and re-deposition were all observed with increasing pulse energy and number of pulses.

In order to shrink the size of the laser-induced features in the SiC films and improve the processing quality, a lower pulse energy of 0.2 μJ was employed. Theoretically, feature size less than the spot size could be obtained by applying the pulse energy slightly above threshold value.

Figure 4.4 illustrates laser-induced features exposed to multiple pulses at 0.2 μJ in ambient air and helium. It is worth noticing that at such a low pulse energy there is no

indication of typical thermal damage, like cracking, ripples, columns and recast, frequently observed at high pulse energy. The most interesting feature is the development of nanoparticles with a size of 100–200 nm in the irradiated areas. The SEM image of the fracture section of the virgin SiC film, shown in Fig. 4.5, demonstrates that the SiC film is not comprised of such structures. Based on their arrangements in the cavity, the nanoparticles are a result of exposure to the laser. For the first few pulses, SEM did not detect any damaged zone in the SiC films. A nearly round and shallow crater with diameter much less than the spot size of the Gaussian beam (a $1/e^2$ -beam radius of $4.98 \mu\text{m}$ is calculated in Sect. 3.3) was produced at 50 pulses (Fig. 4.4a). With increasing number of pulses, the depths of the cavities increased, and the shapes shifted to ellipses with an increasing ratio of long axis to short axis, which is a direct consequence of the linear polarization of the beam. After 200 laser pulses, the edges of the cavities became not well-defined (Fig. 4.4d). These results suggest that at the low laser fluence the SiC film was processed via laser-induced defect formation and accumulation, formation of nanoparticles and final ablation on the irradiated surface [9]. The formation of nanoparticles in the helium environment (Fig. 4e and f) implies that oxidation mechanism does not contribute to the growth of the nanoparticles. The morphological features are quite different from the three damaged zones, characteristic of thermally dominated processing at high pulse energy. The clean ablation of SiC film without any re-deposition of material and evident thermal damage in the surrounding area suggests a non-thermal mechanism effect governing the processing of SiC films in the low-energy regime. When the pulse energy was increased above $0.2 \mu\text{J}$, SiC films were penetrated through and tiny holes appeared on the Si substrate.

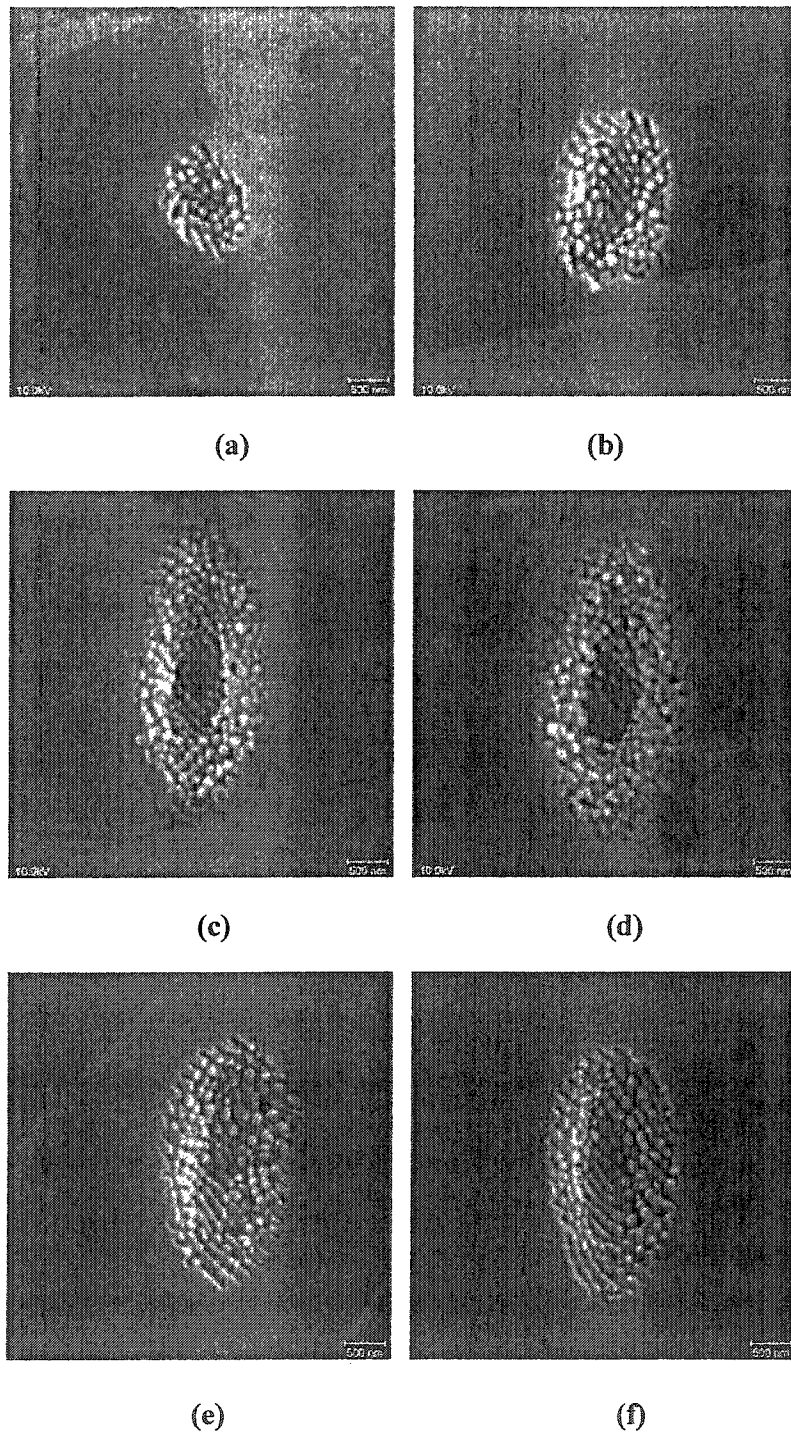


Figure 4.4. SEM images of laser-induced 3C-SiC surface morphology at 0.2 μJ in air: a 50 pulses; b 100 pulses; c 200 pulses; and d 500 pulses, and in helium: e 100 pulses and f 200 pulses

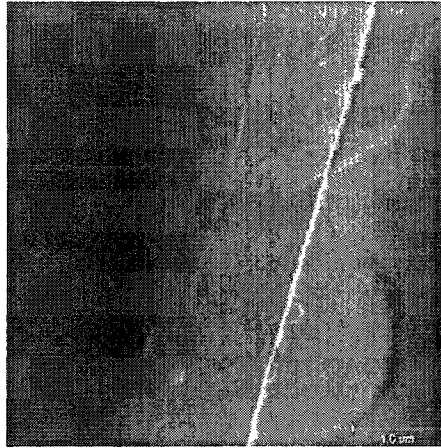


Figure 4.5. SEM image of the fracture section of the single-crystalline SiC film

Ablation rate of SiC film at low laser fluence

A high ablation rate is an attractive figure of merit for femtosecond laser etching compared with chemical etching. Because laser processing at low energy limits the ablation depth within the SiC films, a pulse energy of $0.2 \mu\text{J}$ was appropriate to study the relationship between ablation depth and the number of pulses. Figure 4.6 shows a linear relationship between depth and the number of pulses after $N = 50$ and less than 500 pulses. Beyond 500 pulses, ablation depth in air reached saturation, which obviously resulted from the fixed focal distance from the focus point to the sample. Approximately, an ablation rate of 100 nm/pulse before reaching to saturation was determined from the slope of the linear function. Because of this relationship, the etch depth can be controlled by the number of the pulses. Moreover, the saturation of processing depth can be avoided by appropriate adjustment of the focal distance. This etching technique is useful in the fabrication of electronic devices with thin multilayers, as well as MEMS devices. The etch rate for photoelectrochemical etching (PEC) of SiC is around $1 \mu\text{m/min}$ [18]. Clearly, laser etching of SiC has a faster rate than PEC

etching, even at such a low energy. Furthermore, Fig. 4.6 shows that a higher ablation rate is achieved in helium than in ambient air. A similar result is also observed at high fluence, as shown in Fig. 4.3. It is possibly because helium has very high first ionization potential, which suppresses the plasma formation and makes the laser beam interact solely with materials and not with the environment gas. Thus, ablation depth in helium is increased. Helium also has a low non-linear refractive index which refrains self-focusing action [19]. However, if at a certain low fluence, which is below the ambient gas ionization threshold and cannot trigger other non-linear phenomena, another explanation could be that helium cannot be easier absorbed onto the surface than oxygen in air during processing because of its inertness. Absorbed oxygen has no effect on forming nanoparticles rather than reducing the ablation rate. Existence of absorbed oxygen in the irradiated area of SiC processed in air can be detected from the result of Auger Emission Spectroscopy.

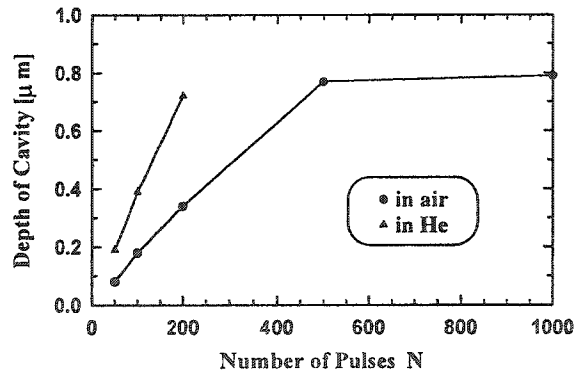


Figure 4.6. Depth of the laser-generated cavities versus the number of laser pulses N applied to 3C-SiC in air ($\tau = 120$ fs, $\lambda = 800$ nm, $\phi_0 = 0.52$ J/cm²)

Threshold fluence

It is of fundamental interest to determine the threshold fluence under ultrafast laser irradiation for a wide band-gap material like SiC because the choice of the operating laser

fluence relative to the threshold fluence has a significant influence on the size, shape and quality of the laser-induced features. What is more significant is that the threshold fluence plays a key role in affecting the ablation mechanism of SiC films.

In accordance with Si morphological features generated by 100-fs laser irradiation [16], the laser-induced SiC films at single laser pulse and 7 μJ consist of three distinct regions (Fig.4.2): modification zone, ripple zone and ablation zone, each of which corresponds to their own threshold fluence. In order to identify these threshold fluences, the diameter D of the modification zones and ripple zones was measured using SEM images and software (Quartz PCI, version 4.0). The pulse energies used for calculation were 7 μJ , 10 μJ , 13 μJ , 20 μJ , 27 μJ and 33 μJ . From the equations [10, 20]

$$\phi_{\max} = \phi_o = 2E/\pi\omega_o^2 \quad (4-1)$$

$$D^2 = 2\omega_o^2 \ln\left(\frac{\phi_o}{\phi_{th}}\right) \quad (4-2)$$

a Gaussian $1/e^2$ -beam radius of $\omega_o = 4.98 \mu\text{m}$ was obtained as the slope of linearly fitting the square of the diameter of the measured area versus the pulse energy. Two threshold fluences, $\phi_{th} (1) = 0.97 \text{ J/cm}^2$ for the modification zone and $\phi_{th} (1) = 3.29 \text{ J/cm}^2$ for the ripple zone were obtained by linearly fitting the square of the diameter of the modified area versus the logarithm of the pulse fluence and extrapolating it to zero (D is equal to zero), as shown in Fig. 4.7. Because the minimal laser fluence used in the experiment of Fig. 4.2 reached 17.11 J/cm^2 , much higher than the above threshold fluences, it is no surprise that the three morphological zones occurred and that the center of the spot underwent thermal processes like melting, vaporizing and re-solidifying due to such a high laser fluence from the peak of Gaussian beam.

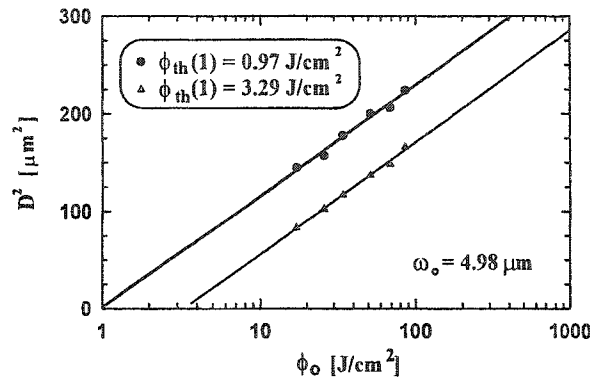


Figure 4.7. Squared diameters, D^2 , of the modification and the ripple areas as a function of the applied laser fluences for single-pulse processing ($\tau = 120$ fs, $\lambda = 800$ nm) of 3C-SiC in air, respectively

For the experiments in Fig. 4.4, the diameter of the modified area for each hole at different number of pulses was measured and the laser fluence ϕ_0 was calculated as 0.52 J/cm^2 from (4-1). Thereby, the damage threshold fluences at different number of pulses were obtained using (4-2): $\phi_{th}(50) = 0.489$ J/cm^2 , $\phi_{th}(100) = 0.458$ J/cm^2 , $\phi_{th}(200) = 0.434$ J/cm^2 , $\phi_{th}(500) = 0.419$ J/cm^2 and $\phi_{th}(1000) = 0.415$ J/cm^2 . It is noted that the damage threshold fluences decrease with increasing laser shots until reaching saturation after 500 laser shots. Considering the presence of the incubation effects which take place within the first few pulses, the laser shot number dependency of the damage threshold $\phi_{th}(N)$ should satisfy the following model [9]:

$$\phi_{th}(N) = \phi_{th}(\infty) + [\phi_{th}(1) - \phi_{th}(\infty)]\exp[-k(N-1)] \quad (4-3)$$

where k is an empirical parameter indicating the strength of the defect accumulation and the increase in photon absorption. Although a more accurate estimate of the first threshold $\phi_{th}(1)$ cannot be obtained because of the lack of $\phi_{th}(N)$ before $N = 50$, the single-pulse threshold ϕ_{th}

(1) of 0.519 J/cm^2 for defect-activated surface damage is smaller than the modification threshold fluence of 0.97 J/cm^2 we have obtained in Fig. 4.7. As can be seen from Fig. 4.8, an apparent process of defect accumulation exists during ablation at low fluence. After defect accumulation, the surface damage threshold is rapidly reduced and reaches a constant level of $\phi_{\text{th}}(\infty)$. At a fluence below $\phi_{\text{th}}(\infty) \approx 0.415 \text{ J/cm}^2$, the irradiation would require an infinite number of pulses to initiate defect accumulation and then activate ablation. This result is consistent with the fact that no damage was detected by SEM in the SiC films processed under a pulse energy of $0.1 \mu\text{J}$.

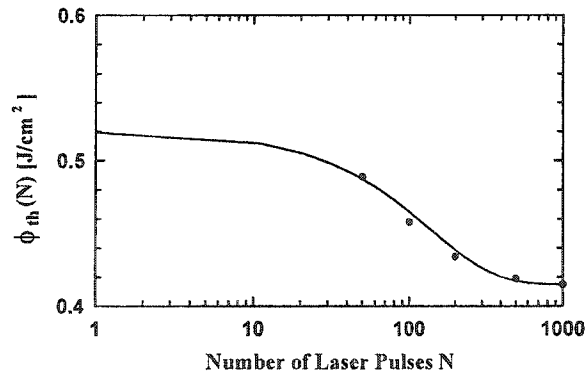


Figure 4.8. The surface-damage threshold as a function of the number of laser pulses N at low processing fluence for the ablation ($\tau = 120 \text{ fs}$, $\lambda = 800 \text{ nm}$) of 3C-SiC in air. The *solid line* represents the result from the fit following model (4-3): here, $\phi_{\text{th}}(1) = 0.519 \text{ J/cm}^2$, $\phi_{\text{th}}(\infty) = 0.415 \text{ J/cm}^2$ and $k = 0.00755$

Ablation mechanism

According to our experimental results, two kinds of laser-induced surface morphology occur, depending on the laser fluence. One is a classical heating, melting, boiling and vaporization or phase explosion process that occurs at high fluence (Fig. 4.2) and is characterized by three surface damage zones, indicative of slight modification, ripple and

ablation. The second is a non-thermally-dominated process at low fluence (Fig. 4.4), characterized by a very clean processing profile and nanoparticles in the SiC films.

A thermal transport model for femtosecond laser processing of semiconductors [16, 21, 22] was utilized to explain the features of the SiC films in Fig. 4.2. For a beam with Gaussian energy distribution coupling with the SiC, the temperatures developed will vary along the spot. The slightly modified zone at the periphery of the exposed spot is in an amorphous state because here the low temperature of the molten material leads to the rapid solidification of material. The ripple zone of the exposed area exhibiting nanoparticles with size of about 100 nm is represented in Fig. 4.9. At the center of the spot with the largest amount of energy deposition, the superheated top layer transforms into gas bubbles composed either of single atoms or of several molecular species and is removed from the SiC film. Consequently, a crater is left on the surface.



Figure 4.9. SEM image of the ripple zone: an amorphous phase and nanoparticles with a size of about 100 nm, resulting from re-crystallization

Pulsed laser ablation is a well-known technique for the preparation of nanoparticles through condensation and/or decomposition of vapors in inert gases [23, 24]. The

nanoparticles begin to grow above the ablation spots, slightly apart from the targets, based on the condensation and/or decomposition of vapors [25, 26]. However, we present that at low laser fluence the formation of laser-induced nanostructures does not result from condensation and/or decomposition but from defect-activation, which prevents the thermal processing described in the conventional micromachining model (in Fig. 4.4). Firstly, at low laser fluence, nanoparticles are not observed on silicon around but in the crater. Secondly, the incubation effects take place at low processing fluence. The mechanism of defect activation is also observed in ion-induced nanostructure formation, driven by defect generation [27].

Strictly speaking, 3C-SiC film is not an ideal crystal without any lattice defects above absolute zero temperature. The pre-existing defects facilitate local absorption of laser [16], especially for SiC, which has a quite low absorption coefficient at a wavelength of 800 nm. Crystalline SiC can be driven to further lattice disorder by electronic excitation resulting from the absorption of laser energy after the onset of laser irradiation because the electronic excitation might weaken the inter-atomic bonding and thus lower the vibrational energy required to produce disorder [28, 29]. With increasing laser-induced lattice defects, the photo absorption is enhanced and electrons are intensely excited from valence band to conduction band and electron-hole plasma is formed. However, due to lagging recombination, a repulsive electrostatic field is built up and ultimately starts on the ejection of ions and neutral particles. As a result, nanocraters are formed all over the SiC film surface and a nanoparticle-like surface is observed. This ablation mechanism starts from a defect-activation process and needs a much lower laser fluence than that involving intense phase transformation mostly induced by multiphoton absorption. The lower threshold fluence thus allows the processing

of smaller and cleaner features for the application of device micromachining. A more detailed study of the laser-induced formation of nanoparticles is underway.

CONCLUSION

Femtosecond laser-induced surface morphology and ablation of 3C-SiC films were investigated for different laser parameters. The differences in the morphology of the damage surfaces were used to explain different laser ablation mechanisms for the processing of SiC thin films. Four threshold fluences were observed for such phenomena as slight modification, ripple, crater and defect-activated ablation. At high laser fluence, SiC film was ablated through melting, boiling and vaporizing from the single crystal. At low laser fluence, however, the ablation mechanism of SiC film was a defect-activation process including defect accumulation, photo absorption of defects, excitation of electrons, formation of repulsive electrostatic field, and ejection of ions and neutral particles, and formation of nanoparticles with a size of 100–200 nm. Therefore, high-quality processing of SiC films with well-defined edges can be obtained based on the defect-activated mechanism. Helium, as an assistant gas, can improve the processing quality and the ablation rate of SiC thin films because of the ability of helium to prevent self-focusing, its high first ionization potential and inertness. We believe that defect-activation is not only a practical technique that can micromachine SiC-based MEMS with well-defined edges but also a promising means to pattern confined nanostructures, expanding the range of possible applications.

ACKNOWLEDGEMENTS

The authors would like to acknowledge the National Science Foundation (NSF) for supporting this research work under Grant No. DMI-9978633. We thank Dr. C. Zorman and Dr. M. Mehregany (Department of Electrical Engineering and Computer Science, Case Western Reserve University, Cleveland, Ohio 44106, USA) for providing the 3C-SiC thin film sample and helpful discussions. Thanks are also due to Dr. W.E. Straszheim for providing SEM characterization.

REFERENCES

- 1 M. Mehregany, C.A. Zorman, N. Rajan, C.H. Wu: Proc. IEEE **86**, 1594 (1998)
- 2 M. Mehregany, C.A. Zorman: Thin Solid Films **355–356**, 518 (1999)
- 3 J.X. Zhao, B. Huttner, A. Menschig: Proc. SPIE **3618**, 114 (1999)
- 4 B.N. Chichkov, C. Momma, S. Nolte, F. von Alvensleben, A. Tünnermann: Appl. Phys. A **63**, 109 (1996)
- 5 K. Ozono, M. Obara, A. Usui, H. Sunakawa: Opt. Commun. **189**, 103 (2001)
- 6 P.P. Pronko, S.K. Dutta, J. Squier, J.V. Rudd, D. Du, G. Mourou: Opt. Commun. **114**, 106 (1995)
- 7 X. Liu, D. Du, G. Mourou: IEEE J. Quant. Electron. **QE-33**, 1706 (1997)
- 8 X. Zhu, D.M. Villeneuve, A.Y. Nauma, S. Nikumb, P.B. Corkum: Appl. Surf. Sci. **152**, 138 (1999)
- 9 D. Ashkenasi, M. Lorenz, R. Stoian, A. Rosenfeld: Appl. Surf. Sci. **150**, 101 (1999)
- 10 J. Bonse, P. Rudolph, J. Krüger, S. Baudach, W. Kautek: Appl. Surf. Sci. **154–155**, 659 (2000)

- 11 S. Ameer-Beg, W. Perrie, S. Rathbone, J. Wright, W. Weaver, H. Champoux: *Appl. Surf. Sci.* **127–129**, 875 (1998)
- 12 C.A. Zorman, A.J. Fleischman, A.S. Dewa, M. Mehregany, C. Jacob, P. Pirouz: *J. Appl. Phys.* **78**, 5136 (1995)
- 13 Z. Guosheng, P.M. Fauchet, A.E. Siegman: *Phys. Rev. B* **26**, 5366 (1982)
- 14 J.F. Young, J.E. Sipe, H.M. Van Driel: *Phys. Rev. B* **30**, 2001 (1984)
- 15 J. Bonse, J.M. Wrobel, J. Krüger, W. Kautek: *Appl. Phys. A* **72**, 89 (2001)
- 16 J. Bonse, S. Baudach, J. Krüger, M. Lenzner: *Appl. Phys. A* **74**, 19 (2002)
- 17 I.W. Boyd: *Laser Processing of Thin Films and Microstructures* (Springer-Verlag, Berlin, Heidelberg 1987) p. 36
- 18 G.L. Harris: *Properties of Silicon Carbide* (Inst. Electrical Eng., London (1995)
- 19 J. Sun, J.P. Longtin: *Therm. Sci. Eng.* **7**, 81 (1999). The first ionization energy (kJ/mol) of the following elements are: H, 1312.0; He, 23 272.3; N, 1402.3; O, 1313.9; and C, 1086.5.
<http://www.webelements.com/webelements/properties/>
- 20 J.M. Liu: *Opt. Lett.* **7**, 196 (1982)
- 21 P.L. Liu, R. Yen, N. Bloembergen, R.T. Hodgson: *Appl. Phys. Lett.* **34**, 864 (1979)
- 22 A. Cavalleri, K. Sokolowski-Tinten, J. Bialkowski, M. Schreiner, D. Von Der Linde: *J. Appl. Phys.* **85**, 3301 (1999)
- 23 T. Yoshida, S. Takeyama, Y. Yamada, K. Mutoh: *Appl. Phys. Lett.* **68**, 1772 (1996)
- 24 T. Makimura, T. Mizuta, K. Murakami: *Appl. Phys. Lett.* **76**, 1401 (2000)
- 25 T. Makimura, T. Mizuta, K. Murakami: *Appl. Phys. A* **69**, S213 (1999)
- 26 Z. Paszti, G. Peto, Z.E. Horvath, A. Karacs: *Appl. Surf. Sci.* **168**, 114 (2000)

- 27 S. Facsko, T. Bobek, H. Kurz, T. Dekorsy, S. Kyrata, R. Cremer: Appl. Phys. Lett. **80**, 130 (2002)
- 28 H.W.K. Tom, G.D. Aumiller, C.H. Brito-Cruz: Phys. Rev. Lett. **60**, 1438 (1988)
- 29 S.V. Govorkov, I.L. Shumay, W. Rudolph, T. Schröder: Opt. Lett. **16**, 1013 (1991)
- 30 L.Y. Sadler, M. Shamsuzzoha: J. Mater. Res. **12**, 147 (1997)

CHAPTER 5. FEMTOSECOND PULSED LASER MICROMACHINING OF SINGLE CRYSTALLINE 3C-SiC AND SI STRUCTURES

A portion of this chapter is excerpted from the paper published in the *Journal of Micromechanics and Microengineering* (2003)

Yuanyuan Dong, Christian Zorman, and Pal Molian

ABSTRACT

A femtosecond pulsed Ti:Sapphire laser with a pulse width of 120 fs, a wavelength of 800 nm, and a repetition rate of 1 kHz was employed for direct write patterning of single crystalline 3C-SiC thin films deposited on Si substrates and bulk 6H-SiC. For surface micromachining of 3C-SiC thin films on Si substrate, low pulse energies were preferred to ensure well-defined and debris-free patterns in 3C-SiC thin films based on the defect-activation ablation mechanism. Micromechanical structures such as micromotor, gas turbine rotor and lateral resonators were patterned into 3C-SiC films. For bulk micromachining of 6H-SiC, the request for low pulse energy was not as exacting as one for 3C-SiC thin films processing. It demonstrates that femtosecond laser direct-writing is a promising technology to produce high-quality diaphragms of 6H-SiC pressure sensor with controllable diameter and thickness.

INTRODUCTION

SiC has recently attracted significant interest in the field of micro-electro-mechanical systems (MEMS) due to its exceptional physical properties, such as high stiffness, mechanical strength, extreme chemical inertness and wide band gap. Various SiC-based

MEMS devices such as temperature sensors, gas sensors, pressure sensors, micromotors, and resonators have been fabricated for use in harsh temperature, erosion, corrosion, shock and vibration environments [1-5]. Reliable patterning processes are critical for the successful fabrication of SiC-based MEMS devices. SiC is a difficult material to etch using conventional techniques due to its high hardness and chemical inertness. Nevertheless, reactive ion etching (RIE) and photo-electro-chemical (PEC) etching have been developed for SiC surface and bulk micromachining [6,7]. Of the two, RIE is more commonly used, however, it tends to suffer from such issues as low etch rate, poor selectivity to polysilicon and silicon dioxide sacrificial layers, and micromasking of the etch field [7]. Although a micromolding technique has been developed as an alternative to RIE for SiC surface micromachining [7], the added processing steps involved makes micromolding more complicated than direct patterning processes.

Laser direct writing is a novel patterning method with potential in SiC micromachining. Compared to other patterning technologies, laser micromachining has the advantages of fast removal rates, being independent of etch masks (direct writing), and an insensitivity to crystallographic orientation. Moreover, laser direct writing can be used to fabricate three-dimensional micromechanical devices since samples can be mounted onto a programmable positioning stage. In contrast, conventional lithographic techniques can only be used to fabricate unidirectional extensions of two-dimensional patterns. Laser direct writing enables control over the dimensions of curved features, thus allowing for the generation of complex mechanical microstructures. Ultrafast laser micromachining produces better resolution and cleaner features than conventional laser micromachining due to the reduction in heat dissipation and recast layers [8,9]. Because the ultrafast laser pulses remove

material by driving nonlinear multiphoton absorption with high peak fluences, strong absorption at the workpiece is not critical. Therefore, ultrafast lasers can also be used to process a wide range of materials and are particularly well suited for chemically inert materials like SiC.

SURFACE MICROMACHINING OF 3C-SiC THIN FILMS

In this work, an ultrafast Ti:Sapphire oscillator-amplifier system (Spectra-Physics, Inc., Model Hurricane X), based on a chirped-pulse-amplification (CPA) technique [9] was used to pattern single crystalline 3C-SiC thin films deposited on Si substrates. The nominally 1- μm thick single crystalline 3C-SiC films were heteroepitaxially grown on Si (100) in an atmospheric pressure chemical vapor deposition (APCVD) reactor using a two-step growth process detailed elsewhere [10]. A set of neutral density (ND) filters was utilized to obtain lower pulse energies. The patterning of SiC films into various component structures such as micromotors, gas turbine rotors and lateral resonators was performed in the low pulse energy regime to demonstrate the potential for this type of processing technique.

It is clear from the previous research results that laser micromachining using low pulse energies enables the patterning of cleaner and smaller 3C-SiC features than patterning using high pulse energies. This is, in large measure, due to the absence of a heat-affected zone (HAZ) recast and debris surrounding the patterned features. To explore the utility of this technique in device fabrication processes, various patterns were laser micromachined into 1 μm thick, 3C-SiC samples. Prior to patterning, the 3C-SiC samples were sequentially rinsed in acetone and methanol and then mounted on a motorized x-y stage (Coherent LabMotion Series). This stage has a repeatability of 1 μm and a resolution of 1 μm . The

stage was programmed to move the substrate in a manner that produced the desired shapes. A quarter wave plate was used to change linearly polarized light into circularly polarized light. High pressure helium was used to eject vaporized material, to produce clean cuts and to protect the lens. Both high and low pulse energies were used for a comparison.

Figure 5.1 shows SEM images of SiC micromotor rotors processed at three pulse energies. At a pulse energy of 20 μJ , a complete rotor with well-defined features (Fig. 5.1a) could not be processed. Significant heat conduction and thermal damage due to high pulse energy deteriorated the SiC thin film. Additionally, the Si field areas exhibited a rough surface morphology, characterized by jagged protrusions resulting from debris and recast. At a moderate pulse energy (2 μJ), much of the SiC rotor exhibited a reasonably well-defined profile (Fig. 5.1b). However, a portion of the SiC structural layer was completely ablated. The laser-exposed Si substrate contained micron-sized surface features and tiny holes when repeatedly irradiated with laser pulses. Similar laser-induced surface features on Si have been reported elsewhere [11, 12]. At a low pulse energy (0.5 μJ), an intact and well-defined SiC rotor was patterned (Fig. 5.1c). It should be noted that the size of the rotor in Fig. 5.1c is only one-half of those patterned at higher energies, inferring that low-energy processing significantly reduces contamination and debris that adversely affect resolution. Figure 5.1d is an enlarged view of the sidewall of the rotor showing the presence of nano-particles on the surface. This phenomenon is consistent with the laser-induced polycrystallization of SiC described in chapter 4.

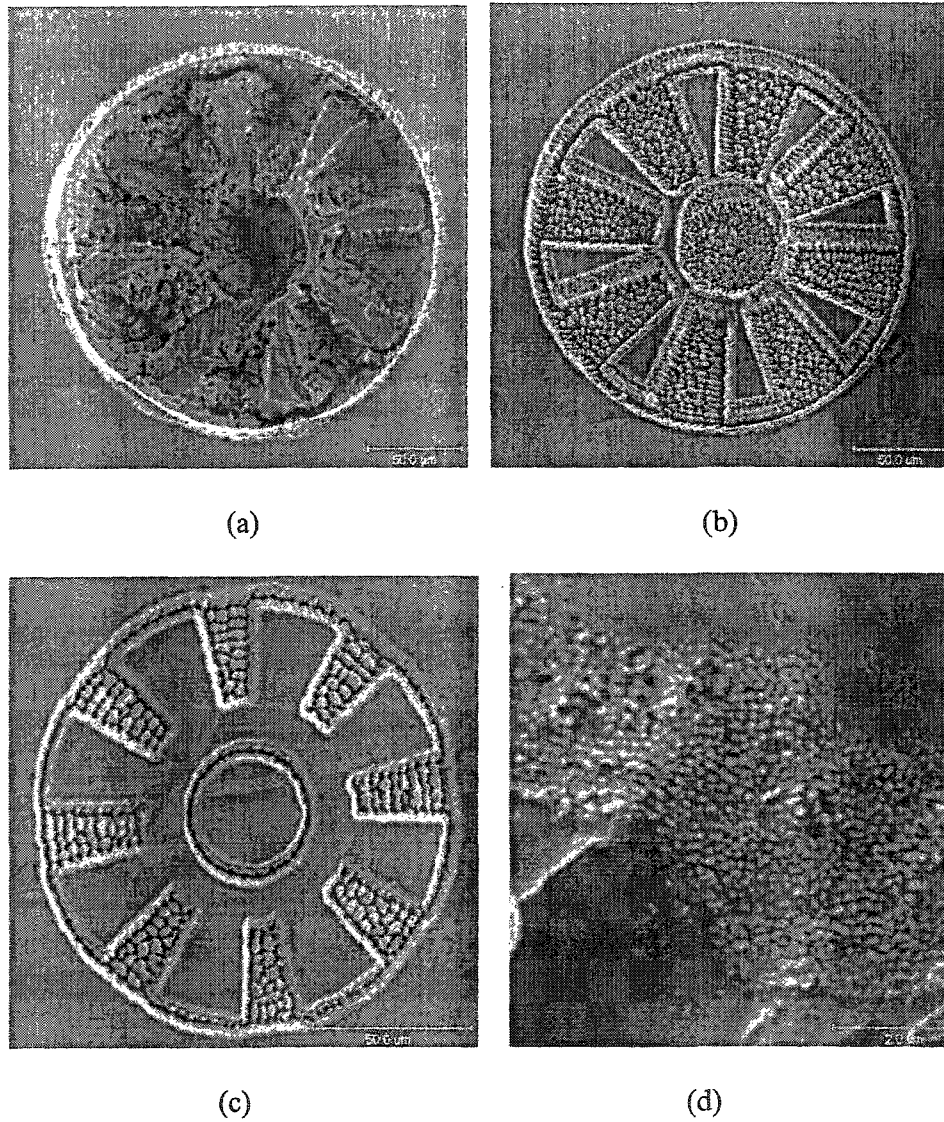
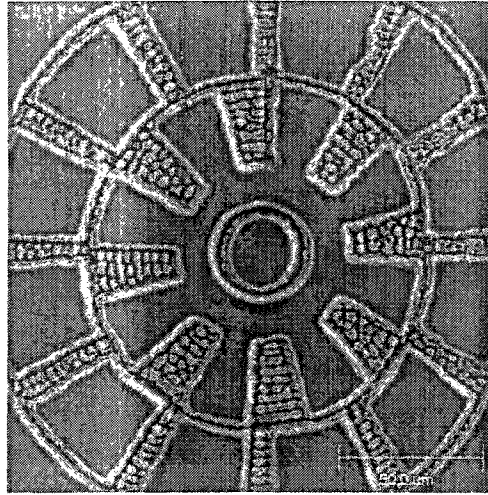


Figure 5.1. SEM images of rotors of micromotors processed at different energies in helium: a. at 20 μJ ; b. at 2 μJ ; c. at 0.5 μJ ; d. close-up view of the machined sidewall; e. micromotor at 0.5 μJ .



(e)

Figure 5.1 continued

Figure 5.1e shows an SEM image of a micromotor consisting of stator and rotor. In order to fabricate a rotary micromotor, a KOH etch was used to suspend the rotor part. However, the central shaft of micromotor must be prevented from etching away while the rotor was suspended, which is more likely to happen because the area of shaft is much smaller than each arm of the rotor. Therefore, a bearing should be created by local deposition of about 1- μm thick SiC thin film [13]. Consequently, the KOH etch for Si substrate needs two steps. The first etch must be carefully controlled so as not to etch through the whole shaft, which should strongly anchor to the Si substrate at the center during the time of etching. After the first etch, SiC bearing will be deposited in about 7- μm wide gap between and on the top of the shaft and rotor. The second etch will fully release the rotor but not the shaft and the stator by reasonably controlling the etch time. Because the deposition of bearing is a quite complex process, the fabrication of a rotary micromotor is a long way from reaching the maturity.

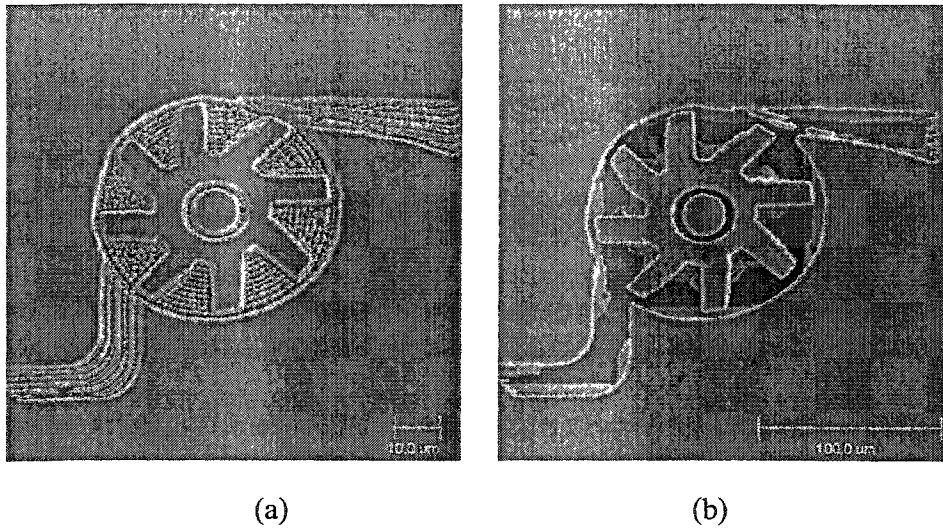


Figure 5.2. SEM images of microturbine rotors processed at 0.5 μJ : a. before etch; b. after-KOH etch.

Figure 5.2 shows the SEM image of a 100- μm wide micro-turbine rotor with a gas channel, fabricated at 0.5 μJ pulse energy through the defect activation ablation mechanism. The processing of the whole feature needed just one step in laser micromachining. The channel is intended to direct the gas flow through the turbine and minimize it around the turbine. The SiC rotor meets the requirement of material hardness for prolonging its lifespan. A flow sensor can be made if this rotor is integrated with an optical fiber for many applications. High aspect ratio is another requirement for micro-turbine rotor to enhance the sensitivity of flow sensor. Usually X-ray lithography and LIGA (galvanoformung) technologies are used to make this device with high accuracy and high aspect ratio. The turbine rotor, shown in Figure 5.2a, did not have the high aspect ratio because SiC thin film on Si is only about 1 μm . However, high aspect ratios can be achievable in laser micromachining, either by adjusting down the laser focal point or employing the

programmable movement of z-direction of the stage. Figure 5.2b is the SEM image of after-etch turbine rotor. It is noted that Si in the area exposed to laser irradiation has almost been etched through and the smooth bottom of Si substrate is revealed. But Si under SiC rotor was left unetched due to lack of time.

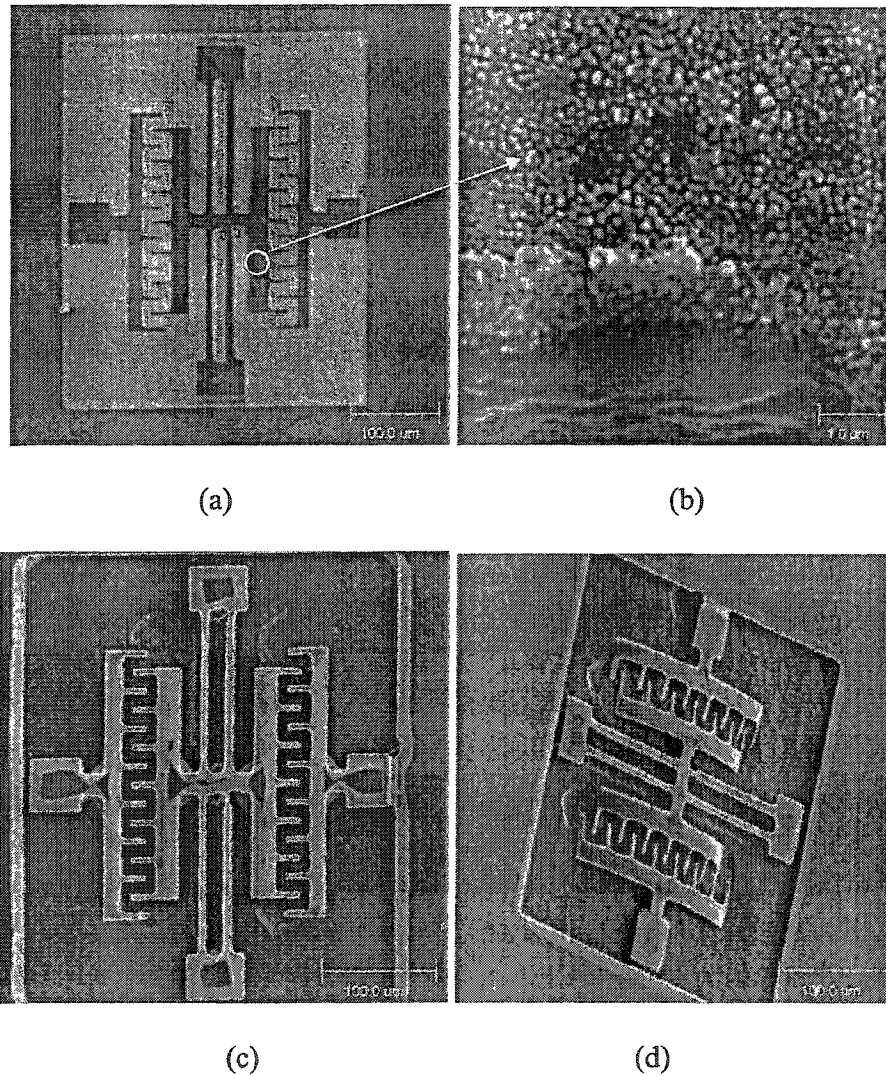


Figure 5.3. SEM images of lateral resonator processed at 1 μJ : a. before etch; b. close-up view of the sidewall of one side of right shuttle; c. plan view of after-KOH etch; d. tilt view of after-KOH etch.

Figure 5.3 shows an one-step laser micromachined lateral resonant structure patterned using a pulse energy of 1 μJ before and after sacrificial undercutting of the SiC structures in KOH. The SEM image prior to release (Fig. 5.3a) shows a distinct contrast between the unirradiated SiC regions and the laser-machined field areas. Figure 5.3b shows the magnified view of the sidewall of the resonator. Nano-particles exist on all edges exposed to the laser beam. This indicates that the defect-activation ablation mechanism described previously occurs when exposed to the tail of Gaussian beam with a lower pulse energy. A plan view image of the resonator after KOH etching (Fig. 5.3c) shows that the laser-damaged regions of Si in the field areas are easily removed and the Si surface is remarkably smoother than before etching. In the tilt view (Fig. 5.3d), stiction - the sticking of structures to the substrate after releasing - is observed, and the shuttle part is suspended after etching. Stiction is a very common problem in MEMS fabrication, which can be solved by supercritical drying [13].

BULK MICROMACHINING OF 6H-SiC DIAPHRAGM

SiC-based MEMS pressure sensors are suitable to withstand harsh environments, for example, being able to operate stably at 500°C or above. A 6H-SiC-based pressure sensor developed by Kulite Semiconductor Products, Leonia, NJ uses n-type 6H-SiC piezoresistors on a p-type 6H-SiC diaphragm. The diaphragm is fabricated using a photoelectrochemical (PEC) etching process. The attractiveness of an “all-SiC” high-temperature pressure sensor is affected by poor PEC etching directionality, making lateral dimensional control (e.g., diaphragm size) difficult. And small wafer sizes and complex fabrication processes are limiting factors. As an alternative, 3C-SiC-based pressure sensors developed by Case

Western Reserve University utilize 3C-SiC films grown on silicon substrates and Si bulk micromachining to produce 3C-SiC diaphragm and use NiCr thin films or p-type polysilicon for the piezoresistive sensing elements. This kind of hybrid pressure sensor NiCr/3C-SiC or poly-Si/3C-SiC underwent material thermal mismatch effects, which may degrade long-term device performance and lifetime in the presence of thermal cycling. In addition, currently used Si wet etching restricts Si (100) substrates to be square or rectangular membranes (diaphragms). To the point of view of design, it is theoretically proven that circular membranes show more favorable in stress and deflection than rectangular and square membranes. Hence, laser micromachining is a flexible and feasible technique to circumvent the above unfavorable issues. Femtosecond laser micromachining technique is quite attractive not only to produce an “all-SiC” pressure sensor by bulk micromachining of SiC but also to process circular SiC membranes due to its insensitivity to crystallographic orientation. Preliminary experimental results demonstrate the feasibility of forming SiC diaphragms with controlled diameter and thickness and location.

Preliminary Analysis of SiC Diaphragm Formation

A test sample consisting of a 35mm, 6H-SiC n-type wafer (D0177-05, Sterling) was cleaved in half and used for an initial set of laser trepanning experiments. The test piece was placed on a programmable X-Y stage, which was programmed to move the sample under the laser beam in a series of concentric circles. The number of concentric circles and each incremental radius determine the diameter of test diaphragm (also called hole diameter). The results of the stylus profilometer scans for the holes that did not go all the way through the wafer show that a). Control of diaphragm diameter is excellent. b). The etch rate changes

ultimately ablation results in debris-free patterning without thermal damage to the films. This process was used to pattern SiC films into the shapes of some commonly recognized MEMS structures. This study shows that femtosecond pulsed laser ablation has potential for SiC micromachining, but much work remains before it can be used to produce structures and devices with comparable fidelity to SiC RIE.

ACKNOWLEDGEMENTS

The authors would like to acknowledge the National Science Foundation (NSF) for supporting this research work under the grant DMI-9978633. Thanks are also due to Dr. Warren E Straszheim for providing SEM characterization.

REFERENCES

1. T. Nagai T and M. Itoh M 1990 SiC thin-film thermistors IEEE Trans. Ind. Applicat. **26**, 1139-1143.
2. Spetz AL Tobias P Baranzahi A Martensson P and Lundstrom I 1999 Current status of silicon carbide based high-temperature gas sensors, IEEE Trans. Electron. Dev., **46** 561-566.
3. R. Zeirmann R J. von Berg J W. Reichert W E. Obermeier E M. Eickhoff M and G. Kortz G 1997 A high temperature pressure sensor with β -SiC piezoresistors on SOI substrates in Tech. Dig. 1997 Int. Conf. Solid State Sensors and Actuators, K. Wise and S. Senturia, Eds., Chicago IL, June 16-19, pp.1411-1414.
4. Yaseen AA Wu CH Zorman CA and Mehregany M 2000 Fabrication and testing of surface micromachined polycrystalline SiC micromotors IEEE Elect. Dev. Lett **21** 164-

- 166.
5. Mehregany M and Zorman CA 1999 SiC MEMS: opportunities and challenges for applications in harsh environments *Thin Solid Films* **355-356** 518-524.
 6. Harris GL *Properties of Silicon Carbide*, Published by: INSPEC, the Institution of Electrical Engineering, London, United Kingdom, 1995.
 7. Mehregany M Zorman CA. Rajan N and Wu CH 1998 Silicon Carbide MEMS for Harsh Environments *Proc. IEEE* **86** 1594 –1610.
 8. Pronko PP Dutta SK Squier J Rudd JV Du Dand Mouron G 1995 Machining of sub-micron holes using a femtosecond laser at 800 nm *Optics Communications* **114** 106-110.
 9. Liu X Du D and Mourou G 1997 Laser ablation and Micromachining with Ultrashort Laser Pulses *IEEE J. Quantum Electronics* **33**, 1706-1716.
 10. Zorman CA Fleischman AJ Dewa AS Mehregany M Jacob M and Pirouz P 1995 Epitaxial growth of 3C-SiC films on 4 in. diam (100) silicon wafers by atmospheric pressure chemical vapor deposition *J. Appl. Phys.*, **78** 5136-5138.
 11. Ameer-Beg S Perrie W Rathbone S Wright J Weaver W Champoux H 1998 Femtosecond laser microstructuring of materials *Appl. Surf. Sci.* **127-129** 875-880.
 12. Jhee YK Becker MF and Walser RM 1985 Charge emission and precursor accumulation in the multiple-pulse damage regime of silicon *J. Opt. Soc. Am. B.* **2** 1626-1633.
 13. Yasseen, A.A.; Chien-Hung Wu; Zorman, C.A.; Mehregany, M. "Fabrication and testing of surface micromachined silicon carbide micromotors", *Micro Electro Mechanical Systems, 1999. MEMS '99. Twelfth IEEE International Conference on*, pp. 644-649,1999

CHAPTER 6. FORMATION AND CHARACTERIZATION OF FEMTOSECOND PULSED LASER SYNTHESIZED NANOPARTICLES ON THIN FILMS OF 3C-SiC

This chapter is excerpted from a paper published in *Applied Physics Letters* (2004) and another paper submitted to *Physica Status Solidi A* (2004)

Yuanyuan Dong and Pal Molian

ABSTRACT

We report the formation of highly-oriented, uniform, and spherical nanoparticles of 3C-SiC as a result of Coulomb explosion during the interaction of near infrared ultrafast laser pulses with 3C-SiC thin films grown on Si substrate. Experiments were performed at laser fluences well below the single-shot, thermal modification threshold. The formation mechanism, size, shape, composition and structure of nanoparticles were analyzed by means of such ex-characterizations as SEM, AFM, XRD, AES and Raman spectroscopy.

INTRODUCTION

Nanoparticles have stimulated great interest in scientific and engineering communities because of their superior mechanical, electrical, optical and magnetic properties to their bulk counterparts [1-6]. Consequently their potential use would be extensive in the fields of quantum electronics, opto-electronics, information storage and processing, tribology and nano-electromechanical machines [7-14]. As an example, recent research has found the contribution of SiC nanocrystals embedded into SiO₂ to a high quantum efficiency of the radiative recombinations due to the quantum confinement effects of excitons in the

nanoparticles for the applications of blue-green light-emitting diodes and UV photodetectors [10]. The nanostructured SiC films with grain size around 20 nm exhibits hardness better than the top of the range for standard SiC and can be used for miniature moving parts (microgears) for micro-transmission owing to superior friction- and wear-resistance [15]. These promising characteristics further spur the research on synthesis and characterization of nanoparticles in recent years. As a result, a wide variety of physical, chemical, and mechanical methods, such as gas condensation techniques, Stranski-Krastanow growth mode, colloid chemistry, ion sputtering and pulsed laser deposition (PLD) [16-20], have been developed with their own advantages and disadvantages to generate nanoparticle-structured materials.

Recently, considerable research efforts have been directed to the Coulomb explosion for nanostructuring of insulator and semiconductor surfaces [21-30]. Theoretical studies [21-24] and molecular dynamics simulations [25-28] of Coulomb explosion have been well documented. Under either impingement of slow, highly charged ions [29] or ultrafast laser irradiation at low energy fluence [30], a charged-surface is created due to the emission of electrons. This surface, which cannot be neutralized in short time due to low hole mobility, stores sufficient repulsive electrostatic energy, which partly converts into kinetic energy during the relaxation process, thus causing Coulomb explosion. This explosion has been suggested to produce material damage, surface modification, and particle ejection, leaving a nanocrater on the surface. Coulomb explosion has been experimentally proven as the underlying mechanism of femtosecond laser “gentle” ablation by experimental observations of emission of ions during laser heating of semiconductors [31-33] and dielectrics [30]. For example, the emitted cluster cations (Si_nC_m^+) produced by laser ablation of SiC target were

detected by a time-of-flight quadrupole mass spectrometry [33]. Hence, researchers are exploring experimental techniques of Coulomb explosion for constructing nanostructured materials in nanoscience and nanotechnology.

We have described a femtosecond pulsed laser induced Coulomb explosion etching (CEE) technique in ambient air to directly and selectively generate nanoparticle layers with an area down to micron scale and thickness of about 350 nm on 3C-SiC single crystalline thin films that are beneficial for nanoelectronics applications [34]. The formation of nanoparticles, different from the indirect growth and nucleation process of conventional PLD, is initiated by femtosecond laser-induced CEE that leads to homogeneously distributed nanocraters in the SiC films and *in-situ* develops the nanoparticle textured surface. Unlike random grain orientation formed by PLD, identical grain orientation is one favorable trait due to the direct etching process. In addition, femtosecond (fs) laser, compared with the nanosecond (ns) lasers operating in the UV regime classically used for PLD, exhibits striking uniqueness including precise micromachining of fine feature with minimal thermal and mechanical damage, and micromachining of nearly all kinds of materials, even transparent materials due to high peak intensity [35-37]. Femtosecond laser-induced CEE is a potential micro- or nanoscale surface modification technique to synthesize highly oriented nanocrystalline films for applications such as micro-sensors, microelectro-mechanical systems (MEMS) and nanoelectro-mechanical systems (NEMS). The properties of nanostructured materials derived from nanoparticles can be tailored by altering the size, shape and surface modes of nanoparticles [38]. In this chapter, we not only provide an insight into the femtosecond laser interaction of 3C-SiC films based on Coulomb explosion but also analyze the structure and composition of nanoparticles as well as clarify the effects

of laser energy fluence on particle size by ex-situ characterization methods including scanning electron microscope (SEM), atomic force microscope (AFM), X-ray Diffraction (XRD), Auger Electron Spectrometry (AES), and Raman spectroscopes.

EXPERIMENTAL DETAILS

A regeneratively amplified Ti:sapphire laser (800 nm, 120 fs, 1 kHz repetition rate, 1 mJ maximum pulse energy) was used to irradiate the sample (3C-SiC on Si) under air ambient as well as argon gaseous environment. The samples consisted of nominal 2- μm -thick single crystalline 3C-SiC films that were heteroepitaxially grown on 500 μm thick Si (100) wafers in an atmospheric pressure chemical vapor deposition (APCVD) reactor using a two-step growth process described in detail elsewhere [39]. Prior to laser irradiation, the samples were polished and rinsed in acetone and methanol in sequence, and then immersed in a 10:1 HF aqueous solution to remove native oxide layer, and finally rinsed in deionized water.

The circularly polarized laser beam, steered through a 45° reflecting mirror and focused with a 50-mm focal length fused silica lens, was incident normal to the sample surface. The samples were mounted on a motorized x-y translation stage and then irradiated to generate the modified areas of 1 cm \times 1 cm using different laser fluences at a stage speed of 1 mm/s. The necessary and sufficient condition for the occurrence of a macroscopic Coulomb explosion is low-laser-fluence [30], which basically prevents the formation of dense plasma and ensuing thermal effects [35]. In our previous work on the femtosecond laser micromachining of SiC [36], a single-shot threshold of 0.52 J/cm² for non-thermal phase and $F_{\text{th}} = 0.97 \text{ J/cm}^2$ for thermal modification phase were noted. For this reason, the laser fluences in our experiments were set in the range of 0.45 J/cm² to 0.99 J/cm².

For the study about the effect of Gaussian profile energy on the size of nanoparticles, the modified line was generated by two-pass irradiation of 0.55 J/cm^2 laser at a stage speed of 1 mm/s . All the experiments were performed in ambient air with Ar gas flow on the surface in order to keep the surface clean during the process.

RESULTS AND DISCUSSION

SEM Characterization

The nanoparticles were examined in the scanning electron microscope (SEM) (plan and side views). Figure 6.1a to d show SEM images of fs-laser induced 3C-SiC nanoparticles at four different laser energy fluences. As shown in Figure 6.1a, these nanoparticles are approximately spherical, closely packed, and fairly uniform in size (100-200 nm). However, with a gradual increase in fluence, the array and shape of nanoparticles appear chaotic and irregular (Fig. 6.1c). Once the fluence exceeded 0.99 J/cm^2 , the modified SiC films underwent immediately melting phase accompanied by the disappearance of nanoparticle as seen in Figure 6.1d. In chapter 4, a thermal modification threshold F_{th} of 0.97 J/cm^2 was obtained, which defines the minimal energy fluence for launching thermal damage on 3C-SiC thin films by single laser shot. Our results have thus far proven that whether nanoparticles on SiC thin films are formed or not hinges upon a certain range of low energy fluences. Judged from the array and shape of nanoparticles irradiated at different fluences, three distinct regimes are classified to correspond to the altered appearance of nanoparticles: formation of nanoparticles (below $0.6F_{th}$), disordering ($0.6-0.8F_{th}$), melting (above $0.8F_{th}$). The conversion of 3C-SiC layer into nanoparticulates took place to a depth of about 350 nm (Fig. 6.1e). Such

observations strongly suggest that low energy irradiation is the key to synthesize nanoparticles.

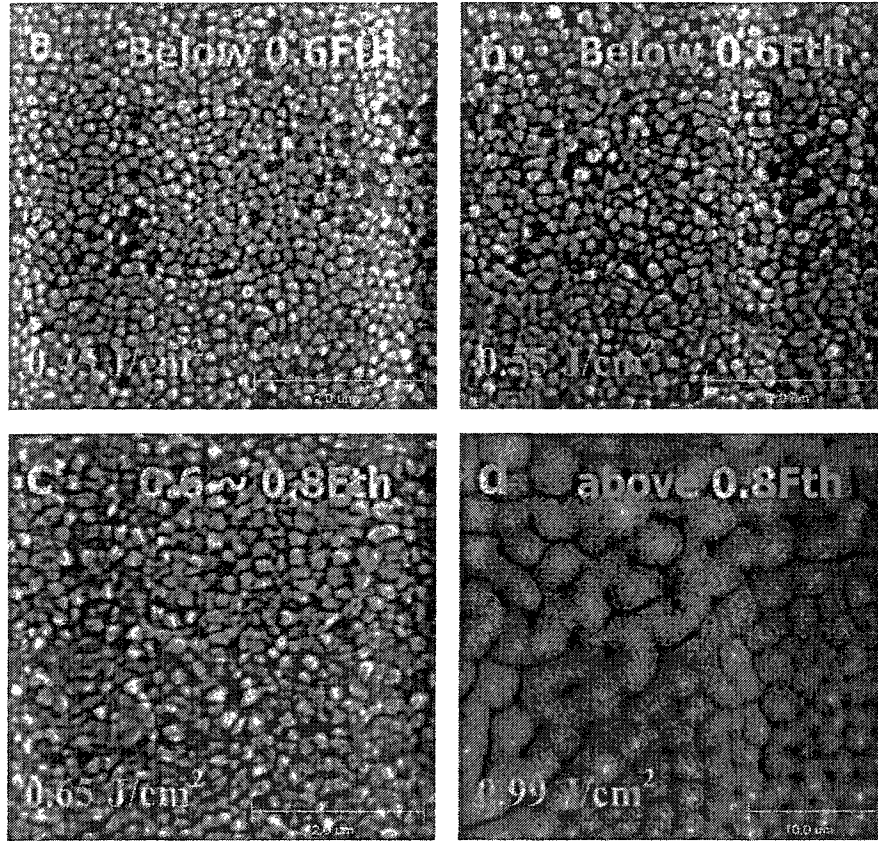
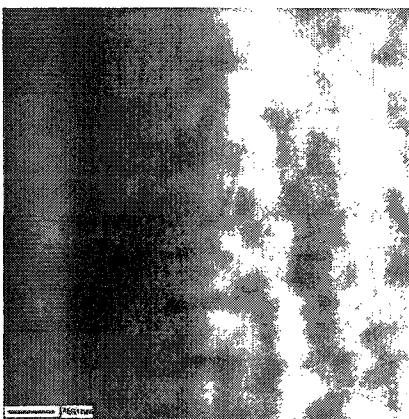


Figure 6.1. Scanning electron micrographs of 800-nm, 120-fs laser-irradiated 3C-SiC areas, Plan view for the sample treated at four different laser fluences: (a) 0.45 J/cm^2 ; (b) 0.55 J/cm^2 ; (c) 0.65 J/cm^2 ; and (d) 0.99 J/cm^2 ; (e) Side view (cross section image) for the sample treated at 0.45 J/cm^2 .



(e)

Figure 6.1 continued

Contrary to expectations, there is no correlation between the size of nanoparticles and energy fluence. One convenient way to validate the absence of correlation is to examine how the particle size varied with beam energy distribution (Gaussian type). Figure 6.2a shows one line irradiated at 0.55 J/cm^2 . Due to spatial Gaussian distribution of laser beam spot, the edge of the line (position b, $60 \mu\text{m}$ away from the center position d) was exposed to the tail of Gaussian beam with the lowest fluence, and the center of line (position d) was exposed to the center of Gaussian beam with the peak fluence, position c ($30 \mu\text{m}$ away from the center) was subjected to an intermediate fluence. Figures 6.2 b, c and d show the close-up views at three positions b, c and d. At b position, nanoparticles were incompletely formed ascribed to relatively lower fluence irradiation. However, nanoparticles were fully formed with similar size at position c and d, though they were subjected to different fluences. Thus, the size of nanoparticles is not fluence dependent within the range that allows nanoparticle formation.

Perhaps the most crucial parameter would be wavelength of light. The high harmonic generation of femtosecond laser has potential to scale down the size of nanoparticles [40].

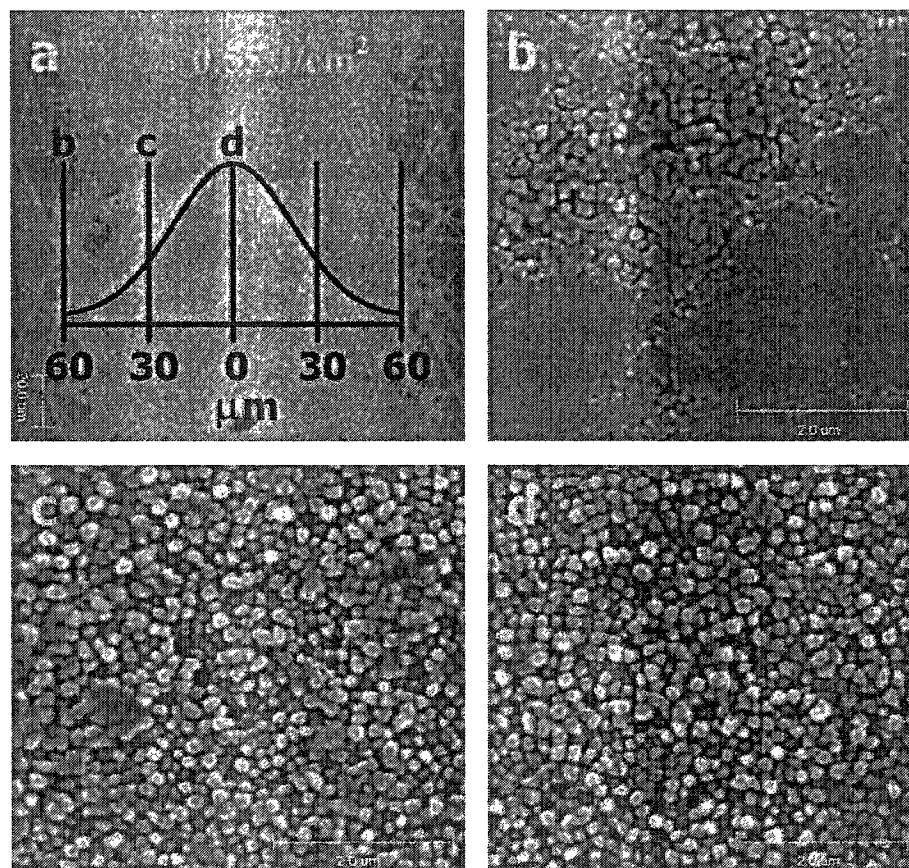
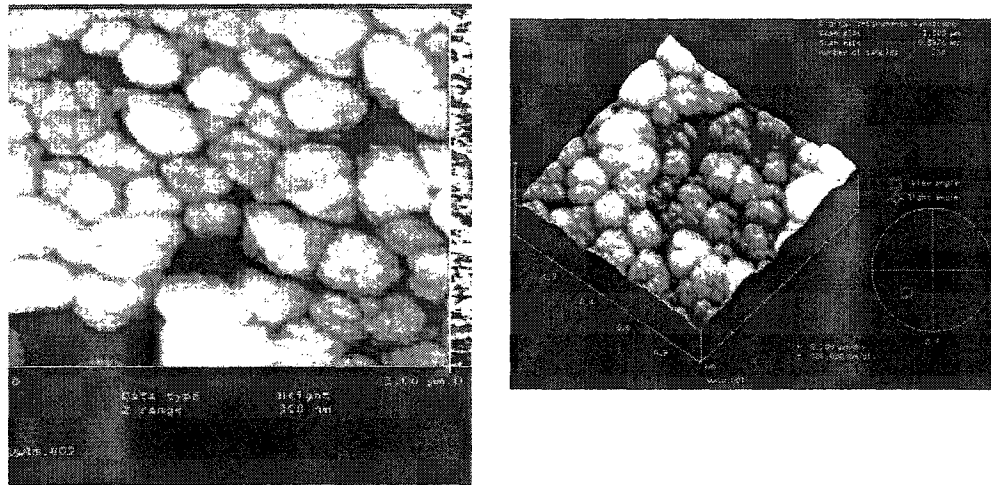


Figure 6.2. Effect of Gaussian profile energy on the size of nanoparticles. Scanning electron micrographs of 800-nm, 120-fs laser-modified 3C-SiC line of sample irradiated at $0.55 \text{ J}/\text{cm}^2$ for two passes.

AFM Characterization

Figure 6.3 shows typical AFM micrographs of nanoparticles in SiC film irradiated below $0.6F_{\text{th}}$. In figure 6.3a, the picture shows the morphological features of nanoparticles in detail. It is observed that the nanoparticles are surrounded by the nanocraters. In addition, the

nanocraters are also seen on each nanoparticle and split it into many smaller nanoparticles with size of 30~70 nm. Few cavities with a depth of about 145 nm provide the evidence for the ejection of particles. These experimental observations suggest that Coulomb explosion occurs during the bombardment of fs-laser pulses (low energy fluence) on 3C-SiC thin films. The absorption of fs-laser pulse by the defect states (the sources of defects in SiC films are from either stacking faults due to 3C-SiC growth on Si [41] or color-centers and mechanical defects generated by first pulse [42]) on the surface of SiC films prompts the excitation of electrons, creating electron-hole pairs. A repulsive electrostatic field is then induced by the accumulation of high concentration positive charges (holes) since electron-hole pairs cannot recombine instantaneously due to low hole mobility. In this case, Coulomb explosion is initiated, leading to ion and particle ejection and eventually forming nanoscale craters on the surface as shown Figure 6.2b. It is these craters distributed over the entire irradiated surface that makes this nanoparticle-like structure in SiC films. These nanoparticles are thus “left over” after particle ejection due to Coulomb explosion. In addition, the nanoparticles were uncontaminated without any thermal damage (Figures 6.1a to c). Here the “gentle” ablation was initiated by the two-photon absorption and dominated by Coulomb explosion. Once the fluence reached thermal modification threshold of 0.97 J/cm^2 , strong ablation via multiphoton absorption has occurred (Figure 6.1d), resulting in phase explosion and collateral thermal damage.



(a)

(b)

Figure 6.3. The typical atomic force micrographs of nanoparticles in SiC film irradiated below $0.6F_{th}$.

X - Ray Diffraction

The crystalline structure and orientation of nanoparticles were identified by x-ray diffraction (XRD) technique. Figure 6.4 shows XRD pattern of both non-irradiated and laser irradiated areas of 3C-SiC films. The (111), (200) and (400) reflection peaks are identified in the initial 3C-SiC thin films (scan (a)). Scans (b), (c) and (d) are obtained from three different samples that were laser irradiated at 0.45 J/cm^2 , 0.55 J/cm^2 and 0.65 J/cm^2 , respectively. A comparison among these scans show that the ratio of intensity of (111) to (200) peaks at fluence below $0.6F_{th}$ underwent a sharp reduction after irradiation at 0.45 J/cm^2 and then further down to the smallest value at 0.55 J/cm^2 . However, this decreasing trend did not continue with increasing fluence to above $0.6F_{th}$ as seen in scan (d) at 0.65 J/cm^2 . In addition, the FWHM of (200) peak becomes narrower at 0.45 J/cm^2 and the narrowest at 0.55 J/cm^2 . In all cases, SiC nanocrystals exhibited the initial cubic (zinc-blende) structure. A

strong preferred orientation along the $\langle 100 \rangle$ direction was observed, indicating the more stable structure, together with the narrowing of the FWHM of (200) peak. Nevertheless, this desirable crystal structure abruptly deteriorated at the higher energy fluence of 0.65 J/cm^2 and transformed into polycrystalline structure as characterized by the stronger (111) peak over (200) peak and the broader FWHM of (200) peak. This broadening effect is attributed to lattice disorder induced by fs-laser irradiation as observed in other semiconductor materials Si, GaAs, and InSb [43]. X-ray diffraction further confirms the presence of three such distinct regimes in terms of lattice structural modifications: lattice structural rearrangement (below $0.6F_{th}$) due to lattice heating by femtosecond laser irradiation accounting for a preferred orientation along the $\langle 100 \rangle$ direction, lattice disordering ($0.6\text{-}0.8F_{th}$) resulting from the destabilization of the atomic bonds due to intense emission of electrons, and melting ($0.8F_{th}$) *via* multiphoton absorption.

The modification of crystal structure at fluences below $0.6F_{th}$ is attributed to lattice arrangement resulted from increased lattice vibration due to lattice heating [44-46] accompanying Coulomb explosion. The ultrafast laser pulse induces a repulsive electrostatic field, consisting of uncompensated positive charges due to the emission of electrons on the surface. The neutralization of positive charges directly ejects charges and indirectly ejects neutrals due to collision. Alternatively, electron supply from the bulk or hole diffusion can take place in which case the carrier energy is transferred to the lattice through the emission of longitudinal-optical (LO) phonons [45]. These processes result in lattice heating and subsequent increased lattice vibration and final lattice reconfiguration. At fluences above $0.6F_{th}$, destabilizing the atomic bonds due to intense emission of electrons [44] directly induces the lattice disorder.

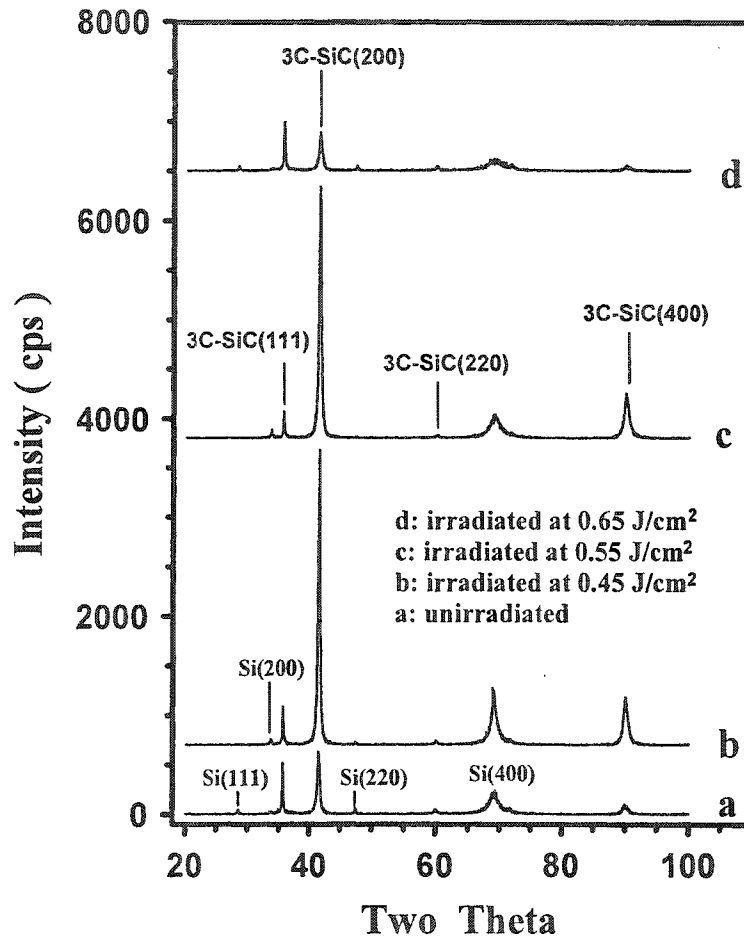


Figure 6.4. X-ray diffraction spectra of 3C-SiC films unexposed and exposed to the ultrafast laser.

Auger Electron Spectrometry

The compositions of virgin and laser-irradiated SiC films were examined by AES. Spectra a, b and c shown in Figure 6.5 represent laser as-irradiated, post Ar-ion etched and virgin SiC films, respectively. The virgin and post Ar-ion etched films were comparable in binding energy and intensity. For the laser-irradiated film, an oxygen contamination was

present, but it was rapidly reduced to the same trace amount as that in virgin film after 35 seconds' Ar ion etching. This suggests that oxygen did not participate in nanostructuring and remained as only absorbed oxygen in the SiC surface layer during the laser irradiation due to Coulomb explosion-induced non-neutral state of SiC.

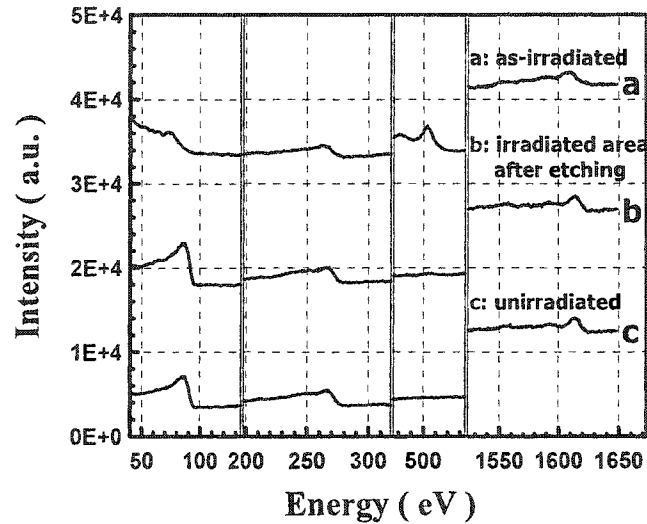


Figure 6.5. The AES spectra of before- and after- irradiated films at 0.45 J/cm^2 .

Raman Spectroscopy

High quality heteroepitaxial films are required for the fabrication of electronic devices. In the case of 3C-SiC on Si, internal stress, arising from the differences in lattice constants (20%) and thermal-expansion coefficients (8%) between 3C-SiC layers and Si substrates, is an essential issue that deteriorates the electrical properties. The stress tends to change the atomic distances or the bonding forces in crystal and consequently causes the shift of phonon Raman bands. Hence, Raman scattering measurements were used for the evaluation of stress states of 3C-SiC films. Figure 6.6 shows the Raman spectra of samples before- and after-laser-irradiation. Transverse-optical (TO) and longitudinal-optical (LO)

phonon modes are observed at 792.4 and 963.7 cm^{-1} , respectively for the laser-irradiated samples. Both peaks have a significant red-shift (towards the low-wavenumber side) of 4 cm^{-1} and 9.3 cm^{-1} with respect to the TO (796.5 cm^{-1}) and LO (973 cm^{-1}) phonon modes of bulk 3C-SiC. The Raman peak at 510 cm^{-1} is associated with the Si substrate. The shift of Raman lines and the shoulder of Raman TO peak suggest the existence of the biaxial stresses, which are most likely from thermal waves [47]. Here, the strain in 3C-SiC films, estimated from Raman measurements, was 0.1% to 0.2% from the equations given below by [48]

$$\omega (\text{TO}) = 976.5 + 3734 (-\Delta a/a_0) \quad (1)$$

$$\omega (\text{LO}) = 973 + 4532 (-\Delta a/a_0) \quad (2)$$

where a_0 is the lattice constant.

Compared with the optical phonon modes of virgin 3C-SiC films (spectrum a), the Raman lines of 3C-SiC films (nanoparticulate films) irradiated below $0.6F_{\text{th}}$ (spectra b and c) remained same with respect to Raman line frequencies and linewidths. No evidence of extra stress induced by laser irradiation was found and no emergence of other Raman lines corresponding to other SiC polytypes was seen, indicative of absence of phase transformation under laser irradiation. Therefore, nanoparticle structuring by laser-induced CEE is a low-temperature technique that benefits device fabrication. It is worth mentioning that both carbon clusterization in graphitic phase (band around 1400-1500 cm^{-1}) and Si clusterization in amorphous phase (band around 480 cm^{-1}) were observed and that the amount of these clusters increases with energy fluence below $0.6F_{\text{th}}$. We believe that Coulomb explosion induced Si_nC_m^+ ejection gives rise to Si and C clusters remaining on the surface. Raman spectrum profile of 3C-SiC films irradiated at 0.6-0.8 F_{th} (spectrum d) displayed sharply reduced intensities and broadening of TO and LO phonon peaks, reflecting a heavily

disordered lattice structure in the irradiated films with nanoparticles. These are consistent with both degraded array and shape of nanoparticles in SEM micrograph (Fig.6.1c) and broadened FWHM (full width at half maximum) of 200 peak in X-ray diffraction (Fig.6.4). During the fluence regime of $0.6-0.8F_{th}$, intense emission of electrons destabilizes atomic bonds and further leads to lattice disorder in crystal while Coulomb explosion ejects ions and particles, forming nanosized craters and developing nanoparticles.

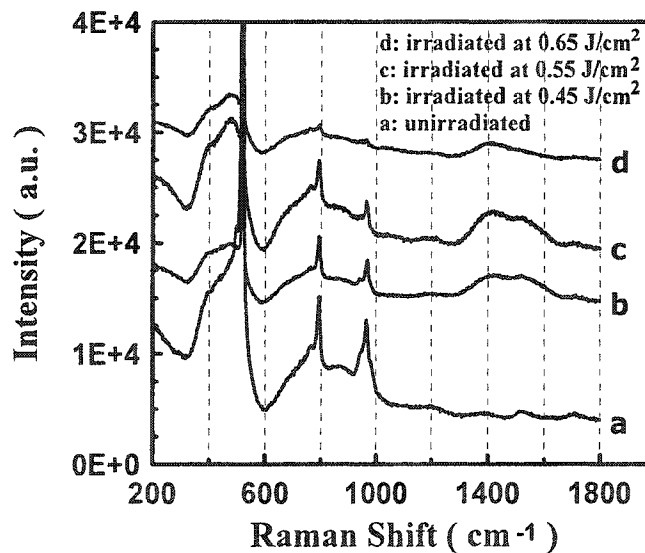


Figure 6.6. The Raman spectra taken from before- and after-laser-irradiated 3C-SiC films at different fluences.

CONCLUSIONS

An array of highly orientated nanoparticles with size of 30~70 nm on the surface of 3C-SiC single crystalline thin films was generated *in-situ* without inducing radiation defects in deeper layers of SiC film by femtosecond laser irradiation. The mechanism of defect-activated Coulomb explosion is responsible for the formation of nanoparticles in 3C-SiC films. The evidence for Coulomb explosion is the presence of nanocraters around and over

nanoparticles. The characterization methods offered greater details of the dependence of nanostructuring on energy fluences below thermal modification threshold, $F_{th} = 0.97 \text{ J/cm}^2$. Below $0.6F_{th}$, both the *in-situ* formation of oriented nanoparticles resulting from Coulomb explosion and the lattice rearrangement due to lattice heating were observed. But the crystal structure of irradiated area still remained the initial cubic structure and nanoparticles were arrayed along a strong preferred lattice orientation $\langle 100 \rangle$. Micro-Raman scattering measurement revealed that nanoparticulate 3C-SiC layers did not undergo any stress change. In the range of $0.6\text{-}0.8F_{th}$, intense emission of electrons caused the heavily disordered lattice structure and degraded the shape of nanoparticles. Above $0.8F_{th}$, melting was observed due to multiphoton absorption. This is a very intriguing result and has potential applications in nanoelectronics and nanotribology.

ACKNOWLEDGEMENTS

The authors would like to acknowledge Dr. Warren E Straszheim for SEM and EDS analysis, James Anderegg for AES analysis, Joel Haringa for XRD measurement, Dr. Vladimir V Tsukruk and Hennady Shulha for AFM analysis, Chad Martindale for Micro-Raman spectroscopy measurement and valuable discussions with them. Thanks are also due to Dr. Chris Zorman (Case Western Reserve University, Cleveland) for providing us 3C-SiC thin film Samples. This research work was supported by the National Science Foundation (NSF) under the grant DMI-9978633.

REFERENCES

1. H.Gleiter, *Adv.Mater.* **1992**, 4,474.
2. G.A.Ozin, *Adv. Mater.* **1992**, 4, 416.
3. A.P. Alivisatos, *J.Phys.Chem.* **1996**, 100, 13226.
4. J.Narayan, Y.Chen, and R.M.Moon, *Phys. Rev. Lett.* **1981**, 46, 1491.
5. C.Suryanarayana, *Int. Mater. Rev.* **1995**, 40, 41.
6. R.W.Siegel, *Nanostruct. Mater.* **1994**, 4, 121.
7. M.Grundmann et al., *Phys. Rev. Lett.* **1995**, 74, 4043.
8. O.Böhme, A.L. Spetz, I.Lundström, and D.Schmeißer, *Adv. Mater.* **2001**, 13, 597.
9. Y.Zhang, T. Ichihashi, E. Landree, F. Nihey, and S. Iijima, *Science*, **1999**, 285, 1719.
10. Xueqin Liu, Jing Zhang, Zhijun Yan, Shuyi Ma and Yinyue Wang, *Mater. Phys. Mech.* **2001**, 4, 85.
11. S.Tiwari, F.Rana, H.Hanafi, A.Hartstein, E.F.Crabbé, and K.chan, *Appl. Phys. Lett.* **1996**, 68, 1377.
12. S.Veprek, *J.Vac. Sci.Technol. A*, **1999**, 17, 2401.
13. B.Raguse, K.-H.Muller, and L.Wieczorek, *Adv. Mater.*, **2003**, 15, 922.
14. A.Schroth, R.Maeda, J.Akedo and M.Ichiki, *Jpn. J.Appl. Phys.*, **1998**, 37, 5342.
15. N. Tyimiak, J. Blum, A. Neuman, N. P. Rao, W. W. Gerberich, P. H. McMurry, J. V. R. Heberlein and S. L. Girshick, *Journal of Thermal Spray Technology*, **2001**,10, 173.
16. R.Uyeda. *Prog.Mater. Sci.* **1991**, 35, 1.
17. V.A.Shchukin and D.Bimberg, *Rev. Mod. Phys.* **1999**, 71, 1125.
18. P.Alivisatos, *Pure Appl. Chem.* **2000**, 72, 3.

19. S. Fascko, T. Dekorsy, C. Koerdt, C. Trappe, H. Kurz, A. Vogt, and H. Hartnagel, *Science*, **1999**, 285,1551.
20. J.Narayan, A.K.Sharma, A.Kvit, D.Kumar, and J.F.Muth, *Mater.Rev. Soc. Symp.* **2000**, 617, J2.4..1.
21. C.Watson and T.Tombrello, *Rad.Eff.* **1985**, 89, 263.
22. R.Stampfli and K.H.Bennemann, *Appl. Phys. A.* **1996**, 60, 191.
23. T.Schenkel, A. V. Hamza, A. V. Barnes, D. H. Schneider, J.C.Banks and B.L.Doyle, *Phys.Rev.Lett.* **1998**, 81,2590.
24. I.S.Bitenskii, M.N.Murakhmetov, and E.S.Parilis, *Sov. Phys. Tech. Phys.* **1979**, 24, 618.
25. R.E.Walkup and Ph.Avouris, *Phys.Rev.Lett.* **1986**, 56, 524.
26. E.Wu, R.J.Friauf, and T.P.Armstrong, *Sur. Sci.* **1991**, 249, 350.
27. H.P.Cheng, J.D.Gillaspy, *Phys. Rev. B* **1997**, 55, 2628.
28. A.A.Valuev, M.Terasawa, T.Sekioka, Z.A.Insepov, I.Yamada, *Computational Nanoscience and Nanotechnology*, **2002**, 455.
29. D.H.Schneider, M.A.Briere, J.McDonald, and J.Biersack, *Radiat. Eff. Def. Solids*, **1993**, 127, 113.
30. R.Stoian, D.Ashkenasi, A.Rosenfeld, and E.E.B.Campbell, *Phys. Rev. B*, **2000**, 62,13167.
31. J.M. Liu, R.Yen, H.Kurz, and N.Bloembergen, *Appl. Phys. Lett.* **1981**, 39, 755.
32. J.Solis, F.Vega, and C.N.Afonso; E.Georgiou, D.Charalambidis, and C.Fotakis, *J. Appl. Phys.*, **1993**, 74, 4271.
33. S.H.Nam, C.H.Bae, and S.M.Park, *The 7th International Conference on Laser Ablation* Oct. 5-10, **2003**, Hersonissos, Crete, Greece.

http://www.iesl.forth.gr/cola03/presentations/show.asp?Sp_type=Oral

34. Y.Dong and P.Molian, *Appl. Phys. Lett.* **2004**, 84, 10.
35. Y.Dong, C.Zorman, and P.Molian, *J. Micromech. and Microeng.*, **2003**,13, 680.
36. Y.Dong and P.Molian, *Appl. Phys. A*, **2003**, 77, 839.
37. X.Liu, D.Du and G. Mourou, *IEEE J. Quant. Electron.*, **1997**, 33, 1706.
38. A.Henglein, B.G.Ershov, M.Malow, *J.Phys.Chem.* **1995**, 99, 14129.
39. C.A.Zorman, A.J.Fleischman, A. S. Dewa, and M. Mehregany, *J. Appl. Phys.* **1995**, 78, 5136.
40. N.Yasumaru, K.Miyazaki and J.Kiuchi, *Appl. Phys.A*, **2003**,76, 983.
41. M.Mehregany, C.A.Zorman, N. Rajan, and C.H.Wu, *Proceedings of the IEEE*, **1998**, 86, 1594.
42. M.Henyk, R.Mitzner, D.Wolfframm, and J.Reif, *Appl.Surf.Sci* , **2000**, 154-155, 249.
43. A.H.Chin, R.W.Schoenlein, T.E.Glover, P.Balling, W.P.Leemans, and C.V.Shank, *Phys. Rev. Lett*, **1999**, 83, 336.
44. Li Huang, J. Paul Callan, Elin. Glezer, and Eric Mazur, *Phys. Rev. Lett.* **1998**, 80, 185.
45. J.A.Kash, J. C. Tsang, and J. M. Hvam, *Phys. Rev. Lett.* **1985**, 54, 2151.
46. C.Rischel, A.Rousse, I.Uschmann, P.-A.Albouy, J.-P.Geindre, P.Audebert, J.-C.Gauthier, E.Förster, J.-L.Martin, and A.Antonetti, *Nature*, **1997**,390, 490.
47. H.Mukaida, H.Okumura, J.H.Lee, H.Daimon, E.Sakuma, S.Misawa, K.Endo and S.Yoshida, *J. Appl. Phys.* **1987**, 62, 254.
48. D.Olego, M.Cardona, and P.Vogel, *Phys.Rev.B*, **1982**, 25, 3878.

CHAPTER 7. FEMTOSECOND PULSED LASER ABLATION OF DIAMOND-LIKE CARBON FILMS ON SILICON

A paper submitted to (2004)

Y. Dong, H. Sakata, and P. Molian

ABSTRACT

Femtosecond pulsed laser ablation ($\tau = 120$ fs, $\lambda = 800$ nm, repetition rate = 1 kHz) of thin diamond-like carbon (DLC) films on silicon was conducted in air using a direct focusing technique for estimating ablation threshold and investigating the influence of ablation parameter on the morphological features of ablated regions. The single-pulse ablation threshold estimated by two different methods were $\phi_{th}(1) = 2.43$ J/cm² and $\phi_{th}(1) = 2.51$ J/cm². The morphological changes were evaluated by means of scanning electron microscopy. A comparison with picosecond pulsed laser ablation shows lower threshold and reduced collateral thermal damage.

Keywords: Diamond-like carbon; Laser

INTRODUCTION

DLC thin films are known to exhibit some properties characteristic of diamond such as hardness, high tensile yield strength, chemical inertness, low coefficient of friction, high thermal conductivity, and low electrical conductivity. However DLC films tend to be “amorphous” or nanocrystalline with no observable long-range order. These attractive properties endow DLC films for numerous scientific and industrial applications such as

optical coatings, wear and corrosion resistant coatings, hard coatings, and carbon-based MEMS and extended applications in the field emission display devices and electronics and MEMS when incorporating metal (Co, Ti, Al or Fe) into the DLC films [1]. However, its favorable properties of hardness and corrosion resistance make it difficult to perform mechanical processing and chemical etching. Femtosecond pulsed laser processing overcomes these barriers and shows potential to surmount the difficulties in the precise machining of hard coatings due to its very high peak laser intensity stemming from the extremely short pulse width. Femtosecond pulsed lasers also offer precisely defined machining regime with minimal collateral thermal damage [2]. In order to best process the DLC films and give insight into its interaction with femtosecond laser beam, the reasonable estimation of the ablation threshold must be made as this being very fundamental yet valuable. *Vouagner et al* [3] reported that laser (a pulsed picosecond Nd-YAG laser) ablation threshold of DLC films could be determined *in situ* by the means of measuring the photoelectrical signal and the charge of ionized species. Femtosecond pulsed laser ablation characteristics of DLC films on silicon are, however, not yet clarified. Here, we introduce a simple and more practical method to obtain the femtosecond laser ablation threshold.

EXPERIMENTAL

DLC films were deposited on polished surface-side of Si wafer by plasma-beam ion-injection deposition (PBIID) method. Film thickness was measured as 630 nm using a DEKTAK 3030ST surface profilometer. X-ray diffraction using a diffractometer (Philips, X'pert PRO) with a film XRD measuring attachment showed a broad halo pattern indicating amorphous nature of the DLC films.

A Ti:Sapphire oscillator-amplifier system (Spectra-Physics, Model Hurricane X), based on a chirped-pulse-amplification (CPA) technique [4], was used to ablate the DLC films. The 120-fs laser was operated at a wavelength of 800 nm and a repetition rate of 1 kHz with a maximum single pulse energy of 0.9 mJ. The output beam of the laser system is linearly polarized light with a near Gaussian beam quality. A set of neutral density (ND) filters was utilized to attenuate the beam intensity. Prior to laser processing, each sample was rinsed and cleaned in acetone and methanol and mounted on a motorized x-y stage (Coherent LabMotion Series). Two sets of experiments were conducted in ambient air. The first was a series of holes drilled by varying pulse energy using single pulse. The second was a series of holes ablated by varying the number of laser pulses at a given pulse energy. The number of laser pulses was controlled by an electronic shutter (UNIBLITZ VMM-T1).

A scanning electron microscope (SEM) (JEOL JSM 840, 10 kV accelerating voltage) in the secondary - electron mode was used to examine the laser-machined features and measure the depth of holes by a method of stereo depth measurement.

RESULTS AND DISCUSSION

For a Gaussian spatial beam profile with a $1/e^2$ -beam radius ω_0 , the maximum laser fluence at the cross-sectional surface ϕ_0 is proportional to the incident laser pulse energy E_{pulse} ,

$$\phi_0 = \frac{2E_{pulse}}{\pi\omega_0^2} \quad (7-1)$$

The diameter D of the laser-processed hole can be correlated with ϕ_0 and ϕ_{th} [5]. Where, ϕ_{th} is ablation threshold fluence.

$$D^2 = 2\omega_o^2 \ln\left(\frac{\phi_o}{\phi_{th}}\right) \quad (7-2)$$

We rearrange the equation (7-2) based on (7-1) to obtain

$$D^2 = 2\omega_o^2 \ln\left(\frac{E_{pulse}}{E_{th}}\right) \quad (7-3)$$

Obviously, we obtain ω_o and E_{th} by a plot of the square of the hole diameter *versus* logarithm of the pulse energy, which are the slope of the plot and an extrapolation to $D^2 = 0$ on x axis, respectively. Here, we chose 4 pulse energies, 0.24 μJ , 0.4 μJ , 0.6 μJ and 0.8 μJ and one single shot to drill the holes (without penetration of DLC films as observed from SEM pictures) separately and obtained $\omega_o = 2.43 \mu\text{m}$ and $E_{th} = 0.23 \mu\text{J}$ or $\phi_{th} = 2.51 \text{ J/cm}^2$ using the above linear least squares fit as shown in Figure 7.1.

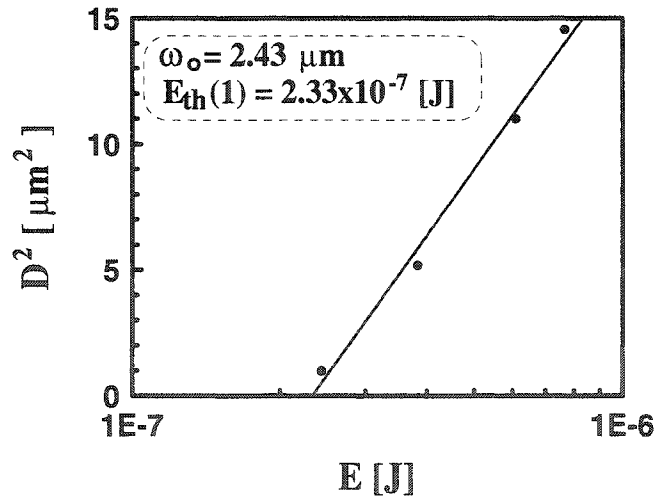


Figure 7.1. Squared diameters D^2 of the damaged areas in dependence on the applied laser pulse energies for single pulse processing ($\tau = 120 \text{ fs}$, $\lambda = 800 \text{ nm}$) of DLC in air. The slope of the plot is ω_o and an extrapolation to $D^2 = 0$ on x axis is E_{th} .

Similar hole-drillings were performed using a series of number of pulses (1, 5, 10, 50, 100, 200, 300) at the fixed pulse energy of 0.24 μJ . We also measured the diameter of each hole and calculated ablation threshold at different number of pulses by equation (3): $E_{\text{th}}(1) = 0.22 \mu\text{J}$ or $\phi_{\text{th}} = 2.43 \text{ J/cm}^2$, $E_{\text{th}}(5) = 0.17 \mu\text{J}$, $E_{\text{th}}(10) = 0.14 \mu\text{J}$, $E_{\text{th}}(50) = 0.11 \mu\text{J}$, $E_{\text{th}}(100) = 0.095 \mu\text{J}$, $E_{\text{th}}(200) = 0.081 \mu\text{J}$, $E_{\text{th}}(300) = 0.075 \mu\text{J}$. It is noted that the ablation threshold decreases with increasing number of pulses as shown in Figure 7.2. This indicates a strong dependence of ablation threshold on the number of pulses, which could be explained by an incubation model [6].

$$E_{\text{th}}(N) = E_{\text{th}}(1)N^{s-1} \quad (7-4)$$

Pulse energy threshold $E_{\text{th}}(N)$ for N pulses is related to the threshold $E_{\text{th}}(1)$ for one pulse. The exponent “ s ” characterizes the degree of incubation in the material. It is 0.81 based on fitting in Figure 7.2 and is indicative of a significant influence of incubation effect.

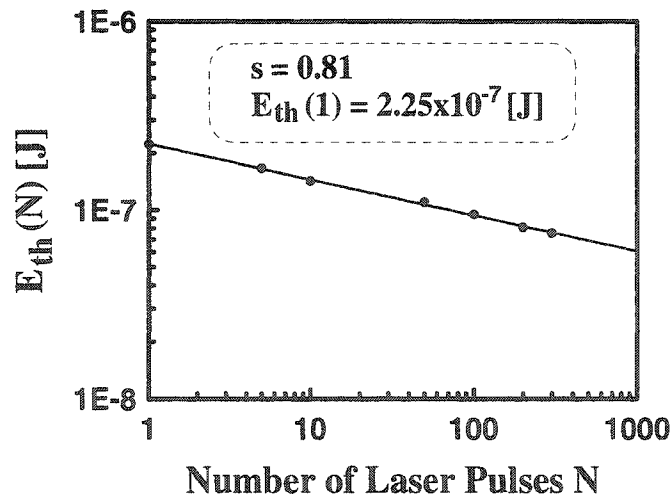


Figure 7.2. Ablation threshold $E_{\text{th}}(N)$ at 0.24 μJ as a function of the number of pulses N for the ablation ($\tau = 120 \text{ fs}$, $\lambda = 800 \text{ nm}$) of DLC in air.. The slope is “ $s-1$ ”. “ S ” characterizes the degree of incubation in the material.

This effect stems from multi-pulse induced defect generation and phase transition, which changes optical properties – increase in optical absorptivity and resultant decrease in the ablation threshold [3]. Such an incubation effect due to ultrashort laser irradiation has also occurred in other materials such as metals [7], semiconductors [8], ceramics [9] and polymers [10]. Figure 7.3 shows the SEM images of morphological features of holes drilled by different number of laser pulses at a pulse energy of 0.24 μJ . It is seen that the lateral dimension of holes apparently increases with the increase of the number of pulses until the first 50 pulses, after which it increases slowly to reach saturation but the vertical dimension of holes still increases. At 500 pulses, a major ablation occurred at the center of the irradiated region. Each hole has an elliptical shape caused by linearly polarized laser light. It is also observable that each hole has a three-zone morphology from the outmost to the innermost, which reflects the spatial distribution of Gaussian beam intensity. It may be noted that the modified region (bright part) of single-shot hole at a threshold energy of 0.24 μJ (Figure 7.3a) is much less than the spot size of laser beam ($\omega_0 = 2.43 \mu\text{m}$). This could be explained by the notion that the only peak of Gaussian laser beam reaches the threshold fluence so that the sub-diffraction limit size can be achieved [4]. It is worth noting that there is no indication of typical lateral thermal damage, like ripples, columns, recast, and cracking which were seen on a spot irradiated by a pulsed picosecond (ps) Nd:YAG laser at ablation threshold power density [3]. Cracking in ps-laser arises from a significant thermal stress build-up due to large thermal gradients. For femtosecond pulses, however, this undesirable effect was significantly reduced, suggesting that extremely short pulse duration does not allow heat propagation into the surrounding material. In addition, the high efficiency in femtosecond laser processing is

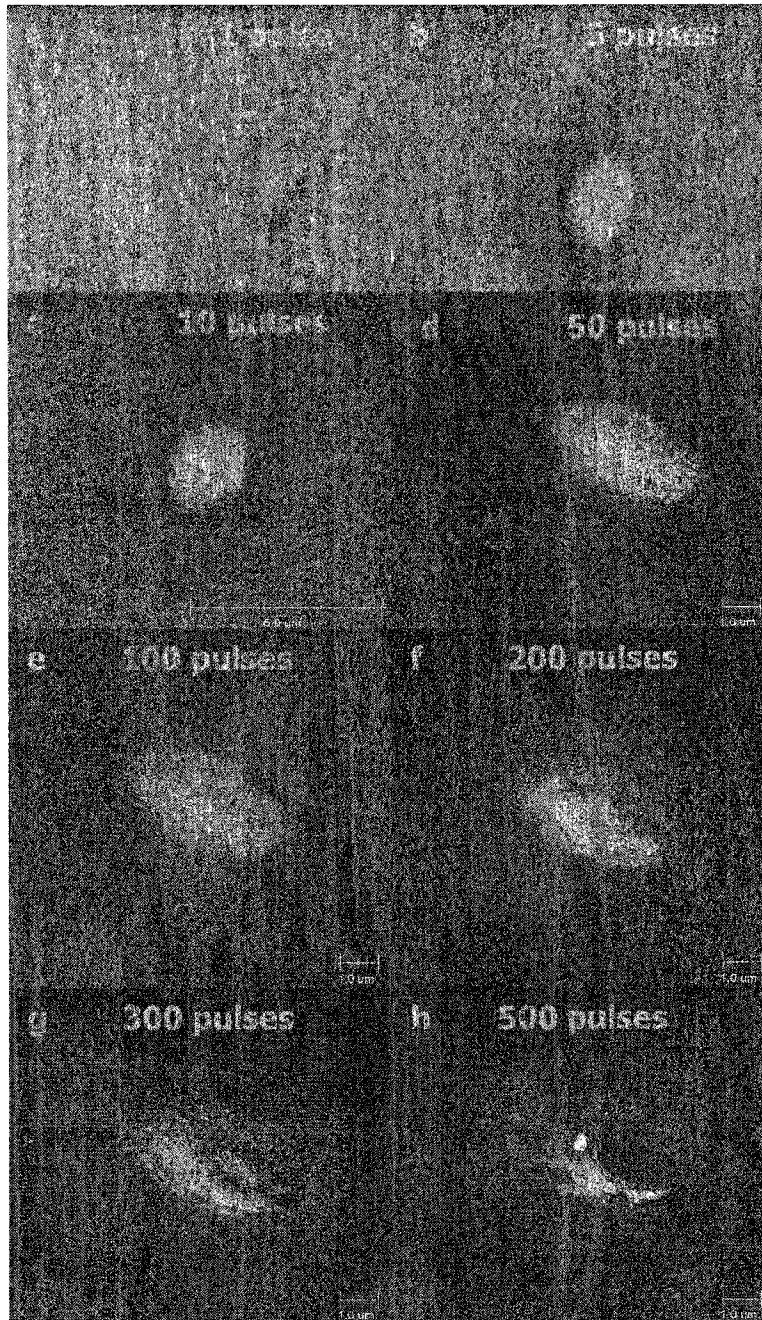


Figure 7.3. SEM images of laser-induced DLC surface morphology at $0.24 \mu\text{J}$ and N pulses (a) $N = 1$ (b) $N = 5$ (c) $N = 10$ (d) $N = 50$ (e) $N = 100$ (f) $N = 200$ (g) $N = 300$ (h) $N = 500$

realized when we compare ablation threshold power density of 2.4 KW/cm^2 for femtosecond pulses with 0.5 GW/cm^2 for picosecond pulses [3]. Ripples, typically observable wavelength-related periodic patterns on femtosecond-laser-induced Si, SiC, InP and TiN materials, were not seen in DLC possibly because an interference between the incident light and a surface wave (generated by scattering) is prevented by the better optical absorption properties due to the occurrence of graphitization during ablation [3]. Laser-induced graphitization process was verified with micro-Raman measurement [3].

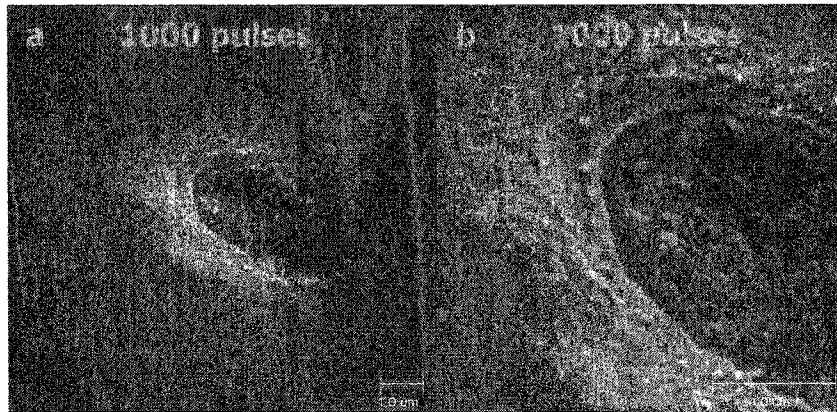


Figure 7.4. SEM images of laser-induced DLC surface morphology at $0.24 \mu\text{J}$ and 1000 pulses. (a) x 10k (b) x 30k

Figure 7.4a shows a hole ablated at 1000 pulses and $0.24 \mu\text{J}$ and Figure 7.4b is its enlarged view. *Yasumaru et al* [11] reported 40-fs-laser-induced a fine-slender-granular or a fine-dot nanostructure formed on DLC film dependent on different laser polarization. In Figure 7.4b, we cannot see such nanostructure as described. High irradiation energy fluence,

longer pulse width, different focusing optics or different deposition means of DLC films might have been responsible.

CONCLUSION

Femtosecond-laser-induced ablation threshold of DLC films was estimated using the relation between the hole diameter D , the beam radius ω_0 , and the applied laser peak fluence ϕ_0 . The DLC film ablation threshold of 2.51 J/cm^2 for femtosecond laser pulses is greatly less than that of picosecond laser pulses. The influence of the number of pulses on processed features is visibly tracked by the delicate morphological changes of holes. There are no commonly observed ripples, cracking and recast found inside and surrounding the holes, indicative of the advantages of ultrashort pulsed laser processing. The incubation effect occurred upon undergoing multi-pulse shots due to defect generation effect.

ACKNOWLEDGEMENTS

Thanks are due to Dr. Warren E Straszheim for providing SEM characterization and helpful discussion.

REFERENCES

1. P. Zhang, BK. Tay, CQ. Sun, SP. Lau, J. Vac. Sci. Technol. A 20(4) (2002) 1390
2. B. Craig, "Ultrafast pulses promise better processing of fine structures", Laser Focus World, September, 1998 p.79-88
3. D. Vouagner, Cs. Beleznai, J.P.Girardeau-Montaut, C.Templir, and H.Gonnord Diamond Relat.Mater. 9 (2000) 786

4. X.Liu, D.Du, G. Mourou, IEEE J. Quant. Electron. 33 (1997) 1706
5. J.M.Liu Opt. Lett. 7 (1982) 196
6. Y.Jee, M.F.Becker, and R.M.Walser, J.Opt. Soc.Am.B 5 (1988) 648
7. J.Güdde, J.Hohlfeld, J.G.Müller, and E.Matthias Appl. Surf. Sci 127-129 (1998) 40
8. Y.Dong and P.Molian Appl. Phys. A 77 (2003) 839
9. J.Bonse, P.Rudolph, J.Krüger, S.Baudach, and W.Kautek Appl. Surf. Sci. 154-155 (2000) 659
10. S.Baudach, J.Bonse, J.Krüger, and W.Kautek Appl. Surf. Sci. 154-155 (2000) 555
11. N.Yasumaru, K.Miyazaki and J.Kiuchi Appl. Phys. A 76 (2003) 983

CHAPTER 8. GENERAL CONCLUSIONS AND FUTURE WORK

Femtosecond pulsed lasers offer a viable alternative to conventional nanosecond pulsed lasers in micromachining and nanostructuring of diverse materials. This research provides evidence of the advantages of femtosecond laser micromachining of 3C-SiC and DLC thin films on Si over nanosecond and picosecond laser micromachining.

For 3C-SiC micromachining, this study firstly demonstrates that the nonlinear effects of air medium in ultra-short pulsed ablation for producing small features (beneficial effect) and uncontrollable geometry of ablated regions (deleterious effect) in micromachining. The effects of self-focusing are not effective until the peak power of the beam exceeds 50 times that of the critical power for self-focusing. Next, fundamental experiments conducted on drilling two sets of holes determine four threshold fluences based on morphologies of the damage surfaces distinguished by slight modification, ripple, crater and defect-activated ablation. High-quality processing of SiC films with well-defined edges can be obtained using energy fluence between thermal-modification threshold and nonthermal-ablation threshold. Helium, as an assistant gas, can improve the processing quality and the ablation rate of SiC thin films because of the ability of helium to prevent self-focusing, its high first ionization potential and inertness. Lastly, the study shows feasibility in laser-assisted surface and bulk micromachining of MEMS structures.

For 3C-SiC nanostructuring, femtosecond laser irradiation *in-situ* generates an array of highly orientated nanoparticles with size of 30~70 nm on the surface of 3C-SiC single crystalline thin films without inducing radiation defects in deeper layers of SiC film. The size of nanoparticles is independent of energy fluence within a range. Micro-Raman scattering

measurement reveals that nanoparticulate 3C-SiC layers do not undergo any stress change. But XRD shows the modification of crystal structures after laser irradiation. AES does not provide evidence of the participation of oxygen in the formation of nanoparticles.

Physical mechanisms of the interaction of femtosecond laser with 3C-SiC can be explained depending on applied fluences. Above thermal-modification threshold ($F_{th} = 0.97 \text{ J/cm}^2$), the physical process is of a classical thermal nature, involving melting, vaporization, boiling or phase explosion. Both multiphoton absorption and photo absorption of defects launch material ablation. At some irradiation fluence below thermal-modification threshold ($F_{th} = 0.97 \text{ J/cm}^2$), nanoparticles in 3C-SiC films are formed and defect-activated Coulomb explosion is responsible for this effect. The likely evidence for Coulomb explosion is the presence of nanocraters around and over nanoparticles. Irradiation fluences cause the slight modification in the lattice structure of nanoparticles. Below $0.6F_{th}$, the crystal structure of irradiated area still remains the initial cubic structure and nanoparticles are arrayed along a strong preferred lattice orientation $\langle 100 \rangle$, evident of the lattice rearrangement due to lattice heating. In the range of $0.6-0.8F_{th}$, intense emission of electrons causes the heavily disordered lattice structure and degraded the shape of nanoparticles. Above $0.8F_{th}$, melting is observed due to the enhanced multiphoton absorption. This is a very intriguing result and has potential applications in nanoelectronics and nanotribology.

Future work could include experimental study on the effect of wavelength on the size of nanoparticles and determination of hardness and Young's modulus from nanoindentation and spectrum detection. The reduction in nanoparticle size is of significant importance for its potential applications in optoelectronics and tribology. An effort to combine microelectronics fabrication techniques with ultrashort pulse micromachining to realize a functional MEMS

devices is challenge but worth a try. The time-resolved experiments are suggested to investigate the emitted ion distributions and instantaneous damage morphologies occurring during the laser-matter interaction. This is supportive for best understanding the physical process and directs optimization of experiments accordingly.

APPENDIX A. Evaluation of B-integral

$$B = \frac{2\pi}{\lambda} \int n_2 I(z) dz$$

The following parameters have been applied for the calculations: the on-axis intensity of a Gaussian beam was assumed, according to $I(r=0) = \frac{2P}{2w(z)^2}$, P is the peak power, $w(z)$ is the laser beam radius along the beam path z-direction. n_2 is the nonlinear index of refraction. λ is the wavelength of 800 nm.

B integral in air from workpiece to lens (lens has a focal length of 50 mm):

$$P = \frac{0.9mJ}{120fs} = 7.5 \times 10^9 W, \quad w(z) = w_0 \left[1 + \left(\frac{z\lambda}{\pi w_0^2} \right)^2 \right]^{\frac{1}{2}}$$

$$B = \frac{2\pi}{\lambda} \int n_2 \frac{2P}{\pi w(z)^2} dz, \quad B = \frac{4n_2 P}{\lambda} \int \frac{1}{w_0^2 \left[1 + \left(\frac{z\lambda}{\pi w_0^2} \right)^2 \right]} dz$$

assuming $X = \frac{z\lambda}{\pi w_0}$,

$$B = \frac{4n_2 P}{\lambda} \frac{\pi w_0}{\lambda} \int \frac{1}{w_0 + X^2} dX = \frac{4n_2 P}{\lambda} \frac{\pi w_0}{\lambda} \frac{1}{w_0} \arctg\left(\frac{\lambda f}{\pi w_0^2}\right)$$

$w_0 = 20 \mu m$, $n_2 = 12 \times 10^{-19} cm^2 W^{-1}$ (in air),

$$B \approx 27.02$$

B integral in quartz (lens has a thickness of 6.88 mm at its center):

$w(z) = 3\text{mm}$, assuming it is constant. $n_2 = 2.8 \times 10^{-16} \text{ cm}^2 W^{-1}$ (in quartz)

$$B = \frac{2\pi}{\lambda} \int_0^{66.88} n_2 \frac{2P}{\pi w^2} dz = \frac{2\pi}{\lambda} \int_0^{66.88} 2.8 \times 10^{-16} \text{ cm}^2 W^{-1} \frac{2(7.5 \times 10^9)W}{\pi(3)^2(10^{-1})^2 \text{ cm}^2} dz$$

$$\approx 0.802$$

The total value of the B integral is 27.822

APPENDIX B. CRITICAL REVIEW: PHYSICAL MECHANISMS AND MODELING OF ULTRASHORT LASER ABLATION

It has been well known that ultrashort (sub-ps) pulsed lasers offer various advantages such as minimal thermal damage and low and well-defined ablation threshold for material processing. To keep abreast with fast developing of ultrashort laser technology and its increasingly exciting applications, it is indispensable to give an insight into laser-matter interactions concerning the nature of excitation, the dynamics of the energy redistribution in irradiated solids, and the precursor mechanisms [1] for material removal. In the case of ultrashort lasers with a pulse duration of less than 1 ps, the mechanisms of laser ablation should take into account both electron and lattice subsystems because the time needed for phonon energy relaxation is more than laser pulse width and electron-phonon coupling is no longer neglected under this circumstance. The ablation consists of two basic steps: (1) absorption of laser radiation inside the surface layers by bound and free electrons (electronic subsystem), (2) energy transfer to the lattice (atomic subsystem), bond breaking, and material expansion [2]. Unlike nanosecond laser ablation, which goes through a normal phase change, so called thermal melting and subsequent thermal phenomena, femtosecond laser ablation may not be simply regarded as either thermal or non-thermal process. The mechanisms strongly depend on the specific optical and thermodynamic properties of the solid for a given laser wavelength and pulse duration. Considerable progress has been achieved on physical mechanisms and modeling for a variety of materials by means of both experimental techniques (pump-probe technique, time-of-flight spectroscopy, time-resolved X-ray diffraction and so on) and numerical methods. However, it still remains as a challenge to give

a complete picture of the involved phenomena. The representative mechanisms and related modeling for femtosecond laser interactions with metals, semiconductors and dielectrics, are outlined below. The physical mechanism for 3C-SiC, a wide bandgap semiconductor, is proposed on the basis of the previous findings in combination with experimental results.

The interaction of short laser pulses with metals begins with the absorption of laser energy by free electrons due to inverse Bremsstrahlung. In the case of metal processing with ultrashort laser pulses, the absorbed energy leads to strong overheating of the electron subsystem but the lattice remains cold. The highly non-equilibrium state of excited electrons is firstly relaxed by electron-electron (e-e) collisions, and then the temperature gradient drives the diffusion of hot electrons and hot-electron bath cools by electron-phonon (e-ph) interaction, the strength of which limits the diffusion range. Finally, electrons and the lattice are in the thermal equilibrium, where equilibrium thermal diffusion takes over and carries the heat into the interior of the metal [3]. Correspondingly, metals undergo vaporization, boiling or phase explosion when the lattice temperature rises up to the thermodynamic critical point, which causes the material removal. However, whether melting can occur in metals is still an open question. The temperature dynamics of electrons and lattice can be described by one-dimension, two-temperature diffusion model (TTM) [4,5]:

$$\begin{aligned}
 C_e \frac{\partial T_e}{\partial t} &= -\frac{\partial Q(z)}{\partial z} - \gamma(T_e - T_i) + S \\
 C_i \frac{\partial T_i}{\partial t} &= \gamma(T_e - T_i) \\
 Q(z) &= -k \frac{\partial T_e}{\partial z}, S = I(t) A \alpha \exp(-\alpha z)
 \end{aligned}$$

Here z is the direction perpendicular to the target surface, $Q(z)$ is the heat flux, S is the laser heating source term, $I(t)$ is the laser intensity, $A=1-R$ and α are the surface

transmissivity and the material absorption coefficient, C_e and C_i represents the volumetric heat capacity of the electron and lattice subsystem, k_e is the electron thermal conductivity, the lattice thermal conductivity is neglected since in metal the thermal conduction is dominated by electrons. γ is the phonon-electron coupling factor.

On the basis of TTM, Chichkov *et al* [6] derived the ablation depth per pulse L is

$$L \approx \alpha^{-1} \ln\left(\frac{F_a}{F_{th}}\right),$$

F_a is the absorbed laser fluence. The logarithmic dependence of the ablation depth on the laser pulse fluence has been demonstrated for metal targets with femtosecond KrF-laser pulses [7]. They consider femtosecond laser ablation process as a direct solid-vapor transition without undergoing melting because sublimation occurs on a time scale shorter than the time for the formation of the liquid phase.

Kanavin *et al* [8] studied heat propagation in metal targets irradiated by ultrashort laser pulses on the basis of TTM. In the case of a strong electron-lattice nonequilibrium, $T_e \gg T_i$, and $\tau_{eph} > \tau_{ee}$ are possible (τ_{eph} and τ_{ee} are times for electron-phonon collisions and electron-electron collisions, respectively). In this regime, the electron relaxation time is determined by the electron-electron collisions ($\tau \approx \tau_{ee} \propto T_e^{-2}$) and both the electron thermal conductivity ($k_e \propto T_e^{-2}$) and the electron thermal diffusivity ($D = K_e/C_e \propto T_e^{-2}$) rapidly decrease with increasing electron temperature (and laser fluence). At sufficiently high laser fluences, the heat propagation velocity is time independent and decreases with increasing laser fluence based on analytical solutions for the electron temperature and heat penetration depth. This result is beneficial for the processing of metals with ultrashort pulsed lasers.

Wellershoff *et al.* [3] applied TTM to describe the dependence of the threshold fluence on the pulse length and film thickness. Their results show that laser damage of

metals, even with femtosecond lasers, is purely a thermal process. Electron-phonon coupling is important for femtosecond laser damage and it is reflected by the great difference in electron diffusion lengths of noble and transition metals. The stronger the e-ph coupling is, the shorter electron diffusion length is. For example, the transfer of energy to the lattice is ten times faster for Ni than for Au because Ni has the much larger e-ph coupling constant than Au. In contrast, there is much more heat transport through the Au film than through Ni film. Accordingly, using the same fluence, it takes 10 times longer for the Au than the Ni film to reach the melting point. This result means that microstructuring is much more efficient in metals with strong *e-ph* coupling.

The interaction of linearly absorbing, covalently bonded semiconductors with femtosecond pulses is simply interpreted as: firstly, the material undergoes nonthermal ultrafast melting on a sub-picosecond time scale, subsequently, the common vaporization, boiling or phase explosion may then contribute to the material removal. The former has been the main theme of studies since the discovery of laser annealing to remove crystal damage in ion-implanted semiconductors by Van Vechten *et al* [9] because the nature of this melting, the phase transition of a material from the solid to the liquid, is of fundamental interest and practical importance for potential applications in laser-assisted material processing, surface photochemistry, optical switching, and optoelectronic devices. Femtosecond laser-induced changes in band structure and structural transition in semiconductors play a key role in determining the electronic properties of semiconductors because the pulse duration is comparable with or shorter than the characteristic times of electron-electron and electron-phonon relaxation [10].

The studies of the dynamics of laser-induced phase transition on surface of semiconductor start with time-resolved optical experiments of femtosecond laser-excited silicon [11,12], gallium arsenide [13,14] and indium antimonide [15] by measuring transient reflectivity, transmission, and second-harmonic generation [11-13,15] and dielectric function [14]. Second-harmonic generation (SHG) in reflection provides information on the order and symmetry of the crystal lattice in the surface layer. The decrease of SHG intensity means the loss of long-range crystal order. The reflectivity probes the changes in the electronic band structure and free-carrier effect. High reflectivity is most probably indicative of the formation of a metallic liquid on the surface of the crystal. The changes in dielectric constant mainly reflect modifications of the band structure. Using pump-probe technique, the experimental results show that the ultrafast drop of SHG following excitation in the high-fluence regime occurs within the time interval comparable with the pulse duration and the rise in reflectivity occurs after several hundred femtoseconds for Si [11], GaAs [13] and InSb [15]. This phase transition on a subpicosecond time scale is too fast to be attributed to the classical thermal melting (equilibrium thermal process) since the time required for highly nonequilibrium electronic subsystem due to the deposition of optical energy to heat phonon subsystem depends on the particular material but lies typically in the range of picoseconds [16]. This ultrafast phase transition termed nonthermal melting is due to instability of the crystal lattice in the presence of a dense electron-hole(e-h) plasma [17,18]. To support the model of a plasma-induced lattice instability [18], the limit of e-h plasma density is in excess of 10^{22} cm^{-3} , which corresponds to approximately 10% the total valence-band population [20]. Nanosecond laser pulse cannot produce sufficient e-h plasma density for such a mechanism to be effective. Sokolowski *et al* suggested a simple two-step model of the laser-induced

phase transition [12], in which, an initial excitation stage is followed by a transition stage. The former is likely responsible for the changes of optical parameters like SHG caused by an electronic excitation of a structurally intact solid material because the time scale of SHG fast drop is only limited by pulse duration not by materials. The latter relates the structural change of materials towards a disordered liquid phase possibly due to a plasma-induced lattice instability mechanism [18]. Chin *et al* [21] utilized time-resolved x-ray diffraction techniques on a femtosecond time scale to study ultrafast structural dynamics in InSb. This technique offered direct information of laser-perturbed structural properties of crystals. The observed lattice expansion on the picosecond time scale is attributed to the combination of energy relaxation processes and strain propagation. The nonthermal ultrafast (< 1 ps) disordering of a ~ 30 Å surface layer was directly observed. Huang *et al* [14] reported on temporally and spectrally resolved measurements of the dielectric function of femtosecond excited GaAs. The response of GaAs to the excitation depends strongly on the incident fluence. With increasing incident fluences, the excited GaAs undergoes lattice heating, lattice disorder, and semiconductor-to-metal transition.

Besides the studies of the dynamics of ultrafast nonthermal melting on a subpicosecond time scale in covalent semiconductors, Cavalleri *et al* [22] investigated laser-induced ablation of GaAs (it is shown that the behavior of GaAs is quite representative of the laser ablation process in semiconductors) using time-of-flight (TOF) mass spectroscopy. The TOF distribution below the ablation threshold can be modeled with a “free flight” half range Maxwellian irrespective of collisions. The measured temperature by fitting the measured velocity distributions of particles with the half range Maxwellian model indicates that the liquid surface of GaAs is heated significantly above the melting point, reaching a maximum

value at the ablation threshold, where the number of detected particles has a step-like increase while an ablated layer of about 10-20 nm in depth is observed by interference microscopy. This indicates the occurrence of a threshold-like bulk effect such as explosive boiling. With increasing fluence above the ablation threshold free flight desorption transforms into a collision expansion process. Ablation starts from a *bulk liquid* and is likely to be initially accompanied by expansion, phase decomposition and eventual transformation of a dense gas. According to Knudsen-layer theory, the expanded material is a non-ideal gas when energy fluence is close to the ablation threshold and it approaches an ideal gas behavior when energy fluence is above $2.5 F_{th}$. This study experimentally validates that the ablation process in semiconductors also undergoes vaporization, boiling or phase explosion as other materials.

Since the application of CPA to terawatt-class laser systems, the investigations of laser-induced breakdown of dielectrics, particularly transparent dielectrics, have been carried out over many years. A direct impetus is that damage to optical surfaces, caused by the intense short pulses, limits further increase of peak power of such systems. Ultraprecise micromachining of transparent dielectrics for optoelectronic, micro-optic, and fiber technological applications is the driver. The theoretical and experimental studies of physical mechanisms mostly address two subjects of why optical breakdown occurs [23-28] and how material removal proceeds [29-35].

Most researchers agree that the optical breakdown in dielectrics for short pulses is assisted by photoionization, such as multiphoton ionization (MPI), which mainly provides seed electrons for avalanche ionization. For long pulses, the seed electrons originate from background carrier such as impurity or shallow traps. This discrepancy gives a good

explanation of the deterministic breakdown threshold for short pulses in contrast to more statistical one for long pulses. The generated plasma at a short pulse regime is highly localized, which is beneficial for micromachining. A deviation from the scaling rule of $F_{th} \sim \tau^{1/2}$ for long pulses is observed below $\tau < 10$ ps by Du *et al* [23] and 20 ps by Stuart *et al* [24]. The damage threshold F_{th} continues to decrease with decreasing pulse width at a rate slower than $\tau^{1/2}$ [24,26] since the enhancement of multiphoton ionization or other nonlinear effects due to the decrease of pulsewidth may reduce threshold damage. Stuart *et al* [24, 25] found that multiphoton ionization instead of avalanche ionization likely becomes the dominant channel for free electron generation for $\tau < 100$ fs. For extremely short pulses ($\tau < 30$ fs), multiphoton ionization alone supplies the critical density of electrons.

The generally accepted picture of damage to defect-free dielectrics is described as follows: (1) multiphoton ionization (MPI) causing the excitation of electrons to the conduction band, (2) electron-electron collisional ionization (avalanche process) due to Joule heating, (3) the build up of conduction electrons to a critical density (10^{21}), which is necessary for further absorption of laser energy, and (4) plasma energy transfer to the lattice, thereby inducing the damage.

Rosenfeld, Ashkenasi, Varel and Stoian's experimental studies and modeling calculations [29-32] illuminate the dynamics of ultrashort pulsed laser ablation of dielectrics (sapphire) by *in situ* and *ex situ* measurements through probe-pump technique, time of flight mass spectroscopy and scanning electron microscopy. The whole ablation process is featured as two successive phases: "gentle" and "strong" etch phases, which have significant differences in terms of surface morphology, ablation rate, ion velocity distribution and ion angular distribution. According to Stoian' description [30,31], the gentle-etch phase has a

smooth surface with almost no pattern developing and no particulates around the rim associated with fast ions having the same momenta, which is attributed to Coulomb explosion due to a high concentration of uncompensated positive charge following the electron photoemission. The strong-etch phase has a greatly increased roughness, numerous particulates around the rims, and the splashed solidified liquid with the formerly molten material inside the spot and with splintered aspect of the edges indicative of a violent mechanism of thermal nature responsible for particle emission, often termed “phase explosion.” The emitted ions have slower velocity with the same kinetic energies rather than the same momenta. During the ablation process, defect formation and incubation effects exert the leverage on the material removal in the strong-etch phase. Many studies show that first laser-shot-generated defects (color centers) acting as absorption centers enhance the absorption of the deposited energy. The accumulation of such defects, termed “incubation” seems to reduce the nonlinear order of excitation, lower the damage threshold and increase the heating efficiency and coupling of the laser radiation to the sample with increasing number of shots. The incubation is a key factor for the occurrence of phase explosion, accompanied by violent ejection of a mixture of vapor and liquid droplets from the sample [33-35]. For wide band gap materials, it is confirmed that accumulation of defects is considered as an additional channel for photon absorption rather than multiphoton absorption.

SiC is a wide band-gap semiconductor ($U_1 \geq \hbar\omega$, U_1 is band-gap energy (2.3-2.9 eV for SiC), $\hbar\omega$ is photon energy) and does not absorb 800-nm laser light (1.55 eV photon energy). Hence, femtosecond optical breakdown in SiC is largely initiated by such excitation mechanisms as two-photon or higher order multiphoton electronic transitions from the

valence band to conduction band. The experimental results have also shown the effect of “incubation” (accumulation of defects) for photo absorption that lowers the threshold with increasing number of pulses. At an energy fluence equal to or above thermal modification threshold fluence of 0.97 J/cm^2 , the SEM pictures show typical collateral damage of ripple, column, recast and so forth at the machined site. The experimental observation indicates a thermal nature of femtosecond laser-SiC interaction. This process follows the excitation of electrons, the transfer of electron energy to lattice, the rise of lattice temperature to the thermodynamic critical point, which causes vaporization, boiling or phase explosion on SiC surface, finally material removal. It is expected as occurring in metal, linearly absorbed semiconductor and dielectrics. At the energy fluence between 0.45 J/cm^2 and above 0.97 J/cm^2 , the femtosecond laser irradiation induces thermal-free nanoparticles on SiC surface. The particle formation seems like another surface explosion, unlike phase explosion, leading to the ejection of materials in nanoscale.

Coulomb explosion is a plausible mechanism in the gentle-etch phase of dielectrics. At such a low fluence, Coulomb explosion more likely starts with the laser energy absorption of localized defects than other nonlinear photon absorption. The absorption of fs laser pulse by the defect states in the surface prompts the excitation of electrons and creates electron-hole pairs. A repulsive electrostatic field is then induced by the accumulation of high concentration positive charges (holes) since electron-hole pairs cannot recombine instantaneously due to low hole mobility. In this case, Coulomb explosion is initiated, leading to ion and particle ejection and eventually forming nanoscale craters on the surface. It is these craters laying over the entire irradiated surface that make this nanoparticle-like structure in SiC films.

In the studies, we found that contrary to expectations, there is no correlation between the size of nanoparticles and laser fluence. However, with a gradual increase in fluence, the array and shape of nanoparticles appear chaotic and irregular. Once the fluence exceeds 0.97 J/cm^2 , the modified SiC films undergo immediately melting phase accompanied by the disappearance of nanoparticle.

The size of particles, or the size of nanocraters should relate to the strength of the electrostatic field causing Coulomb explosion or, more directly, uncompensated electron-hole density. Sokolowski *et al* [20] studied electron-hole density in silicon as a function of excitation fluence. Based on their result (Figure 7.1.), it is found that electron-hole density seems not to have an appreciable increase in the range of from 0.45 J/cm^2 to 0.65 J/cm^2 (these are energy fluences we used to generate nanoparticles). The absorption processes determine the plasma density, and thus the density in SiC possible has an even weaker increase than in Si. In addition, the recombination of electron-hole likely become faster with the increase of energy fluence. As a result, we postulate the change of the strength of the repulsive electrostatic field within such a narrow range of energy fluences is insufficient to alter the power of Coulomb explosion, hence the size of nanoparticles. However, the increase of energy fluences influences the lattice structure through excess heating the electrons, which transfer to the lattice during the relaxation process. X-ray diffraction measurements show that lattice structural rearrangement from more stable structure to the lattice disorder with increasing the energy fluences. Once the energy fluence exceeds a certain value, electron-hole plasma density reaches a critical amount that can induce lattice instability [15,20] and then melting occurs while nanoparticles disappears.

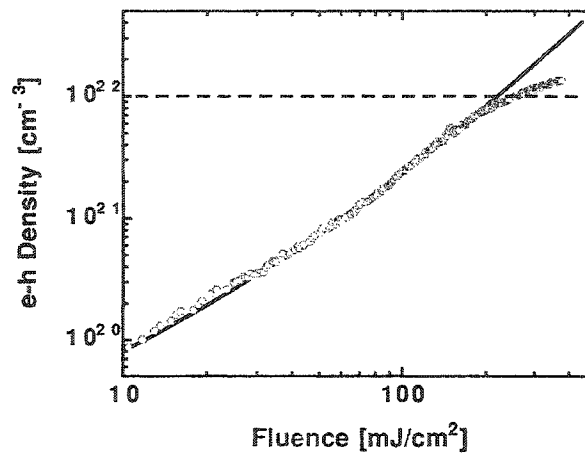


Figure B.1. Absolute electron-hole density as function of excitation fluence [20]

One question still needs to be answered: can wavelength change the size of particles? It might. It is indubitable that the wavelength can significantly affect the absorption mechanism. Some shorter wavelengths may result in the photo absorption in much denser sites of SiC surface due to the effect of “incubation” or linear photon absorption while maintaining the energy fluence at a low level inhibiting the thermal effect in the lattice. In this way, Coulomb explosion may take place on denser sites of the surface, thereby reducing the size of nanoparticles.

The analysis above applies the physical mechanisms done for semiconductor and dielectrics or wide band-gap materials to interpret the interaction of SiC with femtosecond laser. The time-resolved experimental verification of this analytical modeling will be very important for a better understanding of Coulomb explosion process by characterizing the velocity distribution and angular distribution of the emitted ions. On the other hand, calculations of net surface charge density for SiC also provide theoretical support for

Coulomb explosion mechanism because surface charge density determines the strength of electrostatic field and thus is a dominant factor for Coulomb explosion.

The continuity equation [36] used for free electrons generated by the laser pulses is as follows below:

$$\frac{\partial n_e}{\partial t} + \frac{1}{e} \frac{\partial J}{\partial x} = (\sigma_2 I^2 + \alpha n_e I) \frac{n_a}{(n_a + n_i)} - R_e - PE$$

where $\sigma_2 I^2$ is the rate of two photon ionization, n_x is the density of particles (a: neutral atoms, i: positive ions, e: electrons), I is the laser intensity, J is the electric current density, $\alpha n_e I$ is the avalanche term, R_e is the recombination term, and PE is photoemission.

Maximum photoemission occurs from the surface and decreases exponentially towards the bulk given the photoemission term

$$PE = \frac{1}{2} (\sigma_2 I^2 + \alpha n_e I) \frac{n_a}{(n_a + n_i)} \exp\left(-\frac{x}{l}\right)$$

l is the electron escape depth.

The current density is described as

$$J = -en_e \mu_e E - eD \nabla n_e$$

μ_e is the electron mobility and D is the diffusion coefficient.

The results of this modeling may track the buildup of the net positive charge on the surface of SiC as a function of time. It helps if the accumulation of net positive charges during the laser pulse is enough to induce a macroscopic Coulomb explosion of the top surface layers.

REFERENCES:

- [1] D.Bäuerle, *Laser Processing and Chemistry*, Springer, Berlin, New York, 2000, 3rd ed., Chap.13
- [2] F. Korte, S.Adams, A.Egbert, C.Fallnich, and A.Ostendorf, *Opt. Exp.* 7 41 (2000)
- [3] S.- S.Wellershoff, J. Hohlfeld, J. Güdde, E. Matthias, *Appl. Phys. A* 69 S99 (1999)
- [4] M.I. Kaganov, I.M. Lifshitz, L.V. Tanatarov, *Sov. Phys. -JETP* 4, 173 (1957)
- [5] S.I. Anisimov, B.L. Kapeliovich, T.L. Perel'oman, *Sov. Phys. -JETP* 39, 375 (1974)
- [6] B.N. Chichkov, C. Momma, S. Nolte, F. von Alvensleben, A. Tünnermann, *Appl. Phys.A* 63 109 (1996)
- [7] S. Preuss, A. Demchuk, M. Stuke, *Appl. Phys.A* 61 33 (1995)
- [8] A. P. Kanavin, I. V. Smetanin, V. A. Isakov, Yu. V. Afanasiev, B. N. Chichkov, B. Wellegehausen, S. Nolte, C. Momma, and A. Tünnermann, *Phys. Rev. B* 57 14698 (1998)
- [9] J.A. Van Vechten, R.Tsu, and F.W. Saris, *Phys.Lett.* 74 A 422 (1979)
- [10] J.L.Birman, H.Z.Cummins, and A.A. Kaplyanskii, *Laser Optics of Condensed Matter*, Plenum, New York, 1988.
- [11] H.W.K. Tom, G.D.Aumiller, and C.H.Brito-Cruz, *Phys. Rev. Lett.* 60 1438 (1988)
- [12] K.Sokolowski-Tinten, J.Bialkowski, and D. von der Linde, *Phys. Rev. B* 51 14186 (1995)
- [13] S. V. Govorkov, I. L. Shumay, W. Rudolph and T. Schroeder, *Opt. Lett.* 16 1013 (1991)
- [14] Li Huang, J. Paul Callan, Eli N. Glezer, and Eric Mazur, *Phys. Rev. Lett.* 80 185 (1998)
- [15] I. L. Shumay and U. Höfer, *Phys. Rev. B* 53 15878 (1996)
- [16] S.I. Anisimov, B.L.Kapeliovich, and T.L. Perel'man, *Sov. Phys. JETP* 39 375 (1974)
- [17] S. Das Sarma and J. R. Senna, *Phys. Rev. B* 49 2443 (1994)

- [18] P. Stampfli and K. H. Bennemann Phys. Rev. B 42 7163 (1990); 46 10686 (1992); 49, 7299 (1994)
- [19] Pier Luigi Silvestrelli, Ali Alavi, Michele Parrinello, and Daan Frenkel, Phys. Rev. Lett. 77, 3149 (1996)
- [20] K.Sokolowski-Tinten and D.von der Linde, Phys. Rev. B 61 2643 (2000)
- [21] A. H. Chin, R. W. Schoenlein, T. E. Glover, P. Balling, W. P. Leemans, and C. V. Shank, Phys. Rev. Lett. 83 336 (1999)
- [22] A. Cavalleri, K.Sokolowski-Tinten, J.Bialkowski and D.von der Linde, Appl. Phys. Lett. 72 2385 (1998)
- [23] D. Du, X. Liu, G. Korn, J. Squier, and G. Mourou, Appl. Phys. Lett. 64 3071 (1994)
- [24] B. C. Stuart, M. D. Feit, A. M. Rubenchik, B. W. Shore, and M. D. Perry, Phys. Rev. Lett. 74, 2248 (1995)
- [25] B. C. Stuart, M. D. Feit, S. Herman, A. M. Rubenchik, B. W. Shore, and M. D. Perry, Phys. Rev. B 53 1749 (1996)
- [26] M. Lenzner, J. Krüger, S. Sartania, Z. Cheng, Ch. Spielmann, G. Mourou, W. Kautek, and F. Krausz, Phys. Rev. Lett. 80 4076 (1998)
- [27] Ming Li, Saipriya Menon, John P. Nibarger, and George N. Gibson, Phys. Rev. Lett. 82 2394 (1999)
- [28] An-Chun Tien, Sterling Backus, Henry Kapteyn, Margaret Murnane, and Gérard Mourou, Phys. Rev. Lett. 82 3883 (1999)
- [29] M. Henyk, R. Mitzner 1, D. Wolfframm, J. Reif, Appl. Sur. Sci. 154–155 249 (2000)
- [30] D. Ashkenasi), R. Stoian, A. Rosenfeld, Appl. Sur. Sci. 154–155 40 (2000)

- [31] R. Stoian, H. Varel, A. Rosenfeld, D. Ashkenasi, R. Kelly, and E.E.B. Campbell, Appl. Sur. Sci. 165 44 (2000)
- [32] R. Stoian, D. Ashkenasi, A. Rosenfeld, and E. E. B. Campbell, Phys. Rev. B 62 13167 (2000)
- [33] Roger Kelly, Antonio Miotello, Appl. Sur. Sci. 96-98 205 (1996)
- [34] Roger Kelly, Antonio Miotello, Aldo Meleb, Anna Giardini Guidoni, John W. Hastie, Peter K. Schenck, and Hideo Okabe, Appl. Sur. Sci. 133 251(1998)
- [35] A. Miotello, R. Kelly, Appl. Phys. A 69 [Suppl.] S67 (1999)
- [36] R. Stoian, A. Rosenfeld, D. Ashkenasi, I. V. Hertel, N. M. Bulgakova, and E. E. B. Campbell, Phys. Rev. Lett. 88, 097603 (2002)